

UNDERSTANDING UPPER TROPOSPHERIC AND LOWER STRATOSPHERIC
TEMPERATURE STRUCTURE VARIATIONS OVER TROPICAL AND EXTRATROPICAL
PRECIPITATION SYSTEMS

A Dissertation

by

BENJAMIN JOHNSTON

BS, California University of Pennsylvania, 2009
MS, University of Maryland, 2012

Submitted in Partial Fulfillment of the Requirements for the Degree of

DOCTOR OF PHILOSOPHY

in

COASTAL AND MARINE SYSTEM SCIENCE

Texas A&M University-Corpus Christi
Corpus Christi, Texas

December 2019

© Benjamin Ryan Johnston

All Rights Reserved

December 2019

UNDERSTANDING UPPER TROPOSPHERIC AND LOWER STRATOSPHERIC
TEMPERATURE STRUCTURE VARIATIONS OVER TROPICAL AND EXTRATROPICAL
PRECIPITATION SYSTEMS

A Dissertation

by

BENJAMIN JOHNSTON

This dissertation meets the standards for scope and quality of
Texas A&M University-Corpus Christi and is hereby approved.

Feiqin Xie, PhD
Chair

Chuntao Liu, PhD
Committee Member

Toshiaki Shinoda, PhD
Committee Member

Michael Starek
Committee Member

Robert Cutshall
Graduate Faculty Representative

December 2019

ABSTRACT

The upper troposphere and lower stratosphere (UTLS) is a coupling region in the atmosphere in which air typically has characteristics of both the troposphere and stratosphere. This region is distinct in radiation, dynamics, chemistry, and microphysics, and a strong connectivity amongst these different processes makes it highly susceptible to climate change. Stratosphere-troposphere exchange across the tropopause is an important bidirectional process influencing the chemistry of the UTLS. Deep convection plays a large role in this exchange through the direct convective injection of water vapor into the lower stratosphere, by enhancing thin cirrus cloud presence, and by modulating the ozone budget. Many of these processes are also influenced by the extremely low temperatures at these altitudes. Therefore, understanding the role convection plays in the heat budget of the UTLS is paramount in climate research. In this dissertation, firstly, the UTLS vertical temperature structure changes near deep convection are quantified throughout two tropical regions. Deep convection observed from the Tropical Rainfall Measuring Mission (TRMM) satellite is collocated with high vertical resolution temperature profiles from COSMIC GPS Radio Occultation (RO) satellites along with ERA-Interim reanalysis from 2007 to 2011. A distinct layered structure of upper tropospheric warm anomalies, tropopause-level cool anomalies, and lower stratospheric warm anomalies is observed. The amplitude of temperature anomalies increases for deeper convection, marked by higher 20 dBZ radar echo top heights or colder infrared cloud-top temperatures. UTLS diurnal temperature variation also increases in both regions near deep convection. Secondly, to further examine the relationship between convection and UTLS temperatures, precipitation systems with different sizes, depths, and surface types are analyzed within different synoptic environments throughout the extratropics.

Precipitation features (PFs) observed by the Global Precipitation Measurement (GPM) satellite are collocated with nearby GPS RO temperature profiles from 2014 to 2017. PFs are classified as non-deep stratospheric intrusion (non-DSI; more likely to be related to thermodynamic instability) or deep stratospheric intrusion (DSI; related to strong dynamic effects on the tropopause through folding) using potential vorticity. Non-DSI PFs introduce a similar vertical UTLS temperature anomaly structure to the tropics, whereas DSI PFs are mainly associated with major cooling from the mid-troposphere to just above the tropopause. These warm and cool anomalies also display strong seasonal variations from the subtropics to the high latitudes. Additionally, small but deeper non-DSI PFs typically result in lower lapse rate tropopause (LRT) heights, whereas large size but shallower PFs lead to a higher LRT. On the other hand, DSI PFs are almost always associated with large LRT height decreases. Finally, the unique characteristics of the extratropical tropopause are analyzed by illustrating when and where bimodal tropopause height distributions occur and how they relate to different synoptic environments and the occurrence of double tropopauses within individual temperature profiles. Tropopause heights are calculated and analyzed seasonally using COSMIC GPS RO temperature profiles from 2006-2017. Tropopause bimodality occurs within the subtropics (between 20°-40°) and a distinct seasonality is observed, with bimodality occurring most frequently in winter due to a stronger subtropical jet stream. The region with a bimodal tropopause distribution nearly overlaps with the region that experiences a high frequency of double tropopauses (DTs). DT occurrence frequency is highest in winter along the poleward edge of the bimodal band. However, when analyzing profiles with only a single tropopause identified, bimodality occurs much less frequently and is reduced in meridional extent. These results suggest that seasonal tropopause bimodality is caused by two different factors, as the occurrences of double tropopauses strongly

influence the tropical side of the bimodal band while single tropopause profiles that are more tropical in nature strongly influence the poleward side. The results shown in this dissertation display the unique characteristics of the UTLS and the noteworthy impact that both tropical and extratropical precipitation systems have on its thermodynamic structure. Additionally, these results suggest there are intricate relationships between different types of precipitation systems and their properties to the types of temperature anomalies that they produce. This study will enhance the community's understanding of both tropical and extratropical convection, stratosphere-troposphere exchange processes, and tropopause characteristics.

TABLE OF CONTENTS

CONTENTS	PAGE
ABSTRACT.....	v
TABLE OF CONTENTS.....	viii
LIST OF FIGURES	xii
CHAPTER I: INTRODUCTION.....	1
CHAPTER II: THE EFFECTS OF DEEP CONVECTION ON REGIONAL TEMPERATURE STRUCTURE IN THE TROPICAL UPPER TROPOSPHERE AND LOWER STRATOSPHERE	8
2.1. Introduction	8
2.2. Data Description.....	11
2.2.1. TRMM Precipitation Feature Product	11
2.2.2. COSMIC RO Data.....	13
2.2.3. ERA-I data	14
2.2.4 Study Regions and the Spatial/Temporal Distribution of Tropical Deep Convection .	14
2.2.5. COSMIC/ERA-I Dry-Temperature Versus Temperature Differences	17
2.3. Methodology	18
2.3.1 Data Set Collocation and Diurnal Temperature Anomaly Analysis.....	18
2.3.2 Diurnal Variation Analysis	19
2.3.3 Convective Intensity Variation Analysis	20

2.4. Results and Discussion.....	21
2.4.1 UTLS Diurnal Temperature Anomalies	21
2.4.2 Diurnal Temperature Variation at Different Altitudes	24
2.4.3 Impact of Deep Convection Height and Intensity on UTLS Temperature Anomalies. 27	
2.4.3.1 Deep Convection With Various 20 dBZ Echo Top Heights	28
2.4.3.2 Deep Convection with Various 40 dBZ Echo Top Heights.....	32
2.4.3.3 Deep Convection with Various Minimum Infrared CTT.....	35
2.4.4 ERA-I Results Comparison	40
2.5. UTLS Convective Impact Discussion	43
2.6. Conclusions	45
Acknowledgements	47
 CHAPTER III: RELATIONSHIPS BETWEEN EXTRATROPICAL PRECIPITATION SYSTEMS AND UPPER TROPOSPHERIC AND LOWER STRATOSPHERIC TEMPERATURES AND TROPOPAUSE HEIGHT OBSERVED FROM GPM AND GPS RADIO OCCULTATION	
	49
3.1. Introduction	49
3.2. Data Description.....	53
3.2.1 GPM Precipitation Feature Product.....	53
3.2.2 GPS Radio Occultation Data	54
3.2.3 ERA-Interim Data.....	56

3.3. Methodology	56
3.3.1 Zonal Mean UTLS Temperature Variation from GPS Observations	57
3.3.2 PF and GPS Temperature Profile Classification with Isentropic Potential Vorticity (IPV)	59
3.3.3 UTLS Temperature Anomaly and Tropopause Height/Temperature Anomaly Calculations	63
3.4. Study Regions, Sampling, and Storm Characteristics	68
3.5. Results	71
3.5.1 Relationship of PF Characteristics to UTLS Temperature Anomalies	71
3.5.1.1 Non-DSI PFs	72
3.5.1.2 DSI PFs	77
3.5.2 PF Relationship to Tropopause Height/Temperature Anomalies	82
3.6. Conclusions	89
Acknowledgements	93
 CHAPTER IV: CHARACTERISTICS OF THE EXTRATROPICAL TROPOPAUSE: BIMODALITY AND ITS RELATIONSHIP TO THE OCCURRENCE OF DOUBLE TROPOPAUSES.....	
4.1. Introduction	95
4.2. Data Description.....	99
4.3. Methodology	101

4.4. Results	104
4.4.1 Bimodal Tropopause Locations and Characteristics	104
4.4.2 Relationship of Double Tropopause Environments to the Occurrence of Bimodality	111
4.5. Summary	122
Acknowledgements	125
CHAPTER V: CONCLUSION.....	126
REFERENCES	132

LIST OF FIGURES

FIGURES	PAGE
<p>Figure 2.1. Distribution of tropical deep convection (maximum 20 dBZ echo top height > 10 km) observed by Tropical Rainfall Measuring Mission per $1^\circ \times 1^\circ$ grid from 2007 to 2011. The two selected regions of study, the Pacific Warm Pool (PWP) and the Tropical Atlantic Continental and Oceanic (TACO) region, are highlighted by the black rectangle boxes.....</p>	15
<p>Figure 2.2. Diurnal distribution of the subsampled Tropical Rainfall Measuring Mission deep convective systems that have near coincident COSMIC Radio Occultation profiles within 300 km and 3 h after convection occurrence over the (left) Pacific Warm Pool (PWP) and the (right) Tropical Atlantic Continental and Oceanic (TACO) region, with collocations classified by land (red) and ocean (cyan).</p>	16
<p>Figure 2.3. ERA-Interim specific humidity (g/kg) (blue) along with the difference between temperature and dry temperature (red) for the mean background conditions (BG, dotted lines) versus after deep convection (DC, solid lines) in the (a) Pacific Warm Pool (PWP) and (b) Tropical Atlantic Continental and Oceanic (TACO) region.....</p>	18
<p>Figure 2.4. Diurnal distribution of COSMIC dry temperature anomalies (K) after deep convection in the (a) Pacific Warm Pool (PWP) and (b) Tropical Atlantic Continental and Oceanic (TACO). Dashed lines represent cold-point tropopause height.....</p>	23
<p>Figure 2.5. Diurnal temperature anomalies (K) in the (a, c) Pacific Warm Pool (PWP) and (b, d) Tropical Atlantic Continental and Oceanic (TACO) region for background conditions (Figures 2.5a and 2.5b) and after deep convection (Figures 2.5c and 2.5d). Anomalies (solid lines) are shown along with their diurnal components from harmonic analysis (dashed lines) at 11 km (red) and 17 km (blue) using COSMIC profiles.</p>	25

Figure 2.6. COSMIC temperature anomalies (K) near deep convection classified by the PR-derived maximum 20 dBZ heights in the Pacific Warm Pool (top) and Tropical Atlantic Continental and Oceanic region (bottom) for (a, d) all convection, (b, e) convection over land, and (c, f) convection over oceans. 30

Figure 2.7. COSMIC temperature anomalies (K) near deep convection classified by the PR-derived maximum 40 dBZ heights in the Pacific Warm Pool (top) and Tropical Atlantic Continental and Oceanic region (bottom) for (a, c) convection over land and (b, d) convection over oceans. 34

Figure 2.8. COSMIC temperature anomalies (K) near deep convection classified by the VIRS minimum IR brightness temperature in the Pacific Warm Pool (top) and Tropical Atlantic Continental and Oceanic region (bottom) for (a, d) all convection, (b, e) convection over land, and (c, f) convection over oceans. 36

Figure 2.9. Two-dimensional histogram of the COSMIC temperature anomalies (K) at 16 km altitude near deep convection classified by the PR maximum 20 dBZ echo top height and VIRS minimum IR brightness temperature (CTT) in the Pacific Warm Pool (top) and Tropical Atlantic Continental and Oceanic region (bottom) for (a, c) convection over land and (b, d) convection over oceans. 39

Figure 2.10. ERA-I temperature anomalies (K) near deep convection classified by the PR-derived maximum 20 dBZ heights in the Pacific Warm Pool (top) and Tropical Atlantic Continental and Oceanic region (bottom) for (a, d) all convection, (b, e) convection over land, and (c, f) convection over oceans. 42

Figure 3.1. Climatology of UTLS zonal mean monthly temperatures (solid contours, in km) and standard deviation (color contours, in km) between 80°N and 80°S derived from COSMIC

GPS RO profiles from 2006-2017. Lapse-rate tropopause height is shown with a solid white contour. Temperatures greater than 250 K are removed. Additional temperature contours are added between 205-225 K to better display UTLS structure..... 59

Figure 3.2. GPS RO sampling for non-DSI (solid blue contours) and DSI (solid red contours) background profiles from 2006-2017 for a) January, b) April, c) July, and d) October. Shaded contours display LRT height differences (km) between non-DSI and DSI background profiles, provided the sampling is at least 10 profiles. 63

Figure 3.3. Two overshooting non-DSI PFs (a,c) with collocated GPS temperature profiles (solid red) along with their associated non-DSI (solid black) and DSI (dotted black) background profiles. Blue asterisks and the associated dashed lines indicate the height and temperature of the background and PF LRT. Dotted blue line indicates the PF maximum echo top height. Blue-shaded area shows the region ± 5 km around the PF's LRT height for anomaly calculation. Temperature anomaly profile is shown on the bottom (b,d) with the "zero" height corresponding to the PF's LRT height..... 65

Figure 3.4. Overshooting convection observed by GPM over South Dakota in the morning of July 28, 2015. a) PR Ku-band near-surface reflectivity (dBZ). b) PR Ku-band maximum echo top heights (km). c) ERA-Interim potential vorticity at 320 K potential temperature over the GPM PR swath. d) Collocated temperature profile (red) near the maximum echo top height (43.8° N, 100.7° W) and the corresponding background profile (black), along with the PF lapse rate tropopause height (red) and maximum echo top height (blue). e) Cross-section of PR Ku-band reflectivity (dBZ) through the center of the storm. Red line is the GMI 37 GHz polarization-corrected temperature (K); blue line is the GMI 89 GHz polarization-corrected temperature (K); and black line is the rain rate (10 mm/hr). 67

Figure 3.5. Distribution of extratropical PFs ($RD > 0.5$) observed by GPM from 2014 to 2017 for
a) non-DSI PFs categorized by size, b) non-DSI PFs categorized by RD, c) DSI PFs
categorized by size, and d) DSI PFs categorized by RD. 69

Figure 3.6. Histograms for non-DSI (NDSI) and DSI PFs with GPS collocations over land (L, in
red/cyan) and ocean (O, in green/yellow) within 35° - 50° (top) and 50° - 65° (bottom) from
2014 to 2017 for various PF characteristics, including (a,d) maximum echo top heights (km),
(b,e) area (km^2), and (c,f) month of the year. NH and SH represent Northern Hemisphere and
Southern Hemisphere, respectively. 71

Figure 3.7. GPS RO temperature anomalies (K) near non-DSI PFs classified by relative depth (top)
and area (bottom, in km^2) for (a,d) all PFs, (b,e) land PFs, and (c,f) oceanic PFs. The number
of PFs within each category is also displayed after each label. 73

Figure 3.8. Monthly mean GPS RO temperature anomaly profiles (K) near non-DSI PFs over a)
 20° - 40° N, b) 40° - 65° N, c) 20° - 40° S, and d) 40° - 65° S. The number of PFs within each
category is also displayed after each label. 77

Figure 3.9. GPS RO temperature anomalies (K) near DSI PFs classified by relative depth (top) and
area (bottom, in km^2) for (a,d) all PFs, (b,e) land PFs, and (c,f) oceanic PFs. The number of
PFs within each category is also displayed after each label. 79

Figure 3.10. Monthly mean GPS RO temperature anomaly profiles (K) near DSI PFs over a) 40° -
 65° N and b) 40° - 65° S. The number of PFs within each category is also displayed after each
label. 82

Figure 3.11. Two-dimensional histogram (contour) and joint-distribution of lapse rate tropopause
height and temperature anomalies (shaded) with corresponding PF size and relative depth for
non-DSI (a,c) and DSI (b,d) PFs. 84

Figure 3.12. Two-dimensional histogram of the PF LRT temperature (K) and height (km) anomalies (solid contours) and the joint-distribution of the temperature anomalies (K) at the PF LRT from Figures 3.7 and 3.9 (shaded contours) for (a) non-DSI and (b) DSI PFs. Also shown are examples of common PF-located GPS temperature profiles (red) for (c) non-DSI (2015-07-05) and (d) DSI (2016-05-02) PFs along with their associated background profiles (black). Dashed lines indicate the tropopause height and temperature for both profiles and dotted lines indicates maximum echo top height. 87

Figure 3.13. Sampling contours for PFs collocated with GPS temperature profiles comparing the potential vorticity values (PVU) at the 320 K isentrope with the lapse rate tropopause height (a, km) and temperature (b, K) anomalies that occurred near the PF. Solid red lines separate non-DSI and DSI PFs..... 89

Figure 4.1. Tropopause height histograms and inter-class variances in DJF (a,c) and JJA (b,d) for a grid located over Florida (27.5°-30°N, 80°-85°W)..... 103

Figure 4.2. Probability distribution functions (PDFs) of tropopause heights (km) in DJF (blue), MAM (green), JJA (red), and SON (purple) for Beit Dagan (a), Kashi (b), Perth (c), and Durban (d)..... 106

Figure 4.3. Seasonal distribution (a: DJF, b: MAM, c: JJA, d: SON) of bimodal tropopause height locations and threshold values for separating the two modes..... 109

Figure 4.4. Seasonal distribution (a: DJF, b: MAM, c: JJA, d: SON) of bimodal tropopause height locations and total relative frequency of occurrence (%) of profiles with tropopause heights within the lower mode. 110

Figure 4.5. Typical individual double tropopause profiles when the first (lower) LRT height is below (blue) and above (red) the bimodal tropopause height threshold in each respective

region for Beit Dagan (a), Kashi (b), Perth (c), and Durban (d). The blue and red dotted lines are the locations of the first and second tropopause heights, while the black dashed line is the bimodal height threshold..... 112

Figure 4.6. Seasonal distribution (a: DJF, b: MAM, c: JJA, d: SON) of the total frequency of occurrence (%) of temperature profiles with double tropopauses observed. The region that displays LRT height bimodality is outlined by the black and gold contours..... 114

Figure 4.7. Seasonal distribution (a: DJF, b: MAM, c: JJA, d: SON) of bimodal tropopause height locations and the percentage of double tropopause profiles that have their first (lower) tropopause height within the lower mode. 116

Figure 4.8. Seasonal mean temperature profiles within four grids for double tropopause profiles with tropopause heights within the lower mode (solid lines) and the upper mode (dashed lines) for DJF (red), MAM (teal), JJA (blue), and SON (orange). 118

Figure 4.9. Seasonal distribution (a: DJF, b: MAM, c: JJA, d: SON) of bimodal tropopause height locations for profiles that have double tropopauses identified and threshold values for separating the two modes..... 120

Figure 4.10. Seasonal distribution (a: DJF, b: MAM, c: JJA, d: SON) of bimodal tropopause height locations for profiles that only have a single tropopause identified and threshold values for separating the two modes..... 121

CHAPTER I: INTRODUCTION

The upper troposphere and lower stratosphere (UTLS) is a coupling region in the atmosphere in which air typically has characteristics of both the troposphere and stratosphere (Gettelman & Birner, 2007; Peevey et al., 2014). It is generally defined as the region ± 5 km around the tropopause (Gettelman et al., 2011), which is the boundary between the troposphere and stratosphere and plays a crucial role in UTLS processes (Holton et al., 1995; Haynes et al., 2001). The UTLS is distinct in radiation, dynamics, chemistry, and microphysics, and a strong connectivity amongst these different processes makes the UTLS highly susceptible to climate change (Birner, 2006). For example, the UTLS has an important influence on troposphere/stratosphere chemical composition and on radiation escaping to space due to relative minimum temperatures and thin cirrus cloud formation at these altitudes, which affects the surface climate and climate feedbacks (Gettelman et al., 2011). The dynamics of the UTLS may also influence stratospheric annular modes and their effects on the troposphere. This means the UTLS is important for influencing the persistence of tropospheric weather regimes in the middle and high latitudes, so a better understanding of the UTLS could allow for improved weather predictability (Gettelman et al., 2011).

The boundary that separates the turbulently-mixed troposphere and the more stable stratosphere (Anel et al., 2008) is known as the tropopause and it is one of the most important regions of the atmosphere. Characteristics of the tropopause are important because the tropopause acts as a “two-way gate” for the exchange of mass, water vapor, and chemical species between the troposphere and stratosphere (Fueglistaler et al., 2009). A fundamental characteristic of the tropopause is the change in static stability across the interface (Randel et al., 2007). The WMO definition of the tropopause is based on thermal criteria using the temperature

lapse rate (lapse rate tropopause, or LRT) and provides a convenient way to define the tropopause (World Meteorological Organization (WMO), 1986). The tropopause can also be defined by more general stability criteria using the potential vorticity-based dynamical tropopause (Hoskins et al., 1985) or the ozone-based chemical tropopause (Pan et al., 2004). The long-term variability and trends of the tropopause height have been recognized as a climate change indicator (Birner, 2006; Homeyer et al., 2010) because the tropopause is located in a region of minimum temperatures and is sensitive to changes in the concentration of radiatively active species in the UTLS (Gettelman et al., 2011; Peevey et al., 2014). For example, Santer et al. (2003) showed that tropopause height is closely associated with tropospheric warming and stratospheric cooling. Global tropopause height is controlled by many interacting processes, such as radiation, the effect of baroclinic eddies, the stratospheric mean meridional circulation, and deep convection (Stohl et al., 2003). Thus, continuous identification and monitoring of the tropopause has become an important topic in atmospheric and climate research and enhanced understanding of tropopause behavior, especially in relation to deep convection, can contribute knowledge to a variety of meteorological topics (Feng et al., 2011; Randel et al., 2007).

Stratosphere-troposphere exchange (STE) across the tropopause is an important bidirectional process influencing the chemistry of the UTLS (Holton et al., 1995). Many recent studies have focused on understanding the role convection plays in STE throughout the tropics (e.g. Grosvenor et al., 2007; Fueglistaler et al., 2009; Hassim & Lane, 2010) since radiative-convective balance is the dominant physical process in the region (Held, 1982). Deep convection influences climate processes by regulating stratospheric water vapor through direct convective injection, by enhancing thin cirrus cloud presence, and by modulating the ozone budget in the upper troposphere (Sherwood et al., 2003; Kim & Dessler, 2004; Pan et al., 2004). Water vapor

is the most important greenhouse gas in the atmosphere, and even though it is of low abundance in the UTLS, it plays a significant role in the radiative budget at this altitude (Fueglistaler et al., 2009). Additionally, understanding stratospheric hydration/dehydration processes due to deep convection requires accurate measurements of temperature and circulation changes in the UTLS (Randel et al., 2003). This has resulted in attempting to understand the role convection plays in the heat budget of the UTLS becoming a prominent research topic over the past few decades, especially in the tropics. For example, Sherwood et al. (2003) observed warm anomalies in the mid-to-upper troposphere over the Indian and western Pacific Ocean convective regions from radiosonde data, and Gettelman and Birner (2007) also detected warm anomalies at these altitudes using two climate models. Near the tropopause, Holloway and Neelin (2007) found cool anomalies using a combination of AIRS satellite and radiosonde data, while more recently, Paulik and Birner (2012), Khaykin et al. (2013), Xian and Fu (2015), and Kim et al. (2018) also observed cool anomalies using GPS radio occultation (RO) profiles. However, the amplitude of warm and cool temperature anomalies varied significantly between these studies from ± 0.5 K to as much as ± 5 K. Thus, the overall effects of convection on the UTLS temperature structure and the contribution of various dynamical processes towards these anomalies are still not well quantified. While many studies have observed UTLS temperature changes due to tropical deep convection, few, if any, have studied deep convective temperature anomalies on a diurnal scale or examined the distinct anomaly differences that can be caused by convective land-ocean contrast. Separating land and ocean convection is very important because of the large differences in both the intensity and diurnal variation of the convection. For example, based on TRMM observations, the typical peak of land convection is concentrated during the late-afternoon local time while oceanic convection has a much weaker diurnal structure, with a mild

peak seen in the early morning (Liu and Zipser, 2009). Additionally, over land, the mature and more organized convective systems typically appear later in the evening compared to earlier in the afternoon for more isolated convection. Thus, such a strong diurnal variation in frequency and intensity may affect the UTLS temperature structure very differently.

On the other hand, the relationship of extratropical convection to UTLS temperature and tropopause height changes has attracted much less attention. While this is partly because detailed observations of extratropical convection with good diurnal coverage were not widely available before the GPM era, it is also because a variety of other dynamical processes have been identified to be associated with extratropical STE (Sprenger et al., 2007), making it difficult to quantify their relative contributions. These processes include tropopause folds near the subtropical and polar jets due to baroclinic wave dynamics (Danielsen, 1968; Baray et al., 2000), cutoff lows (Price & Vaughan, 1993), gravity wave breaking (Lamarque et al., 1996), and mesoscale convective complexes (Poulida et al., 1996). For example, significant STE occurs due to turbulent mixing during baroclinic tropopause folds (Reid & Vaughan, 2004), and these folds can even reach nearly as low as the boundary layer (Vaughan et al., 1994). Additionally, simulations have shown that a large fraction of STE near folds occurs due to deep convection below the depressions in the tropopause (Gray, 2003). Note that the global-scale aspects of extratropical STE over longer timescales has been described in previous reviews (e.g. Holton et al., 1995). However, it is critical to study synoptic and mesoscale extratropical storms and their relationship to UTLS temperatures to better understand extratropical STE on shorter timescales.

Additionally, the boundary between the tropics and extratropics is often characterized by a split in the tropopause rather than a smooth transition. This results in tropopause discontinuities observed near the subtropical jet. At and poleward of these breaks, multiple tropopauses or stable

layers have been found in the thermal structure of the atmosphere using radiosonde data (Seidel & Randel, 2006). Much research has been done over the past few decades to better characterize this thermal structure. For example, it has been shown that a large percentage of temperature profiles display a double tropopause during the midlatitude winter (40-80%) and this frequency decreases into the summer (Peevey et al., 2012; Schmidt et al., 2006). Randel et al. (2007) showed that double tropopauses occur when the low latitude (tropical) tropopause extends to higher latitudes, overlying the lower tropopause. Seidel & Randel (2007) also showed using radiosonde data that at similar latitudes in the subtropics, the tropopause heights can display a bimodal structure. In these regions, the tropopause is sometimes at the height of the tropical tropopause and other times at a height typical of the extratropical tropopause and there is a clear separation of about 3–5 km between the modes. Most importantly, they state that this feature is not simply a reflection of seasonal variability, but tropopause heights were not analyzed seasonally in the study. The location and strength of the subtropical jet is known to vary considerably with season, which could have an impact on when and where bimodality occurs.

Space-borne radar observations from TRMM have been widely used in identifying the vertical extent of deep convection throughout the tropics with a long record of convection data stretching back to 1997. In the extratropics, highly sensitive radar and lidar measurements from CloudSat and CALIPSO have aided observation of vertical cloud structures, but both satellites on the A-train orbit only capture storms at fixed local times of 1:30 P.M. and 1:30 A.M., which misses the peak occurrence of land convection in the extratropics (Homeyer et al., 2014). Moreover, the small swath of both satellites limits the spatial sampling of individual storms. Now, these gaps are filled by the GPM mission, which was launched in February 2014. The space-borne radar onboard the GPM satellite, along with high orbit inclination, extends the

vertical scan of storms to the high latitudes (Hou et al., 2014). However, a limitation of both TRMM and GPM is that they do not provide thermodynamic information within the convection. To better understand storm structure, additional information from nearby temperature profiles have historically been obtained from radiosonde soundings with limited spatial and temporal sampling or meteorological analyses/reanalyses with coarse vertical resolution and large uncertainty near the convection. Now, GPS Radio Occultation (RO) soundings have begun to fill these gaps by offering global observations of UTLS temperatures with a high vertical resolution in all-weather conditions (Anthes et al., 2008).

Considering the profound impact of convection on UTLS dynamics and stratosphere-troposphere exchange, there are still many questions to be answered to better understand the relationship of convective properties to the UTLS heat budget. The specific questions that will be addressed in this dissertation include the following:

- What impact do different types of convection and different synoptic environments have on the surrounding UTLS temperatures throughout both the tropics and extratropics?
- How does convective depth, size, and land-ocean contrast impact the magnitude of UTLS temperature anomalies?
- Does convection increase the amplitude of diurnal temperature variation in the tropics?
- How are precipitation systems related to changes in tropopause heights in the extratropics?
- Where and when does tropopause bimodality occur and how is it related to the occurrence of double tropopauses?

To address these questions, this dissertation has three main chapters that have led to three research journal papers. The first manuscript focuses on quantifying the UTLS vertical

temperature structure changes near deep convection throughout two different tropical regions (Chapter II). The second manuscript expands on the first study by now moving to the extratropics. The relationship between UTLS temperatures and precipitation systems with different sizes, depths, and surface types are analyzed within two different synoptic environments (Chapter III). The third manuscript focuses on the unique characteristics of the extratropical tropopause by determining when and where tropopause bimodality appears and how it relates to the occurrence of double tropopauses (Chapter IV). Finally, a summary is provided in Chapter V.

CHAPTER II: THE EFFECTS OF DEEP CONVECTION ON REGIONAL TEMPERATURE STRUCTURE IN THE TROPICAL UPPER TROPOSPHERE AND LOWER STRATOSPHERE

2.1. Introduction

The tropical tropopause layer (TTL), generally defined as a layer between 14 and 18.5 km in altitude (Gettelman & Birner, 2007; Hassim & Lane, 2010), is the transition region of the tropical upper troposphere and lower stratosphere (UTLS) in which air has characteristics of both the troposphere and stratosphere. Interest in the heat budget of the TTL has increased in recent years because tropical deep convection plays a significant role in regulating stratospheric water vapor through direct convective injection and also by enhancing thin cirrus cloud presence, both of which play a significant role in the climate (Sherwood et al., 2003; Kim & Dessler, 2004; Hassim & Lane, 2010). Water vapor is the most important greenhouse gas in the atmosphere, and even though it is of low abundance in the TTL, it plays a significant role in the radiative budget at this altitude (Fueglistaler et al., 2009). Additionally, it is one of the main sources of OH radicals and in the activation of chlorine on polar stratospheric clouds, which leads to ozone destruction (Grosvenor et al., 2007; Fueglistaler et al., 2009). Furthermore, understanding stratospheric hydration/dehydration processes due to deep convection requires accurate measurements of temperature and circulation changes in the TTL region (Randel et al., 2003). The overall effects of convection on the UTLS temperature structure and the contribution of various dynamical processes are still not well quantified. Therefore, understanding how and why tropical deep convection modifies the UTLS temperature structure, as well as how these

temperature changes differ over land or ocean, is important for accurate model representation and climate change research.

The influence of tropical deep convection on the tropospheric temperature structure has been studied prominently over the years. Sherwood et al. (2003) found warm anomalies in the mid-to-upper troposphere over the Indian and western Pacific Ocean convective regions from radiosonde data. Gettelman and Birner (2007) also detected warm anomalies in this region using two climate models. Holloway and Neelin (2007) found cold anomalies in the TTL region using a combination of AIRS satellite and radiosonde data. More recently, Paulik and Birner (2012), Khaykin et al. (2013), along with Xian and Fu (2015) also observed cold anomalies in the TTL using GPS radio occultation (RO) profiles. However, the derived amplitude of temperature anomalies varied significantly between these studies from -0.5 K to as much as -5 K. Additionally, a few studies have been conducted in recent years attempting to quantify the time-varying TTL cooling rate during the life cycle of the convective system, but the results have varied considerably. Sherwood et al. (2003) along with Kim and Dessler (2004) both estimated tropopause cooling rates between -5 and -10 K/d during vigorous convection, while Kuang and Bretherton (2004) found cooling rates on the order of a few tenths of K/d, which indicates a consensus on the TTL cooling rates due to convection has yet to be reached.

In addition, while many studies have revealed atmospheric temperature changes due to deep convection, few have studied the vertical structure of temperature changes inside deep convection on a diurnal scale or analyzed the distinct differences in UTLS temperature changes near deep convection due to land-ocean contrast. Separating land and ocean convection is very important because of the large differences in both the intensity and diurnal variation of the convection due to the land-ocean contrast. For example, based on observations from the TRMM

satellite, the typical peak of land convection is concentrated during the late-afternoon local time while oceanic convection has a much weaker diurnal structure, with a peak seen in the early morning (Liu and Zipser, 2009). Additionally, over land, the mature and more organized convective systems typically appear later in the evening compared to earlier in the afternoon for more isolated convection. Thus, such a strong diurnal variation in frequency and intensity may affect the UTLS temperature structure very differently.

Historically, most atmospheric temperature profiles near deep convection are from radiosonde soundings with limited spatial and temporal sampling, or from operational meteorological analyses with coarse vertical resolution and large uncertainty near the convection. Since the launch of the six-satellite FORMOSAT-3/COSMIC mission (Formosa Satellite Mission 3/Constellation Observing System for Meteorology, Ionosphere, and Climate), GPS RO soundings could fill the gaps by offering global observations of UTLS temperatures with a high vertical resolution in all-weather conditions, even inside clouds (Anthes et al., 2008). Note that the vertical resolution of RO soundings varies from 0.2 km in the lower troposphere to 1.4 km in the upper stratosphere (Anthes et al., 2008), although the effective resolution can be higher near sharp changes in refractivity, such as at the tropopause. The precision has been estimated to be 0.1-0.2% for RO refractivity between 10 and 20 km (Kursinski et al., 1997; Schreiner et al., 2007) while temperature accuracy between 10 and 20 km has been estimated from 0.1 K (Alexander et al., 2014) to 0.15 K (Scherllin-Pirscher et al., 2011). In addition to the all-weather capabilities, the uniform local time sampling of COSMIC (Xie et al., 2010; Scherllin-Pirscher et al., 2011) provides an excellent complement to TRMM for diurnal convection analysis.

The main goals of this research are as follows: (1) to better understand tropical deep convection by identifying its impact on the thermodynamic structure in the UTLS region on a

diurnal scale, (2) to quantify the impact of convection height and intensity on UTLS temperature anomaly magnitude and the role land-ocean contrast plays in determining anomaly structure, and (3) to evaluate the difference in UTLS temperature structure between GPS RO and global reanalysis inside and surrounding convection. Two tropical regions which observe frequent deep convection are chosen for this study: the Pacific Warm Pool (PWP) and the Tropical Atlantic Continental and Oceanic (TACO) region. Instead of looking at the tropics as a single latitude band, the selection of two separate regions allows for the ability to study regional differences of deep convection as well as the impact of the land and ocean contrast on the UTLS temperatures. Also, the inclusion of land and ocean in both regions will allow for enough local time sampling of deep convection for studying the UTLS diurnal temperature variations. In this study, tropical deep convection was identified by TRMM Precipitation Radar observations over the two selected regions from 2007 to 2011. The near-coincident temperature profiles from COSMIC GPS RO and the ECMWF ERA-Interim reanalysis (ERA-I: Dee et al., 2011) were also selected. The structure of this paper is as follows: Section 2 provides background on the COSMIC, TRMM, and ERA-I data used for this research; Section 3 describes the methodology used, including collocation criteria among the three datasets and the temperature anomaly derivations; Section 4 presents the key results of the vertical structure of temperature anomalies in the UTLS due to deep convection, including the diurnal variation, regional differences, and land-ocean contrast; Section 5 provides a brief discussion on the effects of convection on the UTLS thermodynamics; Lastly, the conclusions and future work are summarized in Section 6.

2.2. Data Description

2.2.1. TRMM Precipitation Feature Product

TRMM provides the first detailed and comprehensive dataset of the three-dimensional distribution of rainfall and latent heating over the vastly under-sampled tropical and subtropical regions (Kummerow et al., 1998; Liu et al., 2012). The TRMM satellite is in a circular, non-sun-synchronous orbit inclined at about 35° at an altitude of 403 km since August 2001. Four main instruments onboard provide unique observations to study tropical convection, including the Visible and Infrared Scanner (VIRS) which measures visible and infrared radiances; the TRMM Microwave Imager (TMI) which measures passive microwave radiance; the Precipitation Radar (PR) which measures the radar reflectivity; and the Lightning Imaging Sensor (LIS) that detects lightning flashes (Kummerow et al., 1998). The TRMM Precipitation and Cloud Feature database was originally developed at the University of Utah (Liu et al., 2008). This database generalizes the precipitation and cloud features from TRMM measurements to study tropical precipitation characteristics from the perspective of precipitation systems. The data used here are level-2 data from 2007 to 2011, which uses the PR (area of pixels with 20 dBZ near surface) to identify near-surface Raining Precipitation Features (RPFs) by grouping radar-detected surface rain area.

In this study, “deep” convection is defined as having a 20 dBZ radar echo top height greater than 10 km, which includes the relatively less-intense tropical oceanic convection that can still reach high into the UTLS. It is important to note that the TRMM PR is most sensitive to precipitation-sized hydrometeors (large liquid droplets or ice particles) inside the precipitation systems. Generally, there may be layers of clouds with small ice particles that are undetectable by the PR, so such clouds are actually reaching higher altitudes than the PR echo top height. For example, especially over the ocean, the cloud-top height of these ice clouds are often 5 km or greater than the maximum 20 dBZ height (Liu et al., 2007).

2.2.2. COSMIC RO Data

In this study, GPS RO sounding profiles from the six-satellite FORMOSAT-3/COSMIC mission (Anthes et al., 2008) are used for the same five-year period (2007 to 2011). These are level-2 (reprocessed) profiles retrieved from the COSMIC Data Analysis and Archive Center at the University Center for Atmospheric Research. We use the “atmPrf” product, which provides refractivity and dry temperature (T_{dry}) from near the surface up to ~60 km. At microwave frequencies, the atmospheric refractivity N is related to atmospheric pressure P , temperature T , and water vapor partial pressure e (Smith and Weintraub, 1953):

$$N = k_1 \frac{P}{T} + k_2 \frac{e}{T^2} \quad (1)$$

where k_1 is 77.6 K hPa and k_2 is $3.73 \times 10^5 \text{ K}^2 \text{ hPa}$. The dry temperature is then derived from a modified form of the refractivity equation (1). When atmospheric humidity is very small, the second term in the right-hand side of equation (1) can be neglected (Foelsche et al., 2008) such that:

$$T_{dry} = k_1 \left(\frac{P_{dry}}{N} \right) \quad (2)$$

where P_{dry} is the dry pressure (e.g., the pressure without water vapor) that is derived through hydrostatic integration. In this study, the COSMIC dry temperature is used because it can be treated as an independent satellite retrieval, whereas the “real” RO temperature retrieval relies on a-priori model moisture information. The dry temperature retrieval is appropriate for this study as it is nearly identical to the real temperature in the UTLS region, where moisture is generally negligible since temperatures are lower than 250 K (Kursinski et al., 1997). In this paper, only RO soundings with T_{dry} less than 250 K were used to minimize the impact of water vapor on the temperature. The retrieved profiles are reported as a function of geometric height above mean sea level. COSMIC offers roughly 2000 daily profiles with a relatively uniform global

distribution throughout the study period. Note that tangent point drift during an occultation is not accounted for in this study. The location of each COSMIC profile is at the tangent point nearest to the surface.

2.2.3. ERA-I data

ERA-I is the global reanalysis produced by the European Center for Medium-Range Weather Forecasting (ECMWF). This gridded dataset covers 1979-present in 6 h intervals. The horizontal resolution of the dataset is 0.75° latitude \times 0.75° longitude with 60 vertical levels from the surface up to 0.1 hPa (Dee et al., 2011), among which approximately 11 levels are within 10-20 km. Note that COSMIC GPS RO soundings have been operationally assimilated into ERA-I (Poli et al., 2010) but tangent point drift during an occultation is not taken into account in the ERA-I assimilation.

2.2.4 Study Regions and the Spatial/Temporal Distribution of Tropical Deep Convection

The spatial distribution for deep convection observed by TRMM over the tropics (30°S to 30°N) from 2007 to 2011 is shown in Figure 2.1. There is a total of 477,816 deep convective systems throughout the tropics. Two regions that experience frequent deep convection over the tropical Pacific and Atlantic are identified to study the impact of deep convection on the UTLS temperature structure. The first region, extending from 20°N to 15°S and 80°E to 160°E , is effectively known as the “Pacific Warm Pool” (hereafter referred to as PWP) region. The second region, extending from 15°N to 15°S and 80°W to 35°E , is called the “Tropical Atlantic Continental and Oceanic” (hereafter referred to as TACO) region. Over the PWP, a total of 128,361 deep convective systems are found along with 7,564 COSMIC collocations (profiles within 300 km in space and 3 h after convection occurrence), whereas over the TACO region, 117,869 deep convective systems are observed along with 6,706 COSMIC collocations during

the 5 year period. The PWP has roughly twice as much convection occurring over the ocean than over land, while the TACO region sees most of its convection over the equatorial land areas in Central Africa and South America.

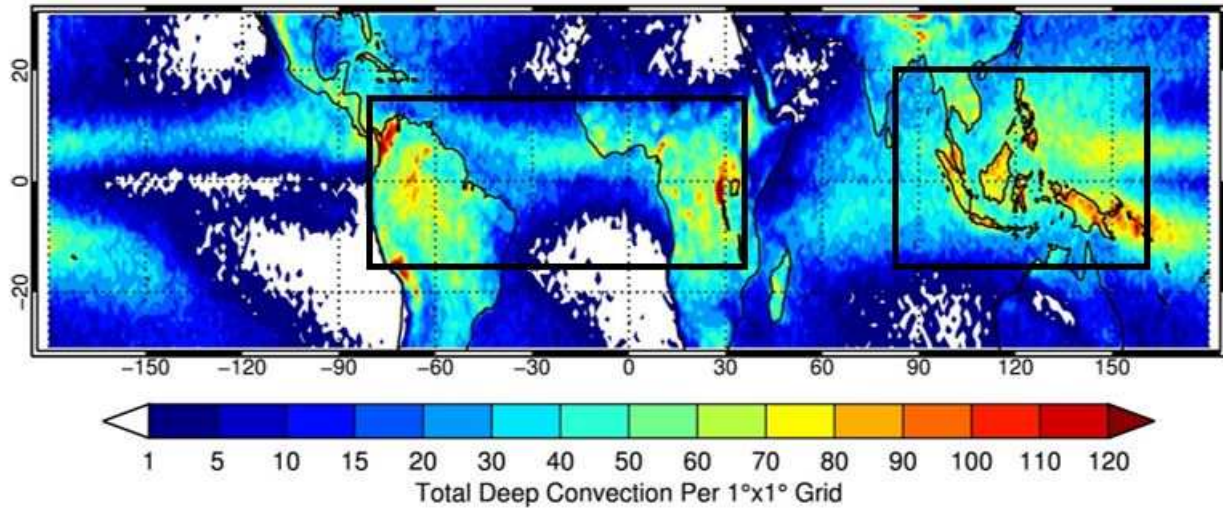


Figure 2.1. Distribution of tropical deep convection (maximum 20 dBZ echo top height > 10 km) observed by Tropical Rainfall Measuring Mission per $1^\circ \times 1^\circ$ grid from 2007 to 2011. The two selected regions of study, the Pacific Warm Pool (PWP) and the Tropical Atlantic Continental and Oceanic (TACO) region, are highlighted by the black rectangle boxes.

Figure 2.2 displays the diurnal distribution of TRMM deep convection systems that have near-coincident COSMIC profiles, with collocations separated by land (red) and ocean (cyan). Since the six COSMIC satellites are distributed equally in local time around the Earth, the diurnal distribution pattern of collocations remains consistent with the full sample of TRMM deep convection (not shown). The PWP deep convection shows a moderate two-peak distribution with good sampling across each local time bin. This owes to a significant number of deep convection observed in this region over both the maritime continent and the open ocean, as the

typical occurrence of land convection peaks in the late-afternoon while oceanic convection has a weaker maximum in the early morning (Liu and Zipser, 2009). Deep convection in the TACO region has a much more pronounced peak during the late afternoon hours due to much of the deep convection occurring over land. However, the smaller amount of oceanic convection still provides enough sampling throughout the day in this region.

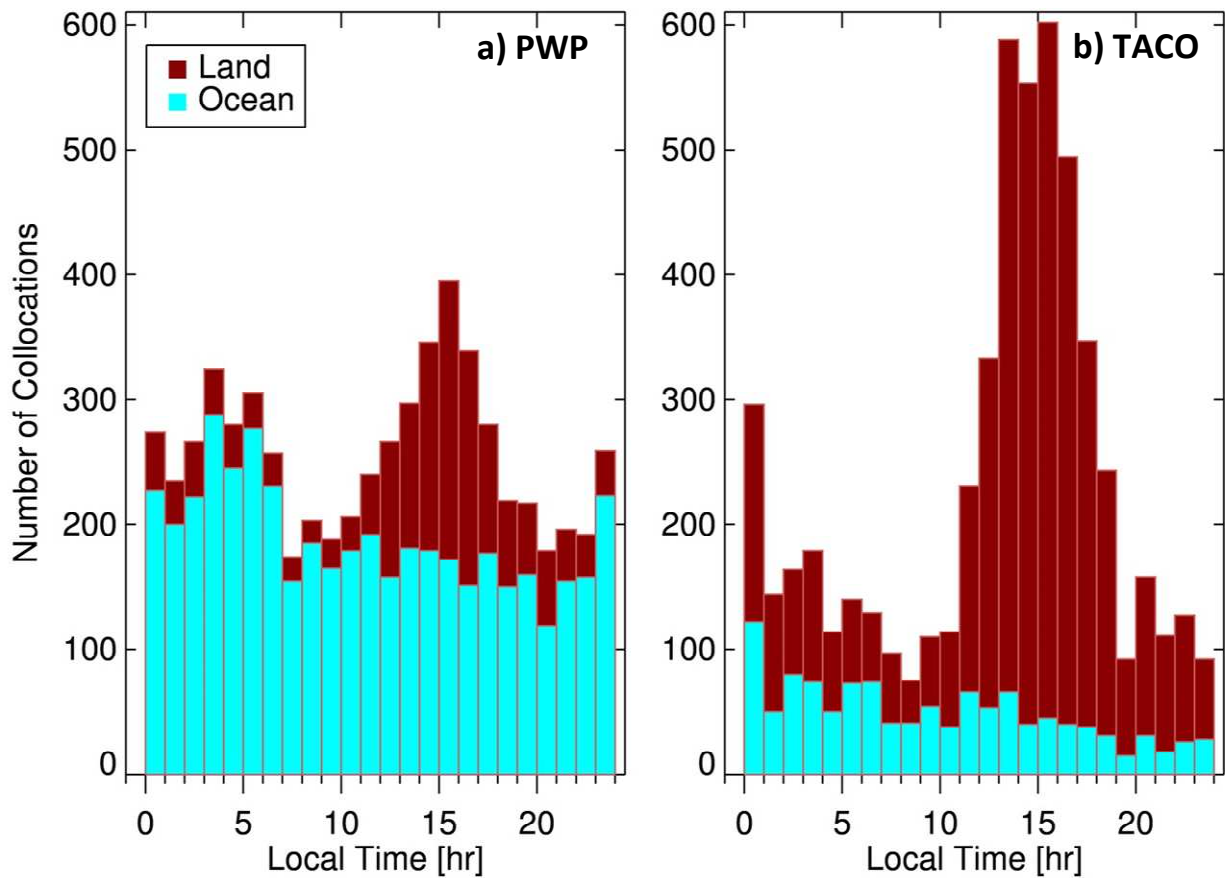


Figure 2.2. Diurnal distribution of the subsampled Tropical Rainfall Measuring Mission deep convective systems that have near coincident COSMIC Radio Occultation profiles within 300 km and 3 h after convection occurrence over the (left) Pacific Warm Pool (PWP) and the (right) Tropical Atlantic Continental and Oceanic (TACO) region, with collocations classified by land (red) and ocean (cyan).

2.2.5. COSMIC/ERA-I Dry Temperature Versus Temperature Differences

As previously discussed, the COSMIC dry temperature is expected to be nearly identical to the real temperature in the UTLS region since temperatures are below 250 K and minimal moisture is likely present. However, the potential impact of this moisture must still be quantified. Near-coincident (within 3 h) COSMIC and ERA-I profiles from the 2007 to 2011 study period in each region (roughly 100,000 each) are identified to represent the background atmospheric temperatures. Furthermore, collocated COSMIC and ERA-I profiles after deep convection occurrence are analyzed to evaluate the moistening effect of convection.

Figure 2.3 shows the ERA-I specific humidity (q) for mean background conditions and after deep convection, along with the corresponding differences between ERA-I temperature and COSMIC dry temperature that occurs due to the presence of water vapor that is not considered in the dry temperature. COSMIC dry temperature has a cool bias compared to the real temperature within 10-13 km due to the presence of significant moisture content within the tropics (Danzer et al., 2014), which is amplified near deep convection. The background specific humidity at 10 km is roughly 0.35 g/kg (PWP) and 0.25 g/kg (TACO), which contributes to a temperature-dry temperature difference of about 3 K (PWP) and 2 K (TACO). The ERA-I specific humidity increases by about 0.1 g/kg at 10 km near deep convection, which further increases the $(T - T_{dry})$ difference by roughly 1 K. As the moisture decreases exponentially with height, the $(T - T_{dry})$ difference also decreases exponentially, with $T \approx T_{dry}$ at about 13 km. Note the larger cool bias within 10-13 km in the PWP due to the presence of more water vapor. This increase in specific humidity after deep convection has a unique impact on the dry temperature anomaly profiles, which will be further discussed later in this text.

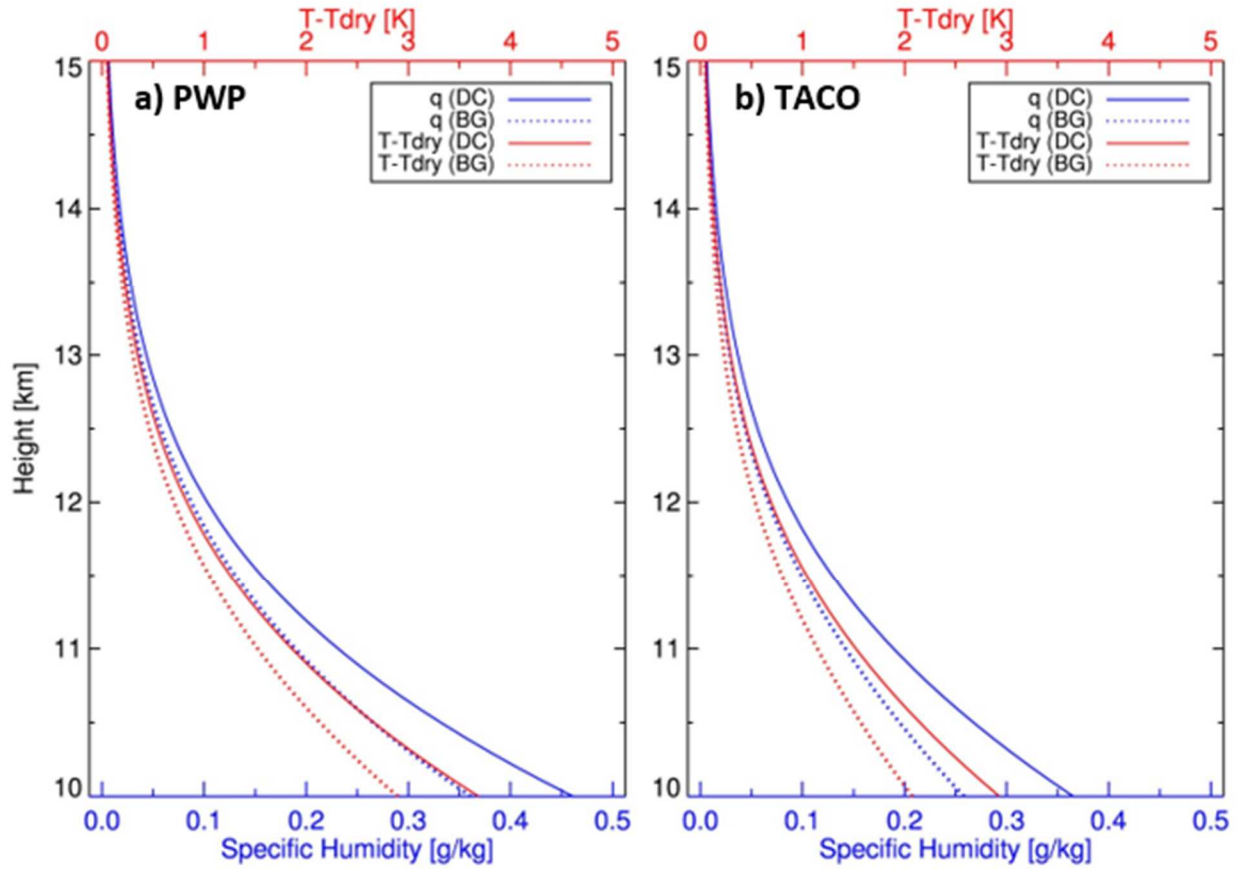


Figure 2.3. ERA-Interim specific humidity (g/kg) (blue) along with the difference between temperature and dry temperature (red) for the mean background conditions (BG, dotted lines) versus after deep convection (DC, solid lines) in the (a) Pacific Warm Pool (PWP) and (b) Tropical Atlantic Continental and Oceanic (TACO) region.

2.3. Methodology

2.3.1 Data Set Collocation and Diurnal Temperature Anomaly Analysis

To capture the thermodynamic structure of the atmosphere inside or near the deep convection, both the COSMIC RO and ERA-I profiles are collocated with deep convection observed by TRMM over the selected regions within 3 h after convection occurrence and within

a 300 km radius of the convection. The time difference between convection and the COSMIC RO/ERA-I temperature profiles is recorded for each pair of collocations. This time and distance threshold is chosen to provide a balance between sampling and direct convective impact. Note that it is necessary to have a threshold large enough to allow for enough samples, but also restrictive enough to observe the direct impact from the convective system. Each COSMIC and ERA-I profile is interpolated to a 10 m uniform vertical grid using a quadratic interpolation scheme and then smoothed to 500 m, which is roughly the native resolution for RO profiles at the UTLS altitude range. The RO profiles within each local time bin are then averaged to generate a composite vertical profile from 10 to 25 km. First, the mean diurnal background temperature profile (using 2-hourly local time bins) is derived from all COSMIC profiles over the two selected regions during the 5 year period. Then, the diurnal variation of UTLS temperature anomalies due to deep convection is calculated as the deviation from the mean background temperature profile at each local time.

2.3.2 Diurnal Variation Analysis

The atmospheric tide is a well-known feature in the UTLS which is driven by daily changes in solar heating, and is responsible for modulating many dynamical, hydrological, radiative, and chemical processes (Xie et al., 2010). The propagating tidal wave, which migrates with the sun, dominates the tropical diurnal variation in the stratosphere and higher altitudes (e.g., McLandress, 1997). In the tropics, the migrating tide increases in amplitude above ~14 km as illustrated by COSMIC temperature soundings (Xie et al., 2010). Two height levels (11 km and 17 km) are chosen to represent the altitude of different temperature anomaly layers observed after deep convection. After the mean background temperatures are subtracted from the temperature profiles near deep convection (using 1-hourly local time bins), a harmonic analysis

with 24-h and 12-h components is applied to the temperature anomalies to compute their diurnal and semi-diurnal amplitudes along with their phases at selected heights. The normal tidal amplitude at these altitudes is calculated based on the mean background temperatures, and its amplitude is compared to the diurnal amplitude observed after convection. As deep convection also exhibits strong diurnal variation, it is important to isolate the contribution of convection to the UTLS diurnal cycle and to determine whether this diurnal cycle is enhanced or suppressed by convective activity.

2.3.3 Convective Intensity Variation Analysis

Additionally, to study the impact of deep convection intensity on the UTLS temperature structure, the TRMM deep convection is categorized based on the system's maximum 20 dBZ and 40 dBZ echo top height using 2 and 1 km-interval bins, respectively. Similarly, the deep convection is also categorized based on its minimum infrared cloud top temperature (CTT) using 10 K-interval bins. The collocated temperature profiles are then grouped into each convective height/CTT bin. Each individual temperature anomaly profile is then derived by subtracting from the background temperature. It is important to note that there is large spatial (e.g., meridional) variation of the UTLS mean background temperatures in the two selected regions. Therefore, instead of using a regional mean diurnal temperature at each altitude as the background (as in Section 3.1), the mean background temperatures are derived using $5^\circ \times 5^\circ$ grids within each region. For example, all COSMIC/ERA-I profiles from 2007 to 2011 are placed into their appropriate grid box and averaged to generate a mean background profile for each grid. Then, the temperature anomaly profile for COSMIC/ERA-I near deep convection can be derived by subtracting the corresponding gridded mean background temperature. These anomaly profiles are accumulated and averaged together to derive a mean anomaly profile for each height bin, with

the number of samples for each subgroup recorded. Furthermore, deep convection over land and ocean are separated and their temperature anomaly profiles for each height bin are also presented.

2.4. Results and Discussion

2.4.1 UTLS Diurnal Temperature Anomalies

As previously mentioned, one of the main goals of this research is to quantify the temperature anomalies due to deep convection and determine their vertical structure in the UTLS, especially on a diurnal scale. Figure 2.4 presents the diurnal distribution of vertical temperature anomalies from COSMIC profiles in the PWP and TACO, respectively. The cold-point tropopause (CPT) height is also derived. In the PWP (Figure 2.4a), warm anomalies are observed (0 to 0.2 K) within ~11-14 km, with slight cooling observed within 10-11 km. A layer of cool anomalies is observed above the warm anomalies within ~14-17 km, ranging from -0.4 K to -0.8 K. Above the cool anomalies, there is a significant layer of warm anomalies of 0.2 K to 1.25 K in a layer from ~17-20 km. Above this warm layer ending around 20 km, slight warm and cool anomalies are seen with no discernable pattern, suggesting no direct connection to convection distribution or frequency at this altitude.

In the TACO region (Figure 2.4b), a similar pattern is evident although stronger anomalies are seen compared to the PWP. Similarly, warm anomalies are observed within ~10-14 km, ranging from 0 to 0.6 K, although slight cooling is still evidenced within 10-11 km. A layer of strong cool anomalies (-0.6 K to -1.5 K) lying above the warm anomalies is observed within ~14-18 km. The height of the strongest cool anomalies is around ~16 km, which is about

1 km below the CPT at ~17 km. Within the 18-20 km layer, a mix of both warm and cool anomalies is observed and no consistent pattern is seen, which is very different from the PWP. However, as shown in Figure 2.2, most convection in the TACO region occurs during the early afternoon through early evening hours (12:00 to 18:00 local time) due to a much higher percentage of convective systems forming over land. Strong cool anomalies (up to -1.25 K) are evident at these local times above 14 km. This could be due to the higher numbers of stronger and deeper land convection triggering an increase in gravity wave activity, which may then propagate upward from the convective sources into the lower to the middle stratosphere (Costantino et al., 2015). Additionally, cooling up to -1 K is observed within 20-25 km around 10:00 to 15:00 local time. The peak anomaly magnitude occurs slightly earlier than the maximum convection frequency over the TACO region (which occurs during the late afternoon hours from the intense land convection over central Africa and the Amazon). At the moment, we do not have a solid physical explanation for this result. Further study to confirm the presence and explain the physical mechanisms of such diurnal cooling at this altitude would be needed.

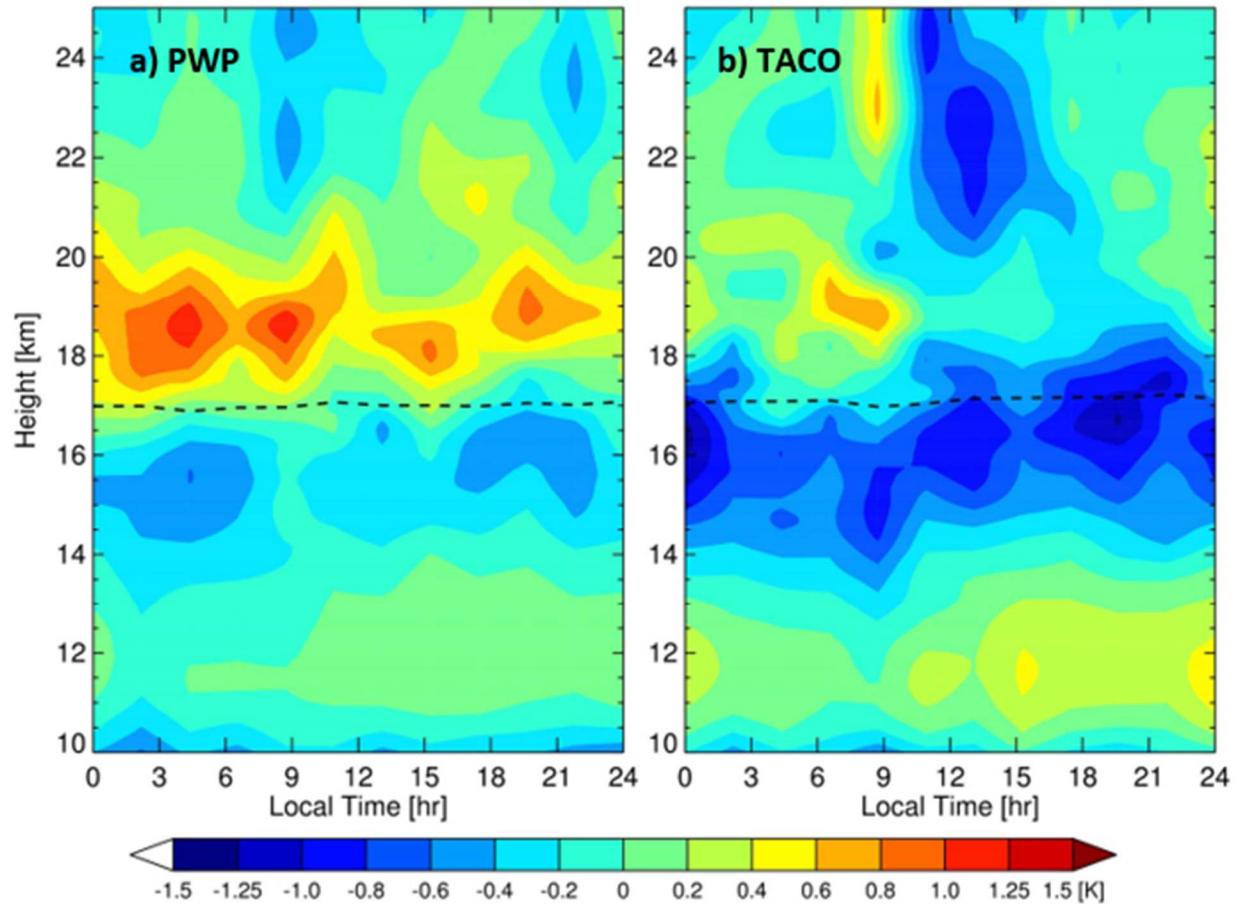


Figure 2.4. Diurnal distribution of COSMIC dry temperature anomalies (K) after deep convection in the (a) Pacific Warm Pool (PWP) and (b) Tropical Atlantic Continental and Oceanic (TACO). Dashed lines represent cold-point tropopause height.

The deep convection frequency (Figure 2.2) seems to have an impact on the diurnal temperature anomaly magnitude. For example, stronger cool anomalies in the 14-17 km layer and warm anomalies in the 17-20 km layer are evident in the PWP during the peak oceanic convection around 2:00 to 6:00 local time (Figure 2.4a). The anomaly magnitudes at these altitudes are slightly reduced in the late morning and early afternoon hours when diurnal convection frequency is a minimum, and then increase in magnitude (and altitude by ~1 km)

during the late afternoon and evening hours when land convection peaks. It is important to note that the oceanic systems generally are of a larger spatial area compared to land convection over the PWP, as the mean (median) size for collocated TRMM convection over land is $4,080 \text{ km}^2$ ($1,140 \text{ km}^2$) while convection over oceans is $6,220 \text{ km}^2$ ($1,420 \text{ km}^2$). This may result in a more significant overall impact of the larger oceanic convection on the COSMIC temperature profiles (as the collocated profiles are less likely to be outside the convection zone). In the TACO region (Figure 2.4b), stronger warming (up to 0.6 K) is evident within the 10-14 km layer in the late afternoon and evening hours, coinciding with the significant peak in land convection at these times. Also, the magnitude of the layer of cold anomalies is generally about 0.5 K stronger and is pushed roughly 1 km higher during the late afternoon and evening compared to the morning hours. This is likely due to deeper and more intense convection occurring during these hours from intense solar heating over land, as the deepest convection has previously been demonstrated to shift the layer of cold anomalies to slightly higher altitudes (Paulik & Birner, 2012). Finally, warm anomalies are displayed during the morning hours within 18-20 km due to the oceanic convection peaking at these times within the region, but the anomalies transition to cool anomalies during the afternoon and evening due to the dominant land convection.

2.4.2 Diurnal Temperature Variation at Different Altitudes

Numerous studies have shown that GPS RO captures the diurnal variation of UTLS temperatures due to migrating tidal waves in the tropics (Zeng et al., 2008; Pirscher et al., 2010; Xie et al., 2010). Here we further investigate the impact of the strong diurnal variation of deep convection on the diurnal variation of temperature in the UTLS. The temperature anomalies are derived at two selected altitudes (11 km and 17 km) and then decomposed into diurnal (24 h) and semidiurnal components (12 h, not shown) using a harmonic analysis. These two altitudes were

chosen to represent the altitude layers exhibiting warm (11 km) and cool (17 km) temperature anomalies as shown in Figure 2.4. Figures 2.5a and 2.5b show the diurnal variation of temperature anomalies for all COSMIC soundings (with collocated convection profiles removed) in the PWP and TACO region, respectively, whereas Figures 2.5c and 2.5d show the diurnal temperature anomalies for COSMIC soundings collocated with deep convection. In both regions, the diurnal variation component (24 h) dominates at both altitudes, while only a small semi-diurnal component is detected.

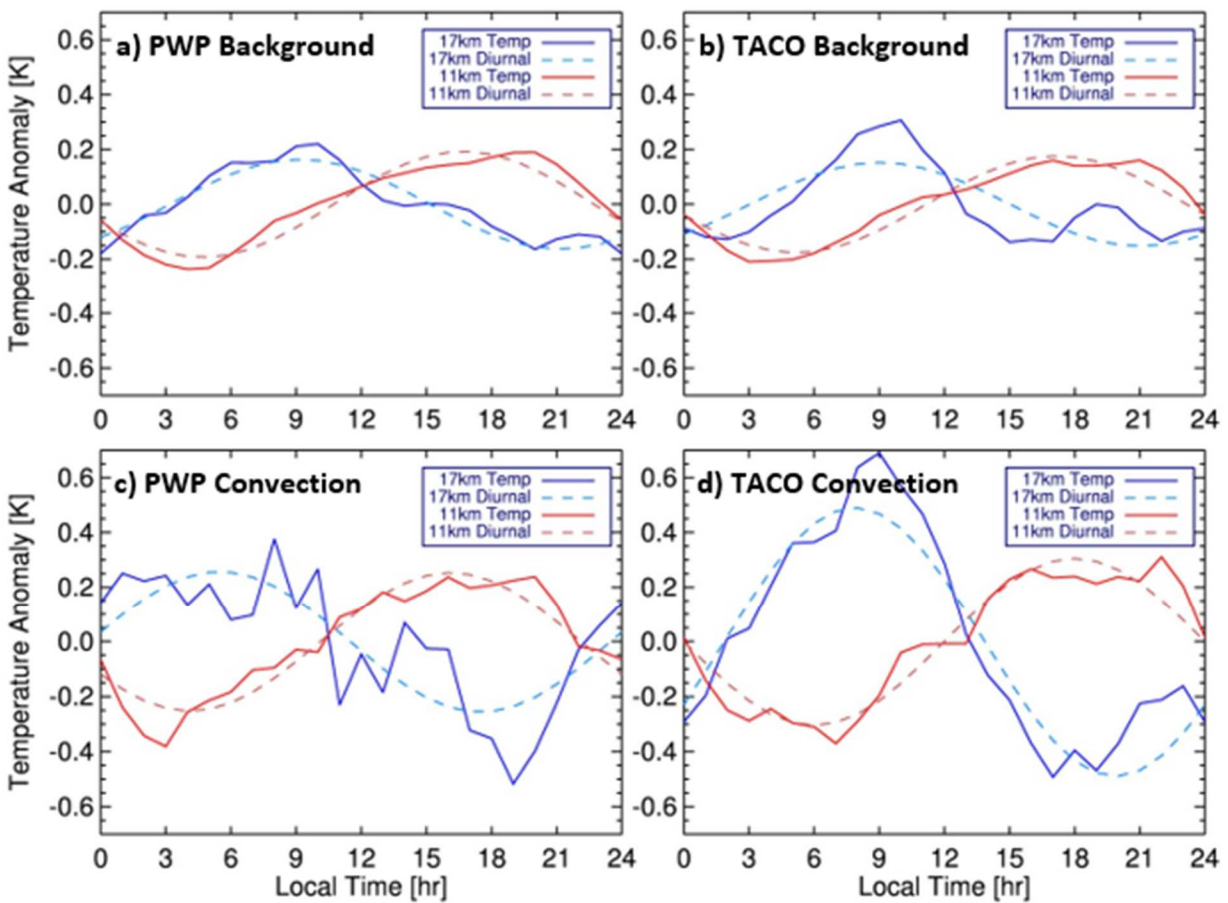


Figure 2.5. Diurnal temperature anomalies (K) in the (a, c) Pacific Warm Pool (PWP) and (b, d) Tropical Atlantic Continental and Oceanic (TACO) region for background conditions (Figures 2.5a and 2.5b) and after deep convection (Figures 2.5c and 2.5d). Anomalies (solid lines) are

shown along with their diurnal components from harmonic analysis (dashed lines) at 11 km (red) and 17 km (blue) using COSMIC profiles.

Figures 2.5a and 2.5b show clear, nearly-identical diurnal temperature anomalies for COSMIC background conditions in both regions, with peak diurnal amplitude of around 0.2 K and a smaller semi-diurnal variation of about 0.05-0.1 K at both altitudes. Moreover, the peak warm anomalies occur at about 17:00 local time at 11 km, and at 9:00 local time at 17 km. Both the diurnal amplitude and phase (local time of the maximum positive anomaly) of the temperature anomalies are highly consistent with the characteristics of the tropical migrating diurnal tides shown in Xie et al., (2010).

More interestingly, a clear diurnal cycle of temperature anomalies with enhanced amplitude and slightly shifted phase are shown for COSMIC soundings collocated with deep convection in both regions. In the PWP (Figure 2.5c), at 11 km, cool anomalies are seen from 22:00 to 10:00 local time and warm anomalies are seen the rest of the day. The diurnal amplitude of the temperature anomalies reaches 0.25 K and the phase is shifted by ~1 h (at ~16:00 local time) compared to the background tide. At 17 km, cool anomalies are seen from about 10:00 to 22:00 local time with warm anomalies the rest of the day. The diurnal amplitude of about 0.3 K is observed and the phase is shifted by ~3 h (at ~06:00 local time) compared to the background tide. Semidiurnal components are small for both heights, with amplitudes less than 0.1 K.

Similarly, in the TACO region (Figure 2.5d), at 11 km, cool anomalies are seen from 00:00 to 10:00 local time and warm anomalies are seen during the rest of the day. Again, the diurnal component dominates with amplitude close to 0.35 K (~0.1 K stronger than the PWP)

with the phase shifted by ~ 1 h ($\sim 18:00$ local time) compared to the background tide. At 17 km, the temperature anomalies show a much stronger amplitude compared to the background conditions, with cool anomalies from about 13:00 to 02:00 local time and warm anomalies in the rest of the day. The diurnal component still dominates, showing an amplitude of about 0.5 K with phase shifted by ~ 1 h ($\sim 08:00$ local time) compared to the background tide. Again, amplitude of the semidiurnal components are much smaller than their diurnal counterparts for both heights, with only around 0.1 K at 11 km and 0.05 K at 17 km. Overall, the amplitude of diurnal temperature variation increases by ~ 0.2 - 0.3 K in both regions after deep convection occurs, which confirms the important role deep convection plays in enhancing the diurnal temperature cycle in both regions.

2.4.3 Impact of Deep Convection Height and Intensity on UTLS Temperature Anomalies

In previous sections, all deep convection with a maximum 20 dBZ echo top height greater than 10 km has been grouped together without differentiating its intensity. However, it is important to quantify the variation of UTLS temperature anomalies based on the convection's intensity, which can be inferred by the maximum radar echo top heights (e.g., 20 dBZ or 40 dBZ) or the infrared CTT (see methodology in Section 2.3.3). COSMIC temperature anomalies near deep convection are divided into subgroups based on these echo top heights or infrared CTT. For example, convection identified as having a maximum 20 dBZ height within 10-11.99 km are grouped together and represented as the convection at 10-12 km, and so forth (Figure 2.6). Similarly, the COSMIC temperature anomalies for various convective intensities categorized by 40 dBZ echo top height and CTT are shown in Figure 2.7 and Figure 2.8, respectively.

2.4.3.1 Deep Convection with Various 20 dBZ Echo Top Heights

Over each region, the COSMIC temperature anomaly profiles for varying convective intensities categorized by 20 dBZ echo top heights are illustrated (Figure 2.6). The results are generally consistent with the diurnal temperature anomalies shown in Figure 2.4, as warm anomalies are observed within 10-14 km and cool anomalies are seen within 14-17 km.

Figure 2.6a shows the mean COSMIC temperature anomaly profiles for all deep convection in the PWP. Warm anomalies are seen at 10-14 km, ranging from a minimum of 0.1 K for the shallower convection to a maximum of 0.5 K near the deepest convection. Cool anomalies ranging from -0.3 to -0.7 K are generally seen above the layer of warm anomalies at ~14-17 km, albeit only for the deeper convection reaching above 14 km. However, within 17-21 km (above the tropopause), anomalies vary from warm to cool, depending on storm intensity. This is discussed more in-depth as the anomalies are analyzed by land and ocean. There is also a distinct increase in temperature anomalies as the convection deepens.

Both land (Figure 2.6b) and ocean (Figure 2.6c) convection display warm anomalies within 10-14 km, with magnitudes increasing up to ~0.5 K as convection deepens. Additionally, within 14-17 km, strong cooling is observed for both land and oceanic convection over the deeper systems whereas basically no anomalies are seen for the relatively shallower oceanic systems. However, significant differences arise in the layer above these altitudes. Within 17-20 km, cool anomalies are observed near land convection for all intensities (ranging from -0.1 to -0.8 K), whereas over oceanic convection, warm anomalies are observed for convection reaching up to 16 km (ranging from 0.3 to 0.5 K) while cool anomalies are only observed for the deepest convection. The overall anomaly pattern (Figure 2.6a) at this altitude reflects the dominant oceanic convection in the PWP. As a result, this confirms that the significant warm anomalies at

17-20 km in Figure 2.4a were caused by the relatively shallower oceanic convection reaching <16 km which dominated the region. While this is a very intriguing development, it is unclear why only the shallower oceanic convection causes such significant warming at this altitude. It is also important to point out that the PWP is known for having a strong diurnal cycle of land-ocean convective propagation. Since the time difference between convection and temperature profile can be up to 3 h, it is possible that the influences from land and ocean convection may be slightly mixed within the results. Finally, it is interesting to note that over both land and ocean, warm anomalies are seen from 23-25 km, which, as previously mentioned, may indicate increased gravity wave activity.

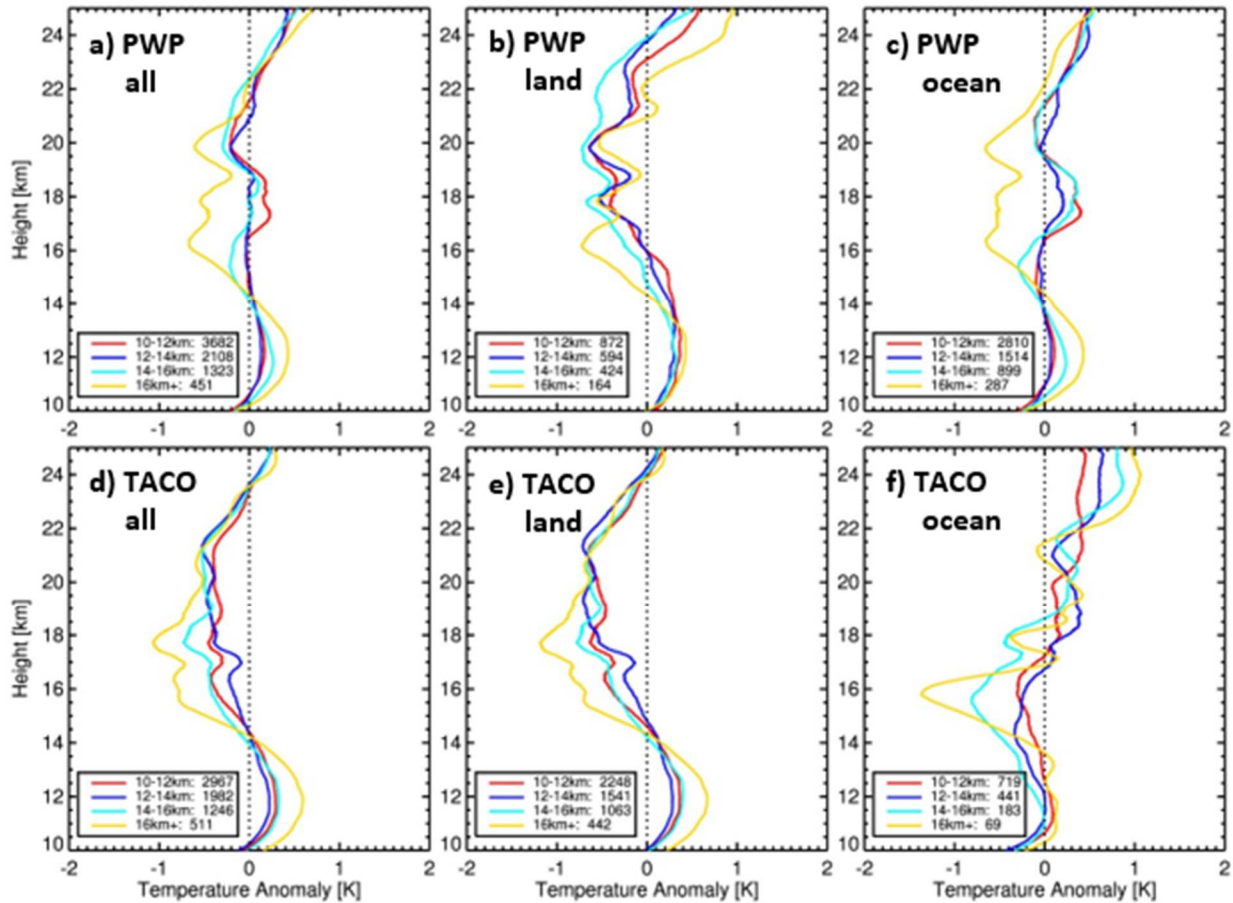


Figure 2.6. COSMIC temperature anomalies (K) near deep convection classified by the PR-derived maximum 20 dBZ heights in the Pacific Warm Pool (top) and Tropical Atlantic Continental and Oceanic region (bottom) for (a, d) all convection, (b, e) convection over land, and (c, f) convection over oceans.

In the TACO region, the overall regional profiles (Figure 2.6d) look much different than the PWP (Figure 2.6a) due to the TACO region having much more land convection than oceanic convection. Again, within 10-14 km, warm anomalies are observed ranging from 0.3 to 0.7 K, with the warmest anomalies occurring for convection in the 16+ km height category (roughly 0.3 K higher than any other category). Within 14-22 km, cool anomalies are seen for all convection

ranging from roughly 0.2 K to 1.1 K. The anomaly magnitudes for all heights at this altitude are much stronger than the PWP. Additionally, the larger anomalies (both warm and cool) correspond to the stronger convection. Since the region has more land convection, the anomalies for land systems in the region (Figure 2.6e) are nearly identical to the overall region anomalies. The oceanic convection (Figure 2.6f) shows larger anomaly variation. Within 10-14 km, weak warming and even weak cooling are observed. Within the cool layer from 14-17 km, the cool anomalies for the shallower convection range from -0.3 to -0.4 K but increase in magnitude rapidly for deepest oceanic systems (over 16 km) up to about -1.4 K. Additionally, contrary to the cool anomalies observed near TACO land convection, warm anomalies of up to 0.4 K are seen near oceanic convection within 17-20 km. While the PWP and TACO region see many similarities in anomaly magnitude and sign near both land and oceanic convection below the tropopause, it is clear there are significant differences between land and ocean convection affecting temperatures above the tropopause in both regions. Both PWP and TACO oceanic convection display significant warming within 17-20 km, while both regions also display significant cooling near land convection at this altitude and agree very well for the most part. This land/ocean convection contrast likely explains the contradictory temperature anomaly signs at this altitude range that has been presented in previous research (Kim and Dessler, 2004; Holloway and Neelin, 2007; Chae et al., 2011; Biondi et al., 2012; Khaykin et al., 2013).

Additionally, an analysis was conducted for PWP ocean and TACO land convection focused on a 5 h window of maximum convective development within each region (not shown). For the PWP ocean, this window is 2:00-7:00 local time, while for TACO land, this window is 13:00-18:00 local time. Temperature anomalies within 10-14 km were very similar to Figure 2.6 in both regions. However, at and slightly above the tropopause, cooling increases by 0.5 K over

TACO land for all echo top heights, while warming increases by $\sim 0.2-0.5$ K for shallower PWP ocean convection and cooling increases by 1 K for 16+ km ocean convection.

Finally, it must be noted that there is a relatively large standard deviation observed for the temperature anomalies at and just above the tropopause (not shown) in both the PWP and TACO regions, regardless of land or ocean surface. This variation reaches a maximum of ~ 4 K at 18 km and indicates that both significant positive and negative anomalies can be observed at these altitudes. Thus, some amount of caution must be taken when interpreting the results at and just above the tropopause as universal cooling or warming (depending on surface type). However, these mean profiles have been verified with the Student's t-test and proved to be statistically significant. They display the general trend of the data and are still quite useful for showing the overall picture.

2.4.3.2 Deep Convection with Various 40 dBZ Echo Top Heights

Previous sections used the PR-derived 20 dBZ maximum echo top height to gauge the intensity of deep convection and determine its maximum impact. Here, we further select the strongest deep convection using the PR-derived 40 dBZ maximum echo top height. Note that these deep convective systems are the same systems that have a maximum 20 dBZ echo top height over 10 km with a COSMIC collocation, but exclude any convective systems not reaching 40 dBZ reflectivity. As a result, 806 deep systems are removed in the PWP (10.7%) and 617 are removed in the TACO region (9.2%). The deep convective systems are divided into subgroups based on maximum 40 dBZ echo top height with 1 km-vertical interval bins. For example, " <4 km" indicates all convection with a 40 dBZ height under 4 km. Note that the 40 dBZ intervals are different for land and ocean since convection intensity varies significantly depending on surface type (e.g., 40 dBZ heights are generally much higher over land). Therefore, PWP and

TACO “all” figure panels are not included and instead we only focus on land and ocean separately.

In the PWP (Figures 2.7a and 2.7b), warm anomalies (0.1 to 0.5 K) are seen within 10-14 km over both land and ocean. The anomalies increase in magnitude for stronger convection over the ocean but remain rather constant over land. However, in the TTL region (14-17 km), the anomalies show no consistent pattern for the different intensities and vary from slight cooling to even slight warming. This variation is most pronounced over land, with significant warming displayed for the highest 40 dBZ heights (which is contrary to what was expected). Within the layer above the tropopause (17-20 km), significant warming is evident for oceanic convection and actually displays the highest magnitude for the weakest convection (up to 0.5 K). Over land (Figure 2.7b), near-neutral temperatures to strong cool anomalies are observed, with the weakest cooling signature displayed for the highest 40 dBZ echo top heights.

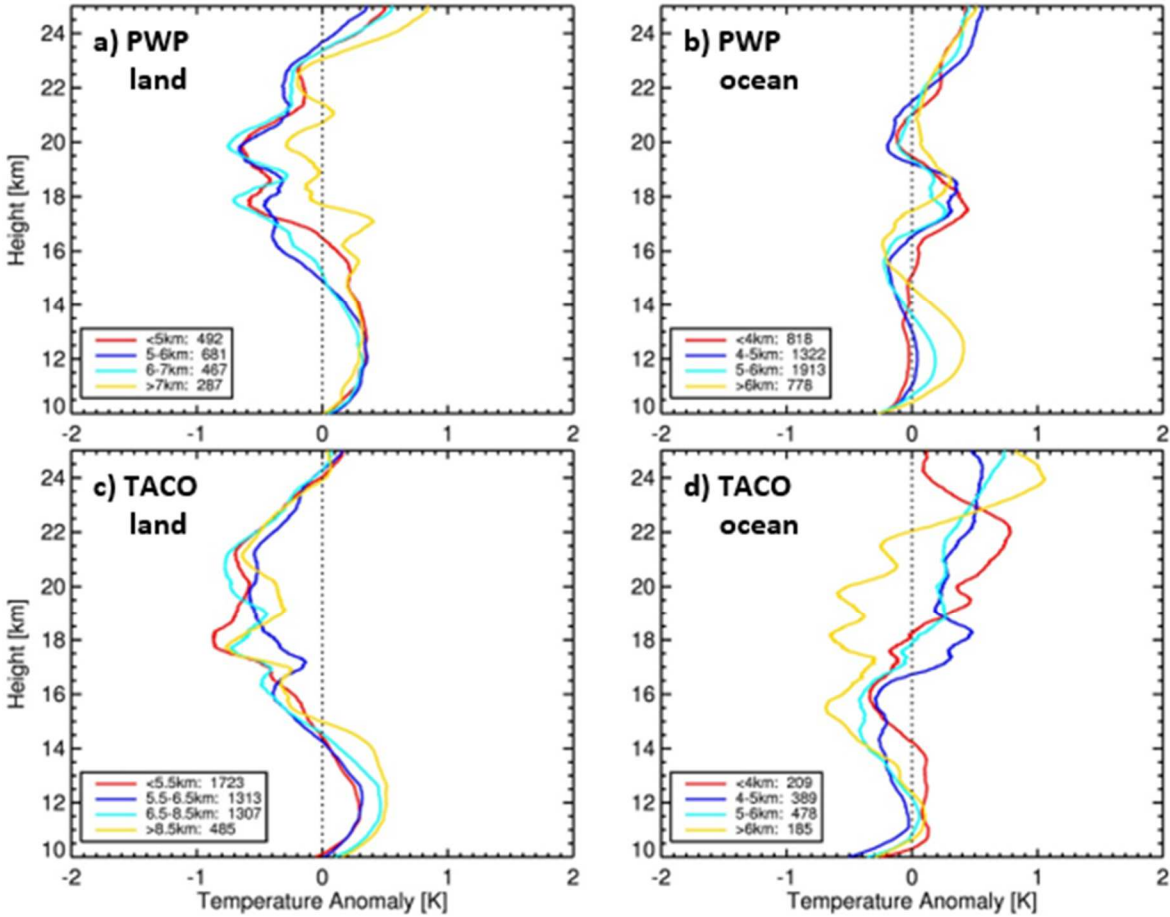


Figure 2.7. COSMIC temperature anomalies (K) near deep convection classified by the PR-derived maximum 40 dBZ heights in the Pacific Warm Pool (top) and Tropical Atlantic Continental and Oceanic region (bottom) for (a, c) convection over land and (b, d) convection over oceans.

In the TACO region (Figures 2.7c and 2.7d), warm anomalies are observed from 10-14 km (0 to 0.5 K) with clearly increased amplitude for stronger convection over land only (Figure 2.7c). Near land convection, cool anomalies are observed from 14-24 km (-0.3 to -1 K), which resembles the anomaly pattern from Figure 2.6e. However, near oceanic convection, a mix of warm anomalies (near weaker convection) and cool anomalies (near stronger convection) are

displayed. Moreover, no consistent pattern is seen for the different intensities and the strongest cooling over land is actually observed near the least intense convection (Figure 2.7c). This result implies that the more intense convection indicated by higher 40 dBZ echo top heights do not necessarily reach higher altitudes or result in a more significant impact to the thermodynamic structure of the UTLS. This could also be explained by the convective stage of development, which we do not consider in this study. Higher 40 dBZ echo top heights are generally associated more closely with early stage convection, while these heights typically decline in the later stages. As a result, early stage convection likely would have less time to affect the surrounding temperature environment. In short, convection's maximum 40 dBZ echo top height is not a robust indicator of the magnitude of UTLS temperature anomalies near deep convection.

2.4.3.3 Deep Convection with Various Minimum Infrared CTT

The minimum infrared (IR) brightness temperature of the clouds above deep convection is a good indicator of the maximum altitude the convective cloud reaches. Here, we again regroup the same deep convective systems (with maximum 20 dBZ height above 10 km) according to their minimum IR brightness CTT with 10 K-interval subgroups. The COSMIC temperature anomalies are then evaluated according to the convective CTT. Also, note that a CTT cutoff of 250 K is used to filter convection with pixels that are likely contaminated by the surface or lower-altitude clouds, since all convection is required to reach at least 10 km and will have a CTT below this value. This results in roughly 2% of the collocations removed in each region.

In the PWP (Figures 2.8a-2.8c), a distinct pattern is evident. Within 10-14 km, slight to moderate warming is seen for both land and ocean convection, but much stronger warming (>0.5 K) is seen for the deepest convection with coldest CTT (<190 K). Within 14-17 km, slight warm

anomalies are seen for the comparatively shallow systems (e.g., warmer CTT) over both land and ocean, while slight cooling is seen for systems within 190-200 K and very strong cooling (reaching as much as -1.1 K) is observed for systems below 190 K. Note that 1,278 deep systems have CTT below 190 K in the PWP (very deep convection) and the anomaly signature is much different than the warmer and shallower systems, where minor warm anomalies are observed at this altitude. Above 17 km, a distinct layer of warm anomalies is observed near oceanic convection for all CTT (Figure 2.8c), whereas cool anomalies are evident near land convection (Figure 2.8b).

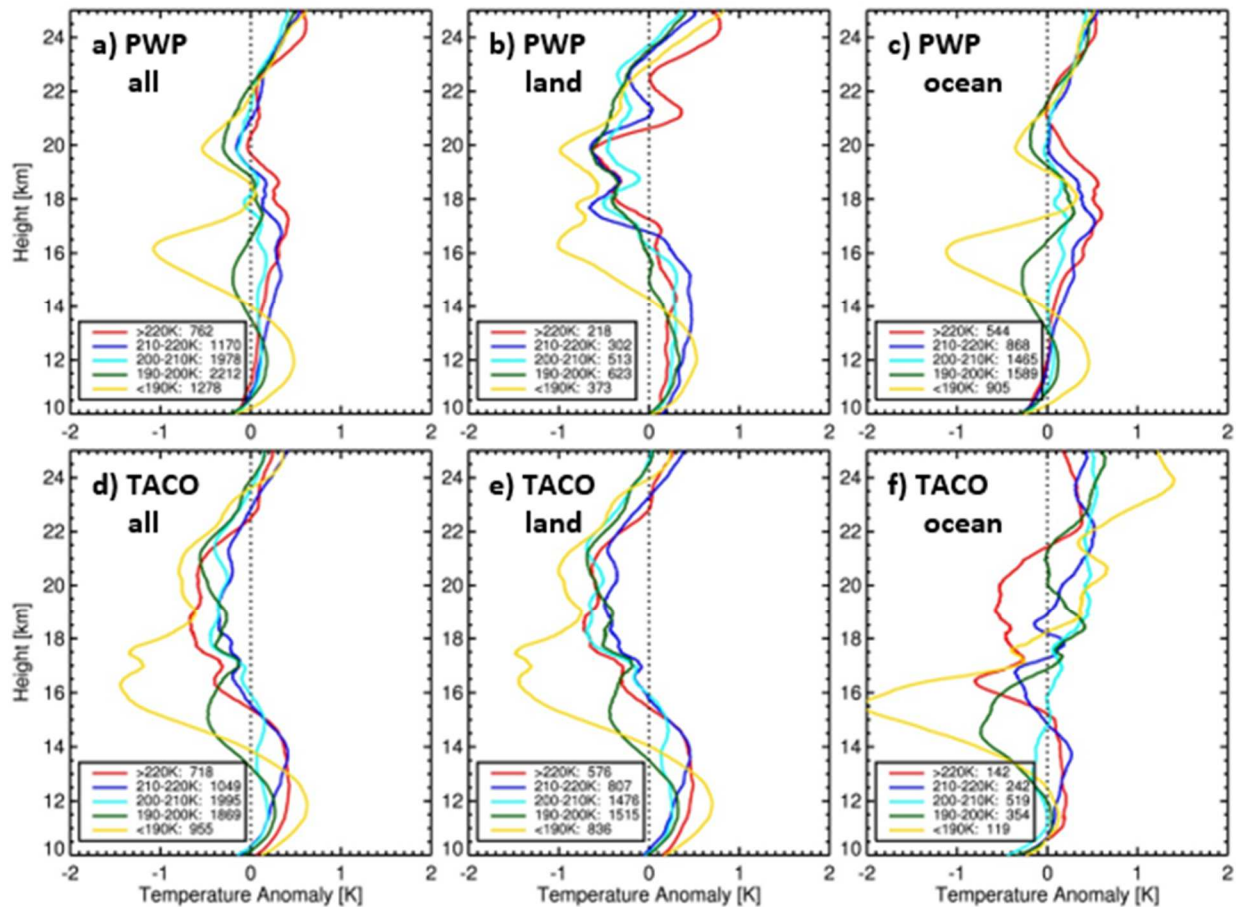


Figure 2.8. COSMIC temperature anomalies (K) near deep convection classified by the VIRS minimum IR brightness temperature in the Pacific Warm Pool (top) and Tropical Atlantic

Continental and Oceanic region (bottom) for (a, d) all convection, (b, e) convection over land, and (c, f) convection over oceans.

In the TACO region (Figures 2.8d-2.8f), the strongest warm anomalies within 10-14 km are again associated with the coldest cloud tops, although it is interesting to note that systems over the ocean in this region do not experience this same increase in warm anomaly magnitude (or even see much warming at all) at this altitude. Within 14-17 km, universal cooling is seen for both land and oceanic convection with the coldest CTT (<190 K), reaching a maximum of about -2 K over the ocean, while the warmer and shallower systems display a mixture of slight warm anomalies (ocean) or slight cool anomalies (land). Additionally, the transition height from warm to cool anomalies varies depending on CTT category and is no longer at a fixed height around 14 km. Differences in temperature anomalies between land and ocean are seen above the tropopause, such as oceanic convection displaying moderate warming while land convection displays moderate cooling. However, in short, the minimum IR brightness temperature is a much better indicator of the anomaly magnitude observed from deep convection compared to using the 40 dBZ convective intensity. A robust pattern is seen for deep convection when progressing from the warmer to the coldest cloud tops, while no robust pattern is evident when progressing from weaker to the most intense convection.

It is important to analyze the relationship between 20 dBZ echo top height and minimum IR temperature (e.g., the CTT) more in-depth, considering the differences in results displayed for these convection characteristics in the previous figures. Figure 2.9 shows a two-dimensional histogram of the temperature anomalies at 16 km altitude for deep convection based on its 20 dBZ height and minimum IR temperature in the PWP and TACO regions with convection

separated by land and ocean. The altitude of 16 km is chosen due to its proximity to the tropopause and because it previously displayed the strongest cooling (Figure 2.8). The grid spacing is 0.5 km for 20 dBZ height and 5 K for minimum IR temperature. Note that grids containing at least five convective temperature anomalies are shown, although almost all have at least 20 and many have more than 50 anomalies. A remarkably clear pattern is displayed in both the PWP and TACO regions over both land and ocean. In the PWP (Figures 2.9a and 2.9b), warm anomalies (up to 1 K) occur at 16 km for the relatively shallower convection (CTT ranging from 240 K to as low as 190 K). As the CTT become colder, the anomalies quickly transition to strong cooling with a negative slope, generally ranging from -2 to -4 K. The cool anomalies typically begin at CTT ~200 K for the lower 20 dBZ heights (e.g., 10 km) and the CTT reach as low as ~170 K for the highest 20 dBZ heights (e.g., 18 km), and this pattern occurs over both land and ocean. The same general pattern is evident in the TACO region as well (Figures 2.9c and 2.9d), although it is interesting to note that cool anomalies are observed over both TACO land and ocean convection for the warmer CTT with 20 dBZ heights between 10-12 km. Also, anomaly magnitude is strongest for oceanic convection over the PWP whereas it is strongest for land convection over the TACO. A stronger relationship for anomaly sign/magnitude is clearly seen for CTT compared to 20 dBZ height. Moderate warming is observed for the warmer CTT and extremely strong cooling is displayed only for the coldest CTT, whereas when looking at specific 20 dBZ heights (e.g., 14 km), both warming and cooling is observed. This indicates that 20 dBZ echo top height does in fact mix up true convection tops to some extent. For example, as previously mentioned, it is possible that one convective system may have a 20 dBZ height of 14 km with a CTT of 205 K (which indicates a similar altitude cloud top compared to the 20 dBZ height) whereas another system may display a 20 dBZ height of 14 km with a CTT of 185 K

(difference of ~ 3 km to the convective top). However, cooler CTT alone does not always indicate a more significant convective impact to UTLS temperature anomalies. For example, if one focuses on a specific CTT (e.g., 200 K or even 190 K), both warm and cool anomalies are observed, depending on the 20 dBZ height of the convection. Therefore, a combination of analyzing the convective CTT and 20 dBZ echo top height is needed to obtain the full picture of convective effects to the surrounding temperature environment.

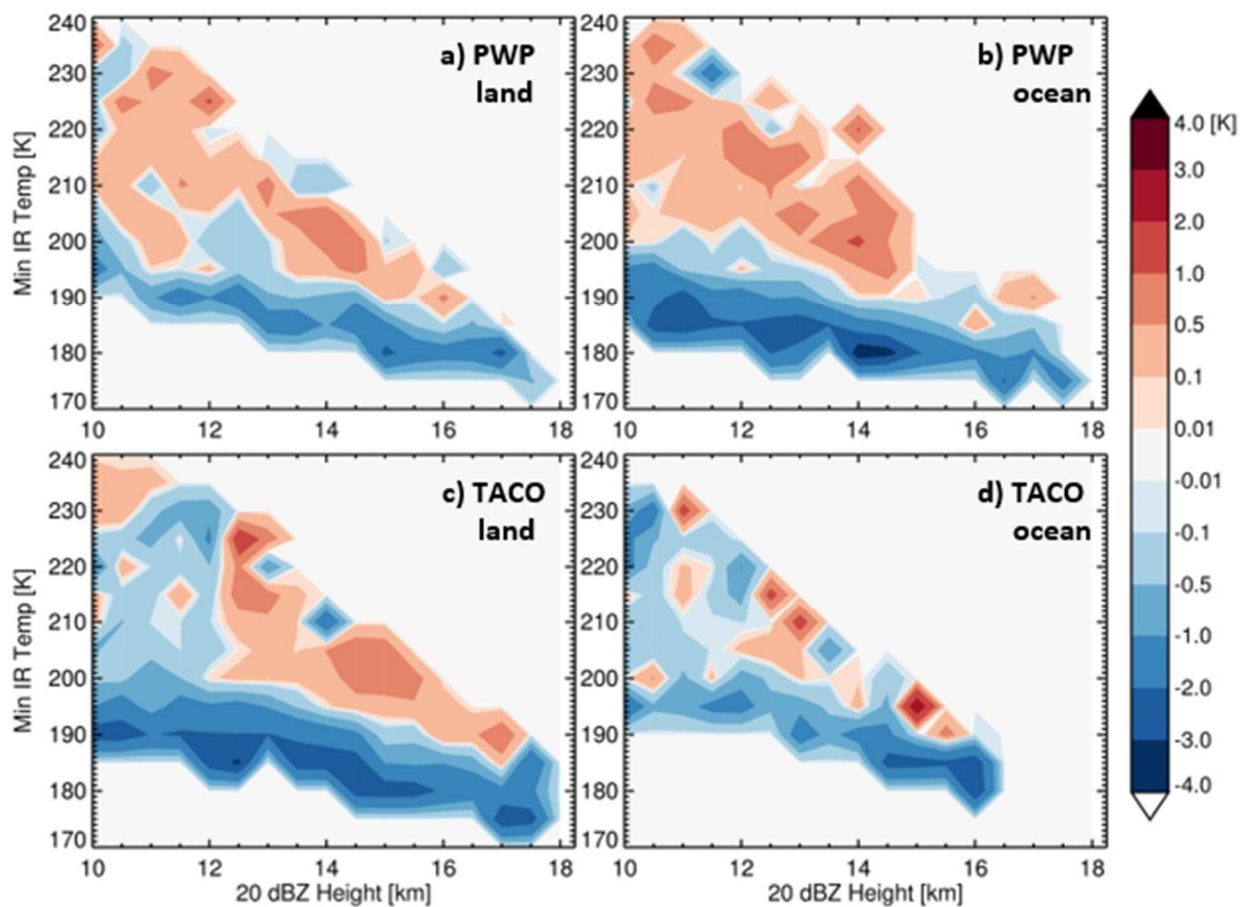


Figure 2.9. Two-dimensional histogram of the COSMIC temperature anomalies (K) at 16 km altitude near deep convection classified by the PR maximum 20 dBZ echo top height and VIRS minimum IR brightness temperature (CTT) in the Pacific Warm Pool (top) and Tropical Atlantic

Continental and Oceanic region (bottom) for (a, c) convection over land and (b, d) convection over oceans.

2.4.4 ERA-I Results Comparison

The final results section of the paper summarizes the comparison of ERA-I temperature anomalies to the previous results from COSMIC. The temperature anomalies for various deep convection heights are derived from ERA-I profiles (Figure 2.10), which show a similar vertical structure to the COSMIC anomalies (Figure 2.6) but with some key differences. The transition height from warm to cool anomalies in ERA-I varies from 12-14 km instead of remaining generally fixed at ~14 km in COSMIC. Additionally, significant differences in anomaly sign and magnitude are evidenced for ERA-I just above the tropopause. The differences seen within ~10-12 km are mainly due to temperature (ERA-I) and dry temperature (COSMIC) differences, which will be discussed in more detail shortly.

In the PWP (Figures 2.10a-2.10c), ERA-I shows generally weak warm anomalies within 12-14 km. Additionally, ERA-I generally shows cool anomalies for all deep convection within 14-17 km whereas COSMIC displays much more variance in both the sign and magnitude depending on land and oceanic convection. ERA-I displays nearly universal strong warm anomalies within 17-20 km over both land and ocean for all deep convective systems, whereas COSMIC indicates warm anomalies at this altitude only for the oceanic convection below 16 km (Figure 2.6). These ERA-I warm anomalies reach as strong as 1 K for the shallower oceanic convection and diminish in magnitude for the deepest convection.

In the TACO region (Figures 2.10d-2.10f), ERA-I agrees better with COSMIC near oceanic convection while still having some differences near land convection. A distinct thick layer of strong cool anomalies is seen within 14-24 km (with a peak around 17 km) in COSMIC land observations (Figure 2.6e). However, this cooling layer shrinks to be within 14-17 km with a reduced peak anomaly at a lower altitude (16 km) in ERA-I (Figure 2.10e). ERA-I anomalies then generally transition to near-neutral around the tropopause over land. Interestingly, ERA-I agrees with COSMIC much better near oceanic convection, with near-neutral conditions below 14 km and strong cool anomalies within 14-17 km, followed by a warming pattern above the tropopause (although ERA-I displays noticeably stronger warm anomalies within 17-22 km). Also, above 23 km, both COSMIC and ERA-I display warming in both regions with similar amplitudes. It was thought that this altitude range (23-25 km) would see minimal direct impact from convection since the convection rarely penetrates above the tropical tropopause near 17 km, but this clearly is not the case and could pose an interesting topic for future research.

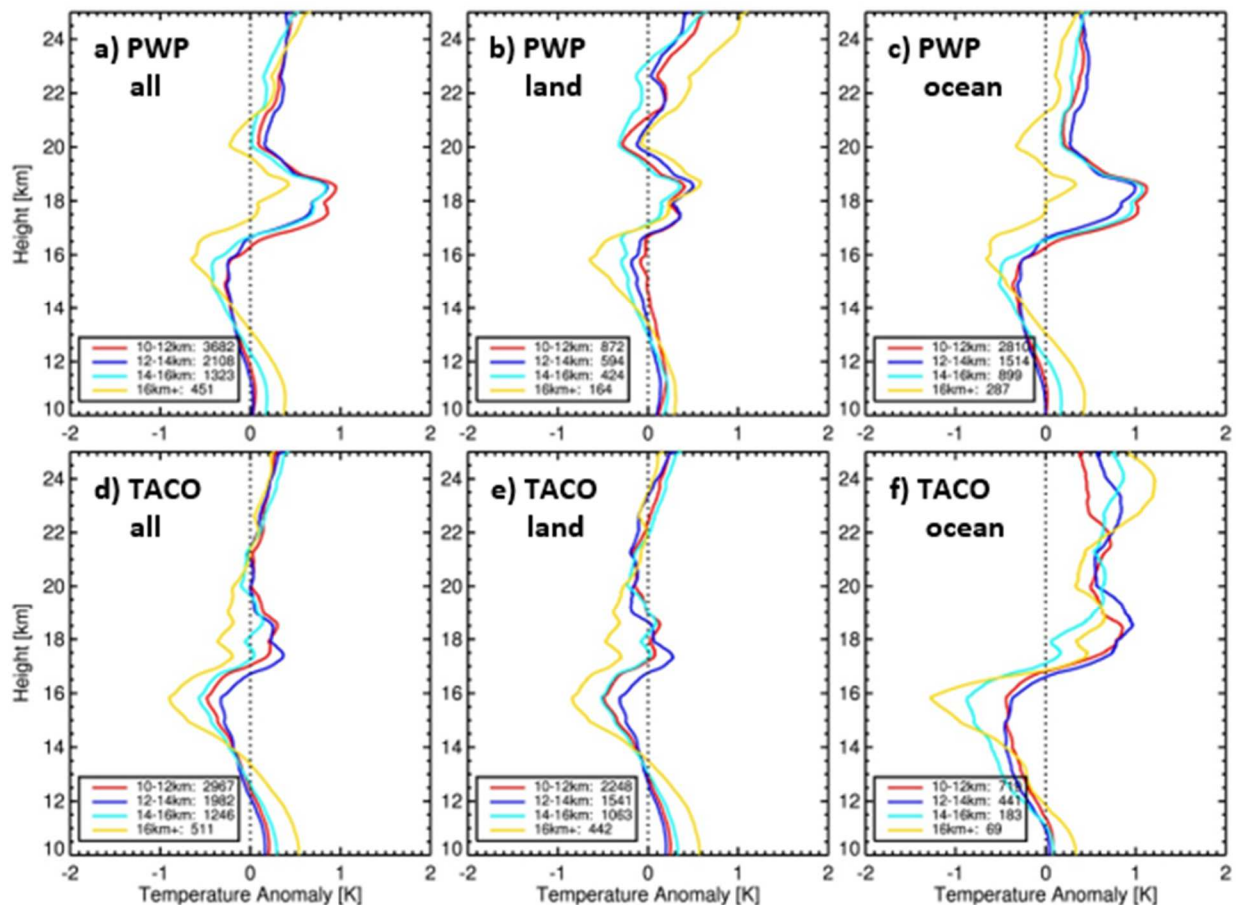


Figure 2.10. ERA-I temperature anomalies (K) near deep convection classified by the PR-derived maximum 20 dBZ heights in the Pacific Warm Pool (top) and Tropical Atlantic Continental and Oceanic region (bottom) for (a, d) all convection, (b, e) convection over land, and (c, f) convection over oceans.

One major difference between the temperature anomaly profiles of COSMIC and ERA-I in Figures 2.6 and 2.10 is seen between 10-12 km. COSMIC demonstrates mainly cool anomalies, especially from 10-11 km, while ERA-I indicates collective warm anomalies at this altitude. Due to the overall increase in atmospheric moisture content near convection, the dry temperature profile near convection is cooler than it would be otherwise (assuming the real

temperature profile is held constant) because of an increased contribution to the temperature profile from moisture. The ~ 0.1 g/kg increase in specific humidity at this altitude near convection (Figure 2.3) results in a 0.4% increase in refractivity (not shown), and, in turn, a 0.8 K decrease in dry temperature. This decrease in dry temperature, combined with the overall increase in real temperatures of roughly 0.4 K due to convective latent heat release at this altitude, results in an “apparent” cooling of 0.4 K at 10 km in the dry temperature profile. This was observed when the ERA-I temperature anomalies were converted to dry temperature anomalies (not shown) using the modified form of the refractivity equation (2). After this conversion, the dry temperature anomalies from ERA-I become almost identical to the COSMIC anomalies between 10-12 km, confirming the consistency between the two datasets at this altitude.

2.5. UTLS Convective Impact Discussion

There are a few likely explanations for the influence deep convection has on the temperature structure (anomalies) seen in the preceding figures. Previous research has characterized the warm convective temperature anomalies observed throughout the middle troposphere as being due to latent heat release in-and-near convective clouds (Randel et al., 2003; Gettelman and Birner, 2007). However, the cool convective temperature anomalies observed throughout the TTL region in this study are not as easily explained. Holloway and Neelin (2007) showed that as gravity waves spread the warming due to convective heating through the free troposphere, hydrostatic pressure gradients will extend above the heating, causing divergence, ascent, and adiabatic cooling aloft. The convective cold-top should be thought of as an intrinsic response to convective heating, and as an inherent part of quasi-

equilibrium temperature adjustment (Holloway and Neelin, 2007). These cold anomalies have been shown to be associated with convectively-coupled gravity waves, but the amount of cooling has varied significantly from study to study (Randel et al., 2003; Sherwood et al., 2003; Biondi et al., 2012). Khaykin et al. (2013) mentioned two possible cooling mechanisms in the TTL region: the first being non-migrating tides generated by convective diabatic heating, possibly interacting with migrating tides and gravity waves (Potter and Holton, 1995); and the second being the systematic injection and turbulent mixing of adiabatically-cooled air by cross-tropopause updrafts (Danielson, 1982). It has been known for many years that convection can generate gravity waves with long vertical wavelengths, as convection involves a time-varying thermal forcing associated with latent heat release that can interact with overlying stable layers and shear in complex ways that are not fully understood (Fritts and Alexander, 2003). One of the difficulties in characterizing convective gravity wave sources is their inherent intermittency. However, Hindley et al., (2015) has recently been able to identify gravity wave hotspots and calculate gravity wave momentum fluxes using COSMIC GPS profiles. As a result, this topic will be investigated more in future research. Again, this study confirms the presence of warm anomalies due to convection throughout the middle troposphere and cool anomalies within the TTL region. In the layer above the cloud-top from ~17-20 km (above the cool anomalies), previous studies have shown both warming and cooling effects. Chae et al. (2011) and Biondi et al. (2012) both showed warm anomalies, with the former indicating warming along with downward motions above the convection. Their hypothesis was that the strongly divergent flow and turbulent mixing near the cloud tops would mechanically drag the air just above the cloud outward. By continuity, this would pull (relatively) warmer lower stratospheric air down from above the clouds, explaining the observed subsidence and warm temperature anomalies (Chae et

al., 2011). They also inferred that the subsidence and warming were part of a Kelvin wave, and that this feature could affect cloud-top heights. Again, similar to previous research, both warming and cooling were observed in this study just above the tropopause. However, the observed temperature anomalies really depend upon the properties of convection and how long the convection has been influencing the environment. Therefore, the differences in anomaly sign and magnitude above the tropopause shown here are dependent on three factors: 1) region of interest; 2) whether convection formed over land or ocean within the specific regions; and 3) maximum height of the convection. Additional research confirming these results above the tropopause by analyzing other regions of interest composed of both land and oceanic convection would likely be a beneficial study.

2.6. Conclusions

In this research, the impact of tropical deep convection on the thermodynamic structure in the UTLS region is studied by collocating deep convection observed by the TRMM Precipitation Radar with COSMIC GPS RO soundings and ERA-I reanalysis from 2007 to 2011. The UTLS diurnal temperature anomalies after deep convection are analyzed in both the PWP and the TACO Region. Warm anomalies ranging from 0.2 K to 0.8 K are generally observed within 10-14 km, then transitioning to a stronger layer of cool anomalies ranging from -0.4 to -1.5 K within 14-17 km, and finally back to a significant layer of warm anomalies in the PWP or cool anomalies in the TACO region up to 1 K within 17-20 km.

Unique diurnal temperature anomaly patterns are seen after deep convection at the two selected altitudes within the layer of warm anomalies (11 km) and cool anomalies (17 km) in

both regions from COSMIC profiles. The temperature anomalies show a diurnal amplitude of 0.3-0.5 K and the semidiurnal component limited to 0.1 K or less in both regions. Moreover, the amplitude of diurnal temperature variation increases by 0.2-0.3 K in both regions after deep convection occurs, which confirms the important role deep convection plays in enhancing the UTLS diurnal temperature variation in the tropics.

There is a clear impact of convection depth on the vertical temperature anomaly structure when classifying convection based on its maximum 20 dBZ echo top height. The general intensity/height of convection plays a significant role in determining the magnitude of temperature anomalies in both regions, as a distinct increase in temperature anomalies is observed near the deeper and stronger convection. Additionally, land-ocean contrast also plays a significant role. Over land, warm anomalies are generally observed within 10-14 km which range from 0.1 to 0.8 K, transitioning to a layer of cool anomalies within 14-22 km that range from -0.3 to -1.5 K (with more variation evident within this altitude), and finally back to warm anomalies between 22-25 km. However, over oceans, the layer of cool anomalies generally is only within 14-17 km and a layer of warm anomalies develops above the tropopause within 17-20 km, ranging from 0.2 to 0.5 K. The different pattern of warm and cool anomalies above the tropopause near oceanic and land convection warrants continued research. ERA-I 20 dBZ temperature anomalies generally agree well with COSMIC in both regions, albeit with some differences in magnitude and vertical extent (e.g., ERA-I displays much stronger warming above the tropopause over both land and ocean).

COSMIC temperature anomalies for various convective intensities, categorized by 40 dBZ echo top heights and the minimum IR CTTs, were also analyzed. The results show that deep convection with higher 40 dBZ heights do not necessarily lead to a larger magnitude of cool

anomalies near the tropopause. This implies that presumably stronger deep convection with higher 40 dBZ heights do not necessarily reach overall higher altitudes or result in a more significant impact to UTLS temperatures compared to less intense convection. On the other hand, minimum IR CTTs (especially <190 K) is a better indicator of the magnitude of anomalies observed near deep convection compared to 40 dBZ echo top heights, as a robust pattern of increasing temperature anomalies for convective systems with colder (taller) cloud tops is observed. Additionally, it is shown that a combination of the minimum IR CTT and 20 dBZ echo top height is needed to obtain the full picture of convective effects to the UTLS temperature environment.

In addition to the previously-discussed limitations of the convective proxies used in this study (20/40dBZ echo top height and minimum IR brightness temperatures), the relatively short time period analyzed is a noteworthy limitation. This is mainly true when sampling numbers are slightly low in some diurnal bins when the deepest convection is relatively rare. Note that the GPM mission is continuing to monitor convection after TRMM, and the upcoming COSMIC-2 mission will triple GPS RO measurements over the tropics. Adding significant sampling will likely benefit future studies on this topic and especially help understand the fine anomaly structures seen at higher altitudes. Finally, more studies on dynamical processes in the UTLS are required to further improve the representation of deep convection in weather and climate models.

Acknowledgements

Funding for this research was provided by NASA grants (NNX14AK17G and NNX15AQ17G). Chuntao Liu was supported by NASA-NNX16AD76G and NSF-1519271.

Special thanks to the program managers Ramesh Kakar and Lucia Tsaoussi for their continued support. COSMIC GPS RO soundings were obtained freely from the University Corporation for Atmospheric Research (<http://cdaac-www.cosmic.ucar.edu/cdaac/products.html>). Thanks to the Precipitation Processing System (PPS) team at NASA Goddard Space Flight Center, Greenbelt, MD, for TRMM data processing assistance. TRMM precipitation feature database is available at <http://atmos.tamucc.edu/trmm/>.

CHAPTER III: RELATIONSHIPS BETWEEN EXTRATROPICAL PRECIPITATION
SYSTEMS AND UPPER TROPOSPHERIC AND LOWER STRATOSPHERIC
TEMPERATURES AND TROPOPAUSE HEIGHT OBSERVED FROM GPM AND GPS
RADIO OCCULTATION

3.1. Introduction

The upper troposphere and lower stratosphere (UTLS) is a coupling region in the atmosphere in which air typically has characteristics of both the troposphere and stratosphere (Gettelman & Birner, 2007; Peevey et al., 2014). It is generally defined as the region ± 5 km around the tropopause (Gettelman et al., 2011), which is the boundary between the troposphere and stratosphere and plays a crucial role in UTLS processes (Holton et al., 1995; Haynes et al., 2001). The UTLS is distinct in radiation, dynamics, chemistry, and microphysics, and a strong connectivity amongst these different processes makes the UTLS highly susceptible to climate change (Birner, 2006). For example, the UTLS has an important influence on troposphere/stratosphere chemical composition and on radiation escaping to space due to relative minimum temperatures and thin cirrus cloud formation at these altitudes, which affects the surface climate and climate feedbacks (Gettelman et al., 2011). A fundamental characteristic of the tropopause is the change in static stability across the interface (Randel et al., 2007). The WMO definition of the tropopause is based on lapse rate criteria (lapse rate tropopause, or LRT) and is defined as “the lowest level at which the lapse rate decreases to 2 K km^{-1} or less, provided that the average lapse rate between this level and all higher levels within 2 km does not exceed 2 K km^{-1} ” (World Meteorological Organization (WMO), 1986). The thermal tropopause provides a convenient way to define the tropopause and is most widely used. There are also other ways of defining the tropopause, such as the potential vorticity-based dynamical tropopause (Hoskins et

al., 1985) or the ozone-based chemical tropopause (Pan et al., 2004). Regardless of tropopause definition, it has been suggested that tropopause height can serve as a useful indicator of climate change (Santer et al., 2003; Birner, 2006).

Stratosphere-troposphere exchange (STE) across the tropopause is an important bidirectional process influencing the chemistry of the UTLS (Holton et al., 1995). Many recent studies have focused on understanding the role convection plays in STE throughout the tropics (e.g., Grosvenor et al., 2007; Fueglistaler et al., 2009; Hassim & Lane, 2010) since radiative-convective balance is the dominant physical process in the region (Held, 1982). Deep convection influences climate processes by regulating stratospheric water vapor through direct convective injection, by enhancing thin cirrus cloud presence, and by modulating the ozone budget in the upper troposphere (Sherwood et al., 2003; Kim & Dessler, 2004; Pan et al., 2004). Additionally, understanding stratospheric hydration/dehydration processes due to deep convection requires accurate measurements of temperature and circulation changes in the UTLS (Randel et al., 2003). Therefore, understanding the role convection plays in the heat budget of the tropical UTLS has been a prominent research topic over the past few decades. Warm anomalies have been observed throughout the mid-to-upper troposphere using radiosonde data (Sherwood et al., 2003) and climate models (Gettelman & Birner, 2007). Cool anomalies have been observed in the tropical tropopause layer (TTL) using AIRS and radiosonde data (Holloway & Neelin, 2007) along with GPS radio occultation data (Paulik & Birner, 2012; Khaykin et al., 2013; Xian & Fu, 2015; Kim et al., 2018; Johnston et al., 2018). The derived amplitude of temperature anomalies varied greatly between these studies, and the magnitude of these anomalies depended on surface type (land/ocean) and intensity of the deep convection.

On the other hand, the relationship of extratropical convection to UTLS temperature and tropopause height changes has attracted much less attention. While this is partly because of the limited availability of detailed diurnal observations of extratropical convection before the GPM era, it is also because of the significant challenge of quantifying the relative contributions of a variety of other dynamical processes associated with extratropical STE (Sprenger et al., 2007). These processes include tropopause folds near the subtropical and polar jets due to baroclinic wave dynamics (Danielsen, 1968; Baray et al., 2000), cutoff lows (Price & Vaughan, 1993), gravity wave breaking (Lamarque et al., 1996), and mesoscale convective complexes (Poulida et al., 1996). For example, significant STE occurs due to turbulent mixing during baroclinic tropopause folds (Reid & Vaughan, 2004), and these folds can even reach nearly as low as the boundary layer (Vaughan et al., 1994). Additionally, simulations have shown that a large fraction of STE near folds occurs due to deep convection below the depressions in the tropopause (Gray, 2003). Note that the global-scale aspects of extratropical STE over longer timescales has been described in previous reviews (e.g., Holton et al., 1995). However, it is critical to study synoptic and mesoscale extratropical storms and their relationship to UTLS temperatures to better understand extratropical STE on shorter timescales.

Space-borne radar observations from TRMM have been useful in identifying the vertical extent of deep convection but were restricted to the tropics and subtropics. Over the extratropics, most passive microwave and infrared satellite data lack the detailed vertical structure of storms and their associated vertical transport. Highly sensitive radar and lidar measurements from CloudSat and CALIPSO have aided the observations of vertical cloud structure in the extratropics.

However, both satellites on the A-train orbit only capture storms at fixed local times of 1:30 P.M. and 1:30 A.M., which misses the peak occurrence of land convection in the extratropics

(Homeyer et al., 2014). Moreover, the small swath of both satellites limits the spatial sampling of individual storms. Now, these gaps can be filled by the GPM mission, which was launched in February 2014. The space-borne radar onboard the GPM satellite, along with high orbit inclination, extends the vertical scan of storms to the high latitudes (Hou et al., 2014). Recent research utilizing GPM has enhanced our understanding of extratropical storms, including identifying the global distribution of storms with large sizes (Liu & Zipser, 2015) and overshooting convection (Liu & Liu, 2016). To better understand storm structure, additional information from nearby atmospheric thermodynamic profiles have historically been obtained from radiosonde soundings with limited spatial and temporal sampling or meteorological analyses/reanalyses with coarse vertical resolution and large uncertainty near the convection. GPS Radio Occultation (RO) soundings have filled these gaps by offering global observations of UTLS temperatures with a high vertical resolution in all-weather conditions (Anthes et al., 2008). The vertical resolution of RO soundings varies from 0.2 km in the lower troposphere to 1.4 km in the upper stratosphere (Anthes et al., 2008) with an average of 0.5 km in the UTLS.

The focus of this research is to better understand extratropical precipitation systems that occur in two different types of synoptic environments and how they impact the UTLS thermodynamic structure. Specifically, the main goals of this paper are to separate these extratropical precipitation systems into two populations, quantify the differences in UTLS temperature and tropopause height anomalies within the two synoptic settings, and determine the physical basis for these anomalies. There are also three secondary goals for this research: 1) to determine where the two populations of precipitation systems occur and what their properties and characteristics are; 2) to quantify how precipitation system intensity and size play a role in determining the sign and magnitude of UTLS temperature anomalies. Previous research has

shown stronger anomalies for the deepest convection, but little attention has been given to the size of the systems. 3) to establish how anomalies vary for land and oceanic systems. Many studies have examined this relationship in the tropics, with differences in anomaly magnitude (even anomaly sign) attributed to land/ocean contrast, but this has yet to be analyzed in-depth for the extratropics. Extratropical precipitation systems are identified using the GPM dual-frequency precipitation radar from 2014 to 2017. The temperature structure within these PFs is provided by the collocated high-resolution GPS RO soundings. The structure of this paper is as follows: Section 3.2 provides background on the GPM, GPS, and ERA-Interim data used in this study; Section 3.3 describes the methodology used, including dataset collocation criteria, how the background profiles and anomalies are generated, and how the PFs are separated into two populations; Section 3.4 provides sampling for PFs in both synoptic settings along with various PF characteristics; Section 3.5 presents the key results of the study, including UTLS temperature and tropopause height anomalies near PFs and the relationship of PF type, depth, size, and season to the magnitude of these anomalies; Lastly, conclusions and study limitations are provided in Section 3.6.

3.2. Data Description

3.2.1 GPM Precipitation Feature Product

The GPM mission is an international network of satellites that provide global observations of rain and snow. Building upon the many successes of TRMM, which focused primarily on quantifying the three-dimensional distribution of moderate-to-heavy rain throughout the tropics (Kummerow et al., 1998), the advanced radar/radiometer system onboard the GPM Core Observatory extends the measurement range to include light precipitation and snow. The

GPM Core Observatory is equipped with the first spaceborne dual-frequency phased array precipitation radar (DPR), which operates at the Ku and Ka bands (13 and 35 GHz, respectively), and a conical-scanning multichannel (10-183 GHz) microwave imager (GMI) (Hou et al., 2014). The 65° orbit inclination allows for observations into the high latitudes where much of the precipitation has a lighter intensity. In this study, GPM radar Precipitation Features (PFs) are obtained from 2014 to 2017. The GPM PF database uses an algorithm similar to the TRMM PF database originally developed at the University of Utah (Liu et al., 2008). The PFs are defined by grouping contiguous areas with nonzero near-surface precipitation using the Ku-band radar (Seto et al., 2013), and the location (lat/lon) of the PF is the centroid of a best-fit ellipse. This analysis method condenses the original pixel-level measurements into the properties of events, which greatly increases the efficiency of searching and sorting the observed historical events (Liu et al., 2008). Maximum echo top heights are used frequently in this study and are obtained using the GPM KuPR, which has a minimum detectable reflectivity near 12 dBZ (Hamada & Takayabu, 2016). For some PFs with large areas, the PF centroid and maximum echo top height location may not be similar (e.g., for elongated fronts with continuous precipitation). PFs with $>2^\circ$ lat/lon difference between the centroid and maximum echo top height are removed from the study.

3.2.2 GPS Radio Occultation Data

GPS RO soundings are obtained from three missions for this study: the joint US-Taiwan six-satellite FORMOSAT-3/COSMIC (FORMOSA Satellite Series No. 3/Constellation Observing System for Meteorology, Ionosphere, and Climate) mission (Anthes et al., 2008), the German TerraSAR-X satellite (Beyerle et al., 2011), and the GRACE-B satellite (Beyerle et al., 2005). The COSMIC constellation provided over 1,000 soundings per day with relatively homogeneous sampling coverage around the globe when GPM was launched in early 2014.

However, the number of daily soundings has decreased to roughly 250-300 per day at the end of 2017. To increase the sampling numbers, additional GPS RO observations from the TerraSAR-X and GRACE-B satellites are obtained. Both satellites provide between 200-250 soundings/day and comprise ~25% of the total collocations with GPM. The reprocessed level-2 RO profiles for all three missions are obtained from CDAAC (COSMIC Data Analysis and Archive Center) at the University Center for Atmospheric Research (UCAR). The profiles are quality controlled by excluding the ones with “bad” flags (such as if the observation bending angles exceed the climatology by a specific threshold). We use the “atmPrf” product, which provides refractivity and dry temperature (T_{dry}) from usually near the surface up to ~60 km. At microwave frequencies, the atmospheric refractivity N is related to atmospheric pressure P , temperature T , and water vapor partial pressure e (Smith & Weintraub, 1953):

$$N = k_1 \frac{P}{T} + k_2 \frac{e}{T^2} \quad (1)$$

where k_1 is 77.6 K hPa and k_2 is $3.73 \times 10^5 \text{ K}^2 \text{ hPa}$. The dry temperature is derived from the refractivity (1) by neglecting atmospheric humidity (Foelsche et al., 2008) such that:

$$T_{dry} = k_1 \left(\frac{P_{dry}}{N} \right) \quad (2)$$

where P_{dry} is the dry pressure (e.g., the pressure without water vapor) derived through hydrostatic integration. In this study, dry temperature is used because it can be treated as an independent satellite retrieval, whereas the real temperature retrieval (“wetPrf”) relies on a priori moisture information from ECMWF low resolution analysis. Note, however, the dry temperature retrieval is nearly identical to the real temperature in the UTLS region, as moisture is negligible when temperatures are generally lower than 250 K (Kursinski et al., 1997). In this study, only sounding altitudes with a T_{dry} less than 250 K were used to minimize the impact of water vapor on the temperature (Johnston et al., 2018). Therefore, the RO dry temperature in the UTLS

region is denoted as RO temperature as it represents real atmospheric temperature. The retrieved profiles are reported as a function of geometric height above mean sea level and the location of each profile nearest to the surface is used.

3.2.3 ERA-Interim Data

ERA-Interim is the global reanalysis produced by the European Center for Medium-Range Weather Forecasting (ECMWF). This gridded dataset covers 1979-present in 6-hour intervals (Dee et al., 2011). Pressure-level temperature and potential vorticity data are used, which have a horizontal resolution of 0.75° latitude x 0.75° longitude with 37 vertical levels from 1000 hPa to 1 hPa. Roughly 6 to 7 levels are provided within the UTLS. Note that COSMIC GPS RO soundings have been operationally assimilated into ERA-I (Poli et al., 2010).

3.3. Methodology

To analyze the relationship between Precipitation Features and the thermodynamic structure of the UTLS, GPS RO temperature profiles are collocated with PFs observed by GPM from 2014 to 2017 throughout the extratropics (20° - 65°). The collocation criteria used for this study are that the GPS profile must be within 3 hours after PF occurrence and within a 300 km radius of the PF, which allows for observation of the PF's impact to its environment. Note that the 300 km collocation criteria is chosen to provide a good balance between robust sampling and observation of the direct impact to the PF's surrounding environment. Each GPS profile is interpolated to a 10 m uniform vertical grid using a quadratic interpolation scheme and then smoothed to 500 m, which is roughly the native resolution for RO profiles in the UTLS altitude range. In addition, for each RO temperature profile, the nearest-neighbor ERA-I potential vorticity profile is also obtained.

To study the relationship between PFs and the UTLS temperature structure, both the PF relative depth (RD) and area are investigated. The RD is a measure of PF depth accounting for the considerable seasonal and meridional variation of the local tropopause height observed throughout the extratropics (Zhang et al., 2014), and the top of the troposphere coincides closely to the level above which convection rarely penetrates. This is because the upper bound on tropospheric clouds is strongly constrained by radiative cooling from water vapor and the depth of tropospheric mixing, and these physical linkages have been applied to both tropical and extratropical convection (Thompson et al., 2017). RD measures the fractional PF depth relative to the local LRT height and is defined as:

$$RD = \frac{\textit{Maximum Height of Detectable Radar Echoes}}{\textit{Lapse Rate Tropopause Height}} \quad (3)$$

Since we are interested in PFs that reach near/into the UTLS, only PFs with a maximum echo top height of at least 50% of the LRT height (e.g., $RD \geq 0.5$) are studied, and the LRT height is identified from a collocated GPS temperature profile.

3.3.1 Zonal Mean UTLS Temperature Variation from GPS Observations

Background temperature structure and tropopause heights are generated using all COSMIC profiles from 2006-2017. The monthly zonal mean global background temperatures, temperature standard deviation, and LRT height are shown in Figure 3.1 using 2.5° latitude bands. Throughout the tropics, LRT heights are consistently high year-round (~15 to 17 km) and UTLS temperature standard deviation remains low. A transition region occurs throughout the midlatitudes around 30° along with a sharp “tropopause break” near the subtropical jet, when the tropical tropopause extends to higher latitudes and overlies the extratropical lower stratospheric air. This transition region migrates with season. In the wintertime, it moves equatorward, becomes sharper and, consequently, the temperature standard deviation increases, whereas in the

summer, it moves poleward and the tropopause height decreases more gradually. In the high latitudes, the tropopause remains low year-round (~8 to 12 km) with a large temperature standard deviation that reaches a maximum during the winter. Note the extremely large standard deviation throughout the polar lower stratosphere, which is due to variability along the edges of the polar vortex. The Arctic vortex reaches its highest variability during the winter (DJF), while the Antarctic vortex displays its largest variability in the spring (SON) since it is stronger, larger, and longer-lasting (Labitzke & Kunze, 2009). The large UTLS standard deviation observed throughout the mid-to-high latitudes is of particular interest in this study, as this clearly indicates considerably different synoptic environments occurring even within individual months. Additionally, several temperature standard deviation “hotspots” are evident that suggest deep convection plays a large role in the observed variation, such as in the lower stratosphere during the Northern Hemisphere summer monsoon (JJA) around ~30°N. Thus, proper characterization of these different synoptic environments is paramount in accurately determining how PFs relate to their environment and impact UTLS temperature variation.

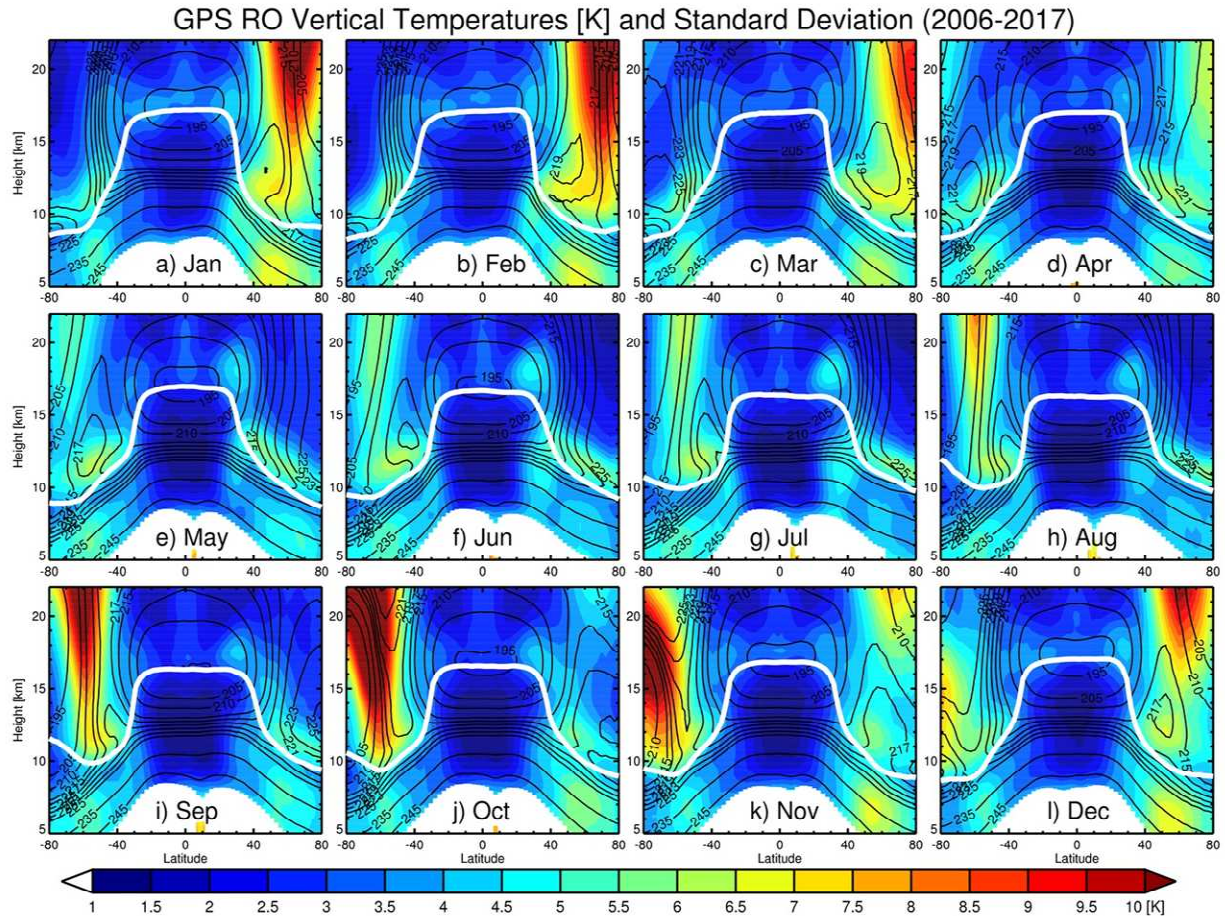


Figure 3.1. Climatology of UTLS zonal mean monthly temperatures (solid contours, in km) and standard deviation (color contours, in km) between 80°N and 80°S derived from COSMIC GPS RO profiles from 2006-2017. Lapse-rate tropopause height is shown with a solid white contour. Temperatures greater than 250 K are removed. Additional temperature contours are added between 205-225 K to better display UTLS structure.

3.3.2 PF and GPS Temperature Profile Classification with Isentropic Potential Vorticity (IPV)

In this study, PFs are separated into two different categories that represent distinct synoptic environments based on extratropical UTLS dynamics. In the extratropics, potential vorticity (PV) is a tracer-like variable based on the conservation of thermodynamic properties and momentum. It is commonly used to identify the boundary between tropospheric and

stratospheric air (i.e. the dynamical tropopause), as the stratosphere is characterized by significantly higher values of PV (Hoskins et al., 1985; McIntyre & Norton, 2000; Kunz et al., 2011). The extratropical tropopause is remarkably close to the ± 2 -PVU surface, where PVU denotes the standard potential vorticity unit ($1 \text{ PVU} = 10^{-6} \text{ m}^2 \text{ s}^{-1} \text{ K kg}^{-1}$) (Holton et al., 1995). Since PV is conserved on isentropic surfaces, isentropic potential vorticity (IPV) has often been used to identify the intrusion of stratospheric air into the troposphere. Namely, the intersection of the 320 K isentrope to the 2-PVU surface has been used to identify moderate to deep stratospheric intrusions or tropopause folds, which frequently occur near extratropical convection during a strong frontal passage from late fall through early spring (Chen, 1995; Appenzeller et al., 1996; Wernli & Sprenger, 2007; Škerlak et al., 2015).

We have adapted this methodology to classify the observed PFs. Background profiles with IPV of at least 2-PVU on the 320 K isentrope are labeled Deep Stratospheric Intrusion (DSI) as they coincide with strong dynamic effects on the tropopause through the aforementioned stratospheric intrusions, whereas profiles with IPV of less than 2-PVU at 320 K are labeled non-Deep Stratospheric Intrusion (non-DSI) as they are more likely to be related to thermodynamic instability. Then, in order to categorize the PFs, they are compared with the monthly-mean GPS background temperature profiles within their respective grid. 12-year non-DSI and DSI median monthly background temperatures/tropopause heights are derived using GPS profiles within 2.5° latitude \times 5° longitude grids. Note that the mean background profile for each synoptic condition is derived only when the number of GPS profiles reaches a minimum of 30 profiles. If the presence of both synoptic conditions exists within one grid (e.g., over the midlatitudes during winter), the simple least-squares method is used to determine the PF's classification by computing the median absolute deviation (MAD) of the PF temperature profile

and the two mean background profiles within ± 5 km around the PF LRT height. Then, whichever background profile has a smaller MAD is the classification assigned to the PF. It is worth noting the challenge in classifying PFs in the extratropics. For example, when using IPV, any potential temperature surface chosen (e.g., 320 K) will intersect the tropopause at different latitudes throughout the year (Wernli & Sprenger, 2007). However, the joint distribution of LRT height/temperature anomalies and IPV values for extratropical PFs clearly shows two distinct PF categories separated by the ± 2 -PVU threshold. An in-depth discussion on this topic can be found in Section 3.5.2 (Figure 3.13).

To show locations in which synoptic overlap occurs, Figure 3.2 displays the sampling for non-DSI (blue contours) and DSI (red contours) background profiles along with mean LRT height differences (e.g., $LRT_{\text{non-DSI}} - LRT_{\text{DSI}}$) for regions that experience overlap. The number of GPS profiles in each grid generally ranges from 60 to 120 in areas with one synoptic condition but can be significantly reduced in areas where both synoptic conditions occur (such as the midlatitudes). The transition region shifts equatorward as winter approaches and moves poleward in the summer. The corresponding LRT height differences between the mean non-DSI and DSI backgrounds also shows large seasonal variation, especially in the Northern Hemisphere due to larger land/ocean contrast. The largest differences are typically observed over the oceans. In January (Figure 3.2a), height differences of 2.5 to 3.5 km are seen over the Kuroshio and Gulf Stream warm ocean currents. This can be attributed to consistent changes in air mass type and large baroclinicity along the coasts. On the other hand, the smallest variability occurs over the continental interior as conditions are frequently cold and dry. The transition region shifts much farther north in July (Figure 3.2c), with few DSI profiles and small LRT height differences seen. In general, the transition region coincides well with the latitude band showing the largest UTLS

temperature variation (between 40°-60° from Figure 3.1), which further confirms the importance of separating the two distinct synoptic conditions using IPV for an extratropical UTLS study. In addition to the large tropopause height standard deviation resulting from different synoptic conditions, there can be large intraseasonal LRT height variations throughout the subtropics, especially during the winter to early spring months where standard deviations often exceed 2 km. For example, Seidel & Randel (2007) have shown a bimodal distribution of subtropical tropopause heights, with one mode above 15 km (characteristic of the tropical tropopause) and another one below 13 km (typical of the extratropical tropopause). Pan et al. (2009) has also shown the occurrence of multiple tropopauses extending to nearly 60° N. Therefore, in order to minimize the impact intraseasonal LRT height variation could have on monthly mean GPS background temperature profiles (and anomaly calculations), PFs that occur within any grids with monthly LRT height standard deviations exceeding 2 km are removed from this study.

GPS RO Sampling and LRT Height Differences for NonDSI and DSI Background Profiles

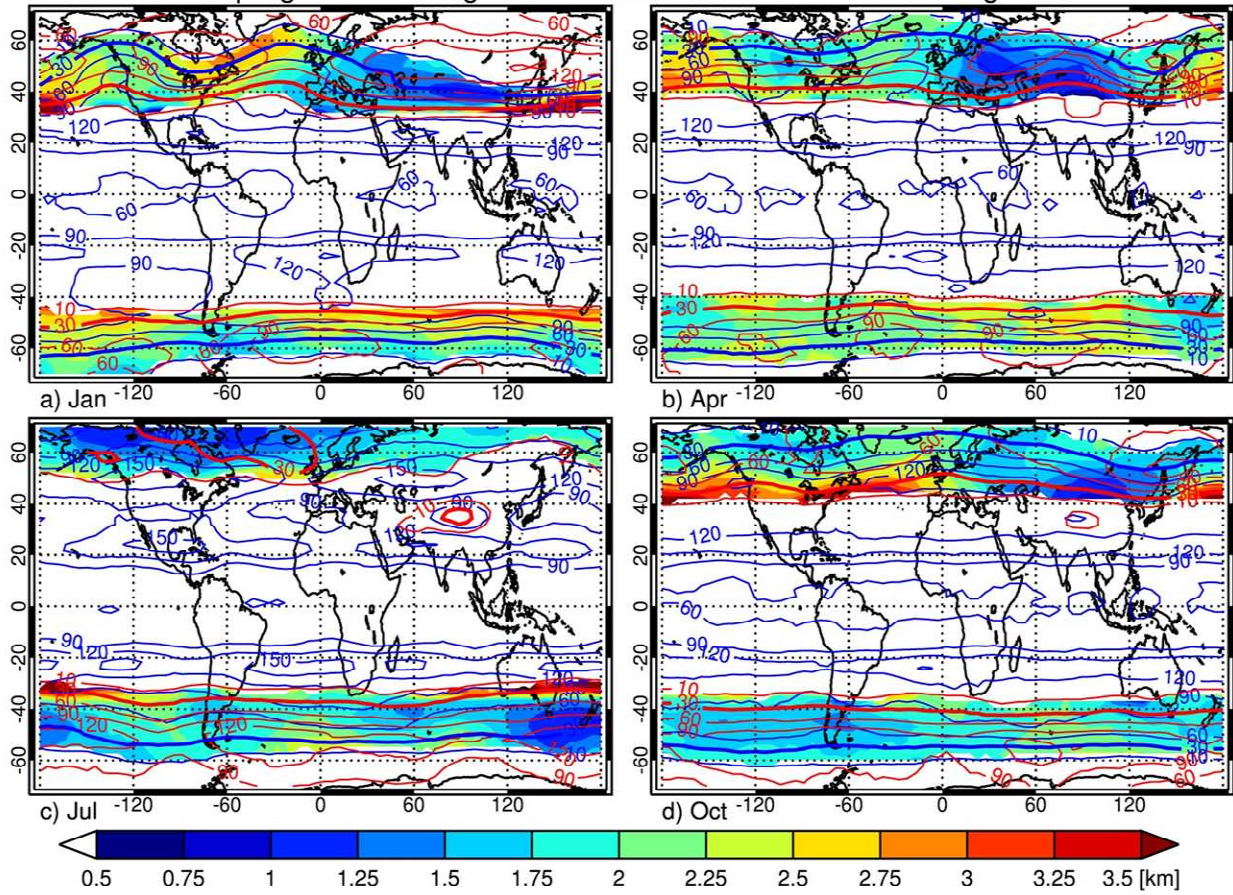


Figure 3.2. GPS RO sampling for non-DSI (solid blue contours) and DSI (solid red contours) background profiles from 2006-2017 for a) January, b) April, c) July, and d) October. Shaded contours display LRT height differences (km) between non-DSI and DSI background profiles, provided the sampling is at least 10 profiles.

3.3.3 UTLS Temperature Anomaly and Tropopause Height/Temperature Anomaly Calculations

In this study, each individual PF temperature anomaly profile (T') is derived by subtracting the PF temperature profile (T_{PF}) from the gridded-mean GPS background temperature (T_{BG}) profile:

$$T'(z) = T_{PF}(z) - T_{BG}(z), \quad (4)$$

Where height z is from within $\pm 5\text{km}$ of the PF's LRT height to account for the large seasonal and meridional variations in tropopause height. Figure 3.3 shows GPS temperature profiles collocated with PFs (red) and their gridded-mean non-DSI and DSI background profiles (black). Figure 3.3a shows a relatively large-size ($20,229 \text{ km}^2$) overshooting PF with a relative depth of 1.07 that is classified as non-DSI. The temperature anomaly profile (Figure 3.3b) is calculated simply by subtracting the background profile with the smaller mean absolute deviation (solid black line) from the individual PF profile. The temperature anomalies for each PF are centered on each individual PF's LRT height (horizontal red dashed line) and obtained for a $\pm 5 \text{ km}$ window (blue-shaded box) around this height. Then, the anomalies are grouped according to the different PF characteristics and averaged to generate a mean anomaly profile for each group, with the "zero" height being the location of each PF LRT. The number of samples within each subgroup is recorded, and PFs over land and ocean are also separately investigated. The PF temperature/synoptic profile comparison from Figure 3.3a is relatively straightforward; however, there are some instances (e.g., Figure 3.3c) that can be somewhat ambiguous. While the upper tropospheric section of the PF profile is certainly "non-DSI" in nature, the tropopause/lower stratosphere is rather uncertain. Thus, the temperature anomaly profile from Figure 3.3d looks quite different than Figure 3.3b. However, we do not want to hide these examples; rather, it is important to show that the environments are not always clean-cut. The relationship between PFs and LRT height/temperature is also analyzed by subtracting the median background from the PF tropopause height/temperature:

$$LRTH' = LRTH_{PF} - LRTH_{BG} \quad (5)$$

$$LRTT' = LRTT_{PF} - LRTT_{BG} \quad (6)$$

The PFs are again categorized by their area and RD to determine the relationship between PF intensity and anomaly magnitude.

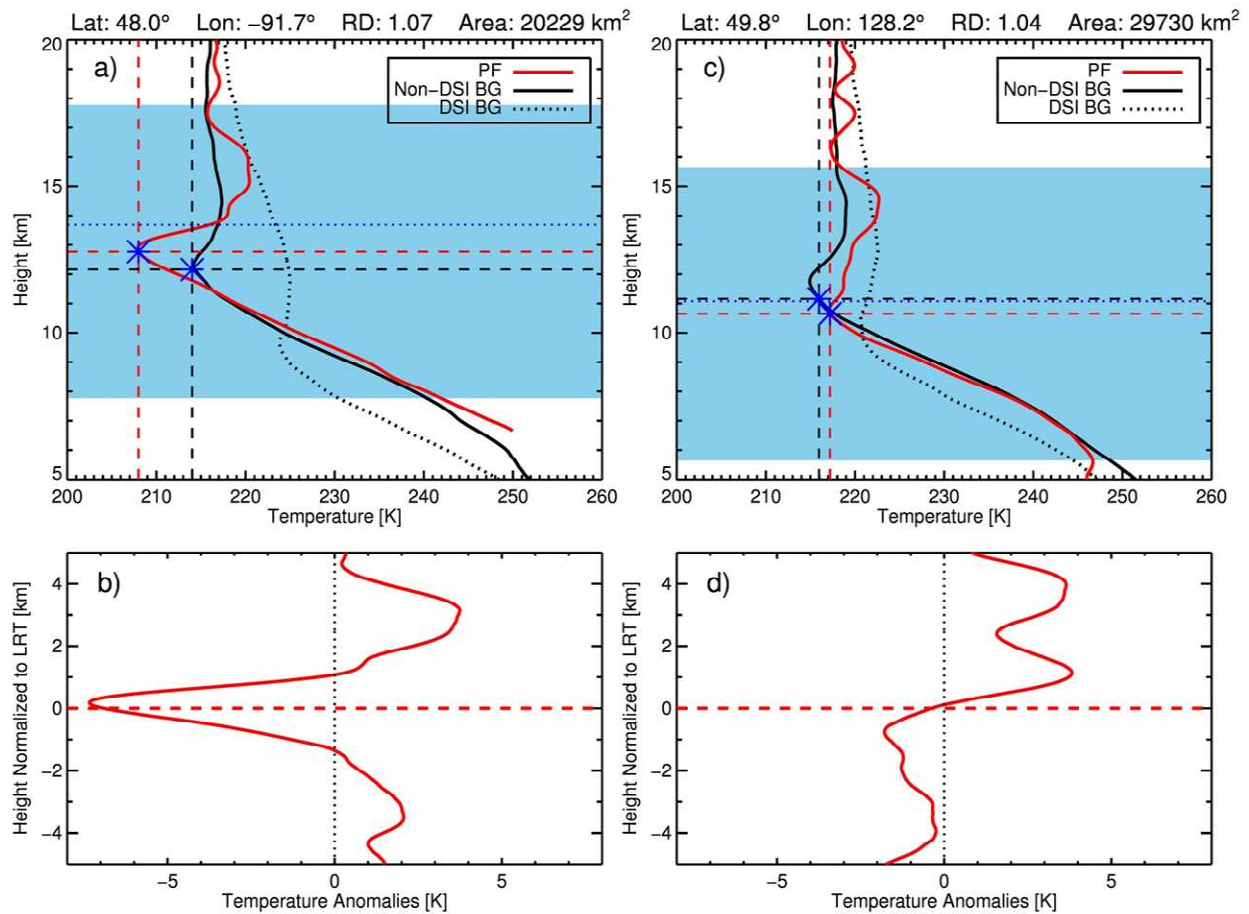


Figure 3.3. Two overshooting non-DSI PFs (a,c) with collocated GPS temperature profiles (solid red) along with their associated non-DSI (solid black) and DSI (dotted black) background profiles. Blue asterisks and the associated dashed lines indicate the height and temperature of the background and PF LRT. Dotted blue line indicates the PF maximum echo top height. Blue-shaded area shows the region ± 5 km around the PF’s LRT height for anomaly calculation. Temperature anomaly profile is shown on the bottom (b,d) with the “zero” height corresponding to the PF’s LRT height.

Figure 3.4 shows an example of an overshooting convective system observed by GPM in the early morning of July 28, 2015 over South Dakota in the United States. This system is a strong bow-echo, with near-surface reflectivity reaching up to 60 dBZ (Figure 3.4a) and maximum echo top heights over 17 km (Figure 3.4b). Additionally, a cross-section through the feature is also displayed, with very low brightness temperatures and high rain rates (50 mm/hr) occurring near the core of the storm (Figure 3.4e). The collocated ERA-I potential vorticity is near or slightly above 1 PVU, indicating a likely non-DSI system (Figure 3.4c). Finally, the collocated temperature profile near the maximum echo top height at 43.8° N and 100.7° W is shown along with its corresponding background profile, and the LRT height and maximum echo top height are also displayed (Figure 3.4d). The RD of this feature is 1.13, indicating overshooting convection.

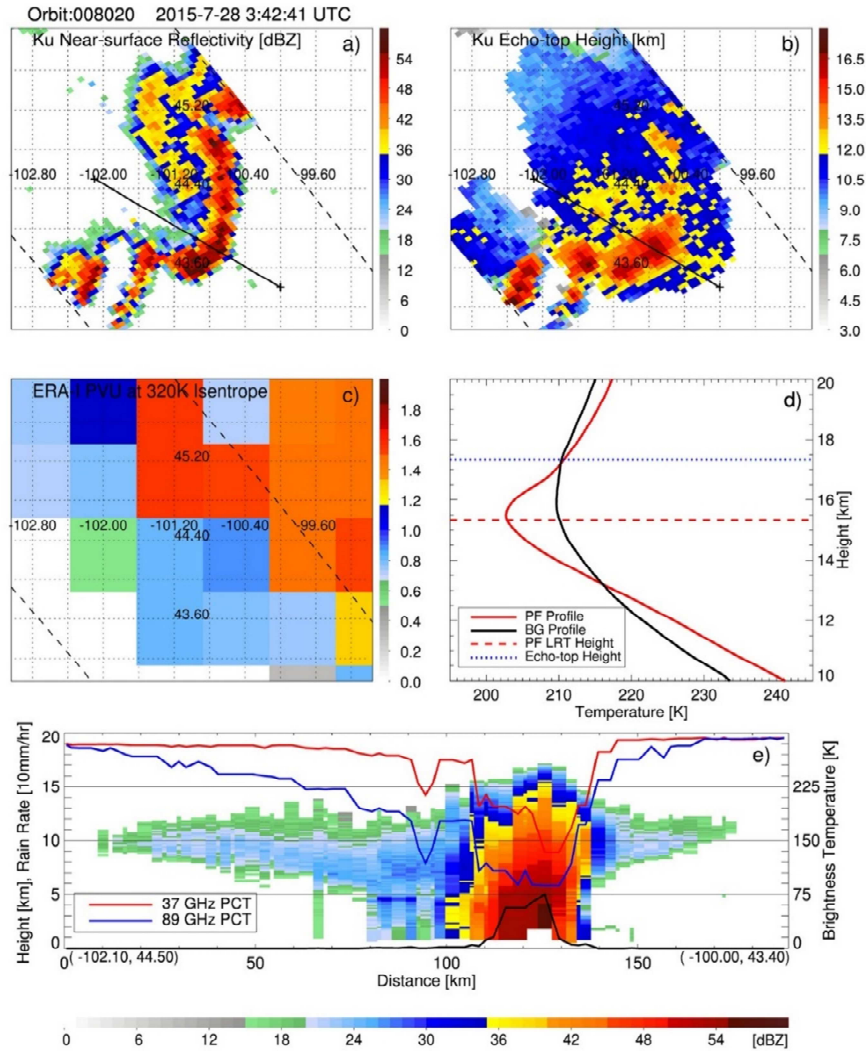


Figure 3.4. Overshooting convection observed by GPM over South Dakota in the morning of July 28, 2015. a) PR Ku-band near-surface reflectivity (dBZ). b) PR Ku-band maximum echo top heights (km). c) ERA-Interim potential vorticity at 320 K potential temperature over the GPM PR swath. d) Collocated temperature profile (red) near the maximum echo top height (43.8° N, 100.7° W) and the corresponding background profile (black), along with the PF lapse rate tropopause height (red) and maximum echo top height (blue). e) Cross-section of PR Ku-band reflectivity (dBZ) through the center of the storm. Red line is the GMI 37 GHz polarization-corrected temperature (K); blue line is the GMI 89 GHz polarization-corrected temperature (K); and black line is the rain rate (10 mm/hr).

3.4. Study Regions, Sampling, and Storm Characteristics

The extratropics in both the northern and southern hemispheres (20° - 65°) are chosen for analysis in this paper. There are 832,858 PFs with a $RD > 0.5$ throughout the extratropics and 23,594 of these PFs have collocations with a GPS RO temperature profile. Of these collocations, 12,662 are non-DSI PFs and 10,932 are DSI PFs; after removal of PFs that occurred in background grids with large tropopause height variation, these numbers are reduced to 10,178 and 9,573, respectively. Figure 3.5 displays the distribution of collocated PFs observed by GPM with a $RD > 0.5$ from 2014 to 2017 for both non-DSI PFs (a,b) and DSI PFs (c,d) categorized by size and RD. Larger-size Non-DSI PFs (Figure 3.5a) are most frequently observed over the oceanic regions. These larger systems are likely midlatitude cyclones that have progressed from mature and into the occlusion stage of development. In contrast, the deepest (overshooting) PFs (Figure 3.5b) are mainly found over land masses, such as North America, Europe, and Argentina. These deepest PFs are primarily summertime convection fueled by warm land surface temperatures and strong instability. However, some deep PFs also form over warm ocean currents such as the Gulf Stream, some of which are likely tropical cyclones. On the other hand, DSI PFs (Figure 3.5c and d) are most often observed in the mid-and-high latitudes, with few occurrences in the subtropics. Most DSI PFs occur over the oceans due to contrasting air masses, with the cold and dry continental air masses interacting with the warmer and wetter oceanic air masses. Several hotspots stand out, such as the wintertime storm tracks over the Southern Ocean, the Icelandic Low, and the Aleutian Low. No consistent pattern is shown for different PF size or RD categories. However, as expected, many more DSI PFs have large sizes rather than depths since these systems will typically have much weaker uplift than summertime convection.

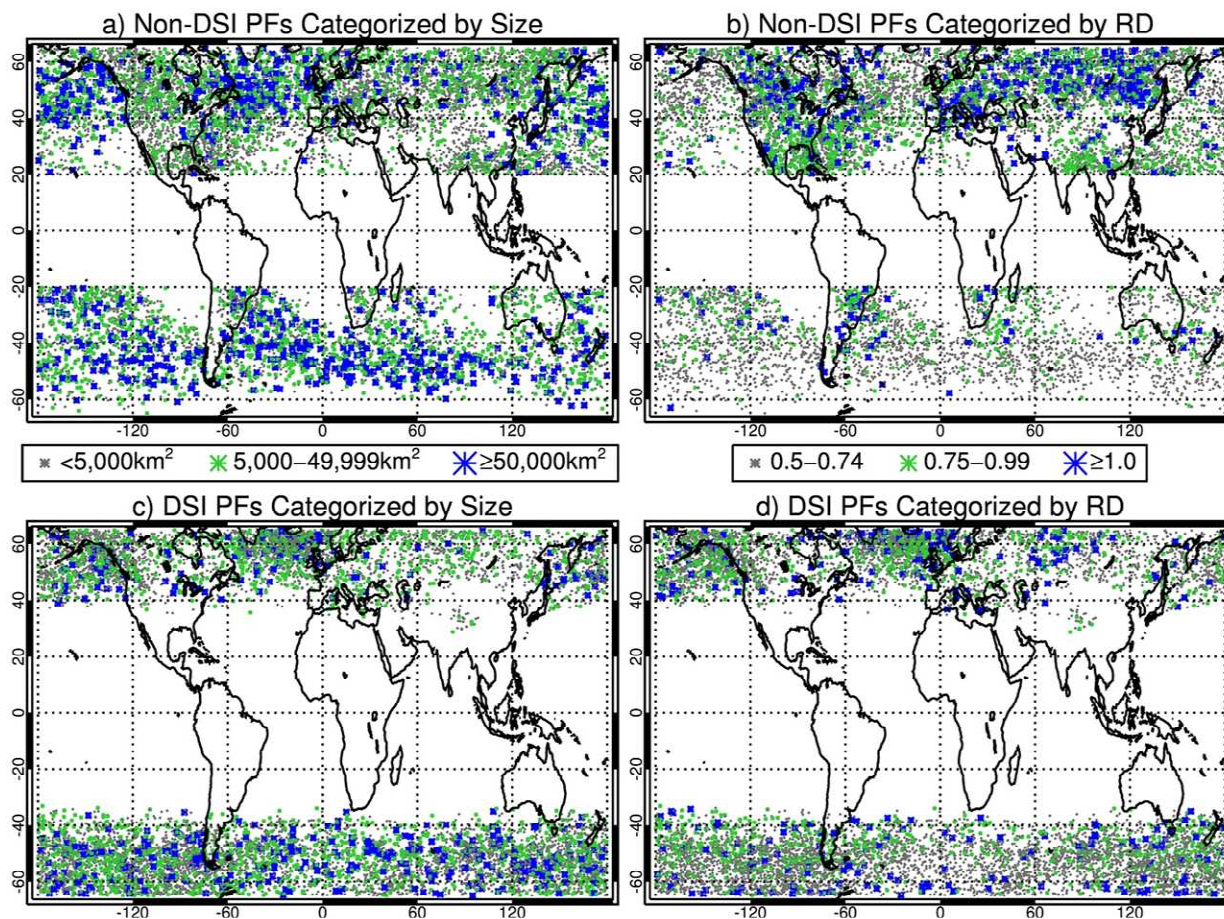


Figure 3.5. Distribution of extratropical PFs (RD > 0.5) observed by GPM from 2014 to 2017 for a) non-DSI PFs categorized by size, b) non-DSI PFs categorized by RD, c) DSI PFs categorized by size, and d) DSI PFs categorized by RD.

Figure 3.6 displays histograms of a subset of PFs with collocated GPS profiles for various PF characteristics over the mid and high latitudes from 2014 to 2017. Due to the generally uniform distribution of GPS RO observations, the subset of collocated PFs maintains the characteristics of PFs observed by GPM. The peak occurrence of non-DSI PFs displays a higher maximum echo top height (Figure 3.6a and d) of around 6-7 km relative to the peak occurrence of DSI PFs, which occurs around 4.5-5 km. Additionally, even though land non-DSI

PFs only make up a small portion of the total sampling, they comprise the majority of PFs with echo tops greater than 10 km, which DSI PFs rarely reach. Note that most PFs have a size less than 10,000 km² (Figure 3.6b and e). The number of PFs typically decreases as the area increases, especially for land PFs, which rarely reach 100,000 km². Interestingly, there are comparatively fewer oceanic non-DSI PFs for the smallest areas relative to the other categories, whereas they display the highest number of PFs for the largest areas. The PFs also display a distinct seasonality within the midlatitudes (Figure 3.6c), as non-DSI PFs show a considerable peak in each hemisphere's summer months, while DSI PFs display a strong peak in the winter months. This seasonality is even more pronounced for non-DSI PFs in the high latitudes (Figure 3.6f), with an extreme peak in the summer months and few during the rest of the year. However, DSI PFs are substantially different, with a peak in boreal spring in the Northern Hemisphere and a peak in early austral fall in the Southern Hemisphere. Nevertheless, DSI PFs are relatively common year-round within the high latitudes in both hemispheres.

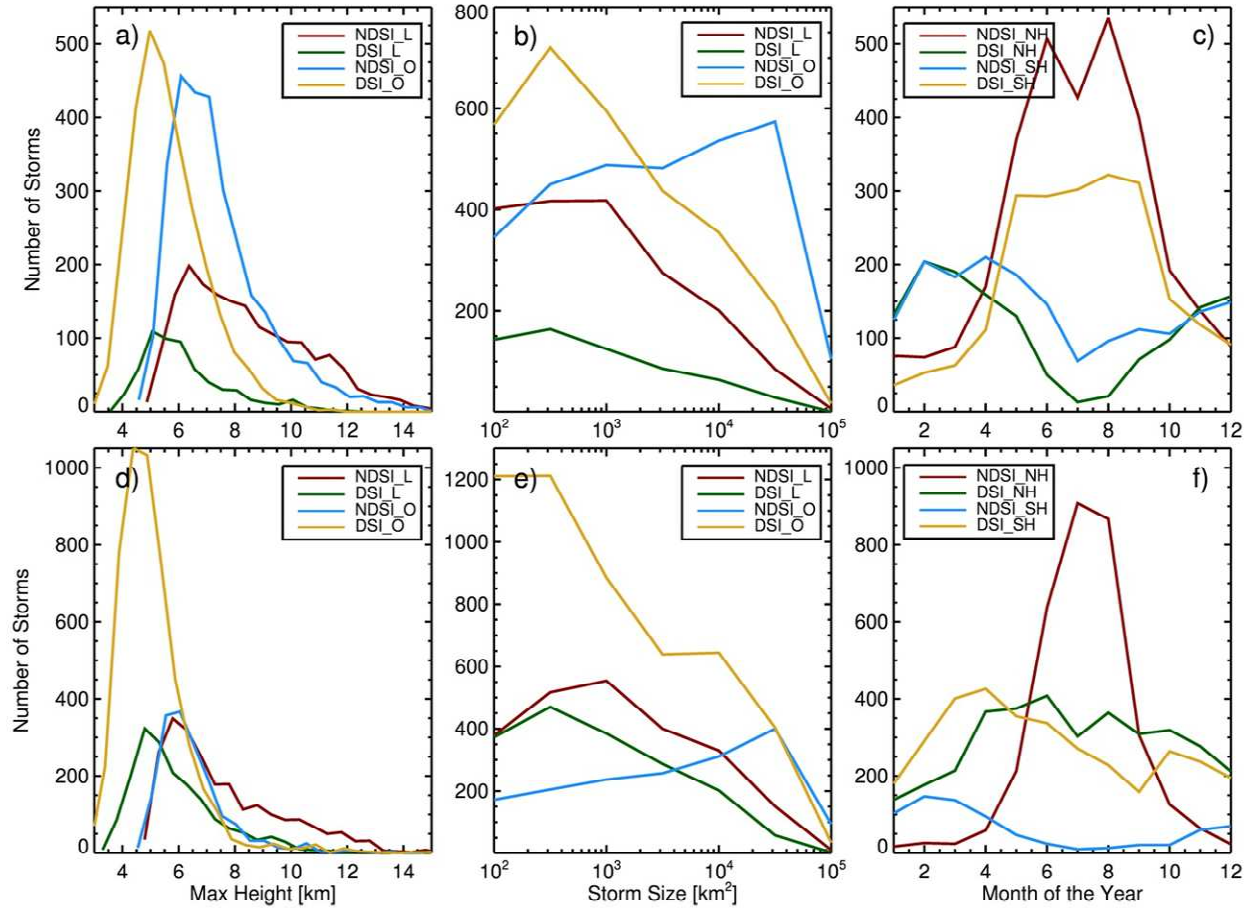


Figure 3.6. Histograms for non-DSI (NDSI) and DSI PFs with GPS collocations over land (L, in red/cyan) and ocean (O, in green/yellow) within 35°-50° (top) and 50°-65° (bottom) from 2014 to 2017 for various PF characteristics, including (a,d) maximum echo top heights (km), (b,e) area (km²), and (c,f) month of the year. NH and SH represent Northern Hemisphere and Southern Hemisphere, respectively.

3.5. Results

3.5.1 Relationship of PF Characteristics to UTLS Temperature Anomalies

This section focuses on extratropical PF characteristics and UTLS temperature anomalies within ± 5 km of the PF LRT height. One of the primary goals of this section is to determine how

surface type as well as PF size and depth influences the magnitude of UTLS temperature anomalies. GPS RO temperature anomalies near both non-DSI and DSI PFs are separated by their surface properties (land or ocean) and further divided into subgroups based on PF size (area) and depth (RD) (Figures 3.7 and 3.9). For example, PFs reaching close to the LRT are grouped together within the “0.8-1.0” RD classification, while PFs reaching above the LRT (overshooting) are grouped within the “>1.0” classification. Finally, PFs are grouped by their month of occurrence (Figures 3.8 and 3.10) to determine any seasonal differences in anomalies.

3.5.1.1 Non-DSI PFs

Figure 3.7 displays the mean GPS RO temperature anomalies near non-DSI PFs over the extratropics (20° - 65°). For all PFs classified by various RDs (Figure 3.7a), warm anomalies are observed for PFs within roughly 1.5 to 5 km below the LRT, ranging from 0.1 K to 0.8 K. Interestingly, the strongest warming (~ 0.8 K) occurs for the shallower PFs ($RD < 0.6$) whereas weak warming occurs for deeper PFs reaching near or above the tropopause ($RD > 1$). We speculate that this is because the more intense deep convection typically occurs in the earlier part of a storm’s life cycle (Machado et al., 1998). As a result, the cumulative influence of latent heat release that occurs around the core of the storm may not be sufficient to affect the surrounding environment yet (Houze, 1989; Schumacher et al., 2004). Above the upper tropospheric warming, a strong layer of cool anomalies centered on the PF LRT is observed, ranging from roughly -2.5 to -3 K. Both the shallowest and deepest PFs show comparable magnitudes of strong cooling. Above the cooling layer, warming of 0.5 to 1 K is generally observed with the largest magnitudes for the deepest overshooting PFs, although nearly zero anomalies are observed for the shallowest PFs. There are major differences in anomaly magnitude between land and oceanic PFs (Figure 3.7b and c), with much more variation evident for oceanic PFs. For

example, oceanic PFs display a wide range of anomalies below the tropopause layer, with moderate warming for the shallower RDs and strong cooling for the deeper RDs. However, warming is observed for all land PF RD categories. Additionally, the largest anomaly magnitudes occur near oceanic PFs, as the strongest tropopause-level cooling, as well as warming below and above the tropopause, is observed in these groups.

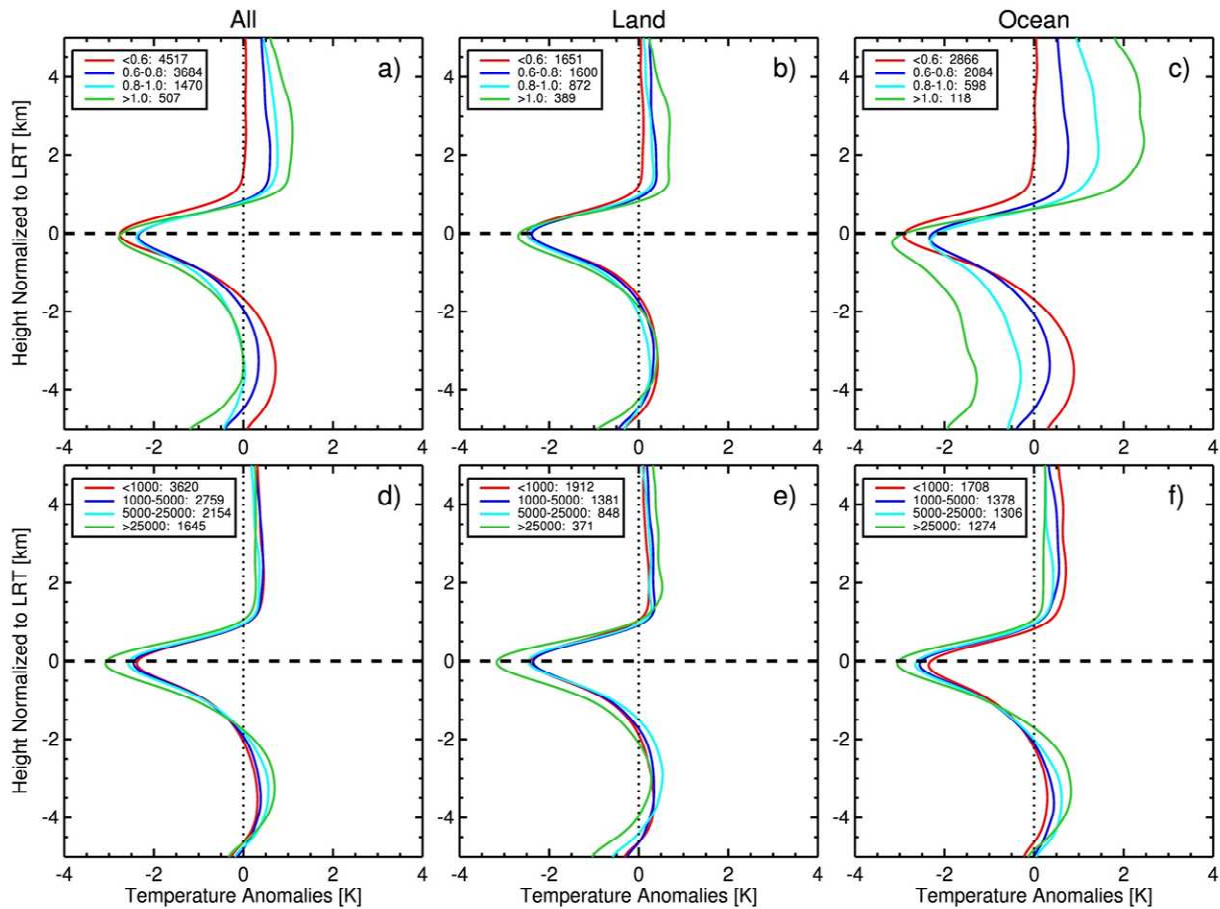


Figure 3.7. GPS RO temperature anomalies (K) near non-DSI PFs classified by relative depth (top) and area (bottom, in km²) for (a,d) all PFs, (b,e) land PFs, and (c,f) oceanic PFs. The number of PFs within each category is also displayed after each label.

Similar temperature anomaly patterns are seen for all PFs with different sizes (Figure 3.7d). A clear increase in anomaly magnitude from smaller to larger PF size is observed throughout the vertical extent of the profiles. A warming layer is displayed up to 1.5 km below the LRT for all subgroups, with the largest PFs exhibiting the strongest warming (up to 0.8 K). The strongest cooling at the LRT also occurs for the largest PFs (roughly -3 K). Above the cooling layer, a much smaller range of anomalies is displayed, with minor warming (~0.3 K) observed for all PFs. Differences between land and ocean PF size subgroups are relatively minor (Figure 3.7e and f), highlighted by slightly stronger warming below the LRT and cooling at the LRT for oceanic PFs. Larger anomaly variation is again observed among different size oceanic PFs, but with much smaller variation compared to the RD dependency.

The UTLS temperature anomaly patterns observed in this study for extratropical non-DSI PFs are similar to anomaly patterns displayed in previous research near tropical deep convection (e.g., Johnston et al., 2018). The warm temperature anomalies observed throughout the mid-to-upper troposphere result from latent heat release in-and-near the convective clouds (Randel et al., 2003; Gettelman & Birner, 2007). The cool anomalies near the convective tropopause have been characterized in a few different ways. Holloway & Neelin (2007) showed that as gravity waves spread convective warming through the free troposphere, hydrostatic pressure gradients will extend above the heating, causing divergence, ascent, and adiabatic cooling aloft. The convective “cold-top” should be thought of as an inherent part of quasi-equilibrium temperature adjustment. Khaykin et al. (2013) also discussed two cooling mechanisms: the first being nonmigrating tides generated by convective diabatic heating; and the second being the systematic injection and turbulent mixing of adiabatically cooled air by cross-tropopause updrafts. Previous studies have shown both warming and cooling in the layer above the tropopause, which is confirmed in this

study. For example, Chae et al. (2011) observed warm anomalies at these altitudes and downward motions above the convection. They suggested that strongly divergent flow and turbulent mixing near the cloud tops would mechanically drag the air just above the cloud outward, which would pull comparatively warmer lower stratospheric air down from above the clouds.

Figure 3.8 displays the monthly mean temperature anomalies for non-DSI PFs within the extratropics in both hemispheres. The extratropics are separated into two bands to determine any latitudinal differences (20° - 40° and 40° - 65°). Throughout each hemispheric latitude band, large differences in the pattern and magnitude of anomalies are observed as the seasons change. Within 20° - 40° N (Figure 3.8a), the magnitude of upper tropospheric warming remains similar in each month, although the sharpness of the transition from warm to cool anomalies does differ. However, tropopause-level cooling is weakest from late spring through early fall and strongest during the wintertime. The magnitude of summertime tropopause-level cooling (between 1.5-2 K) is similar to results shown in previous research throughout the tropics (e.g., Johnston et al., 2018). Considerable seasonal variation is displayed for the lower stratospheric warming. Similar results are also observed within 20° - 40° S (Figure 3.8c). For example, the weakest tropopause-level cooling is again observed during the summer whereas the strongest occurs during the winter. In contrast, seasonal magnitude changes generally show the opposite patterns in the high latitudes for both hemispheres. Within 40° - 65° N and S (Figure 3.8b and d), the strongest tropopause-level cooling is seen during the summer whereas the weakest occurs during the winter. Upper tropospheric warming is slightly stronger in the high latitudes, with the strongest warming occurring during austral summer and boreal winter. Again, considerable variation is observed in the lower stratosphere. We attribute the seasonal magnitude changes in the two

latitude bands to seasonal variations in PF characteristics (not shown). Within 20°-40° N, the wintertime tends to have more frequent shallower but larger size PFs relative to the summertime, when more frequent deep convective cores with smaller sizes are observed. However, within 40°-65° N, the shallower convection that occurs during the summer have larger areas than the wintertime PFs of similar depth. The Southern Hemisphere PFs also display similar characteristics albeit to a smaller degree as the majority of PFs occur over the ocean. This confirms the results from Figure 3.7 where PFs with larger sizes produced the strongest tropopause-level cooling.

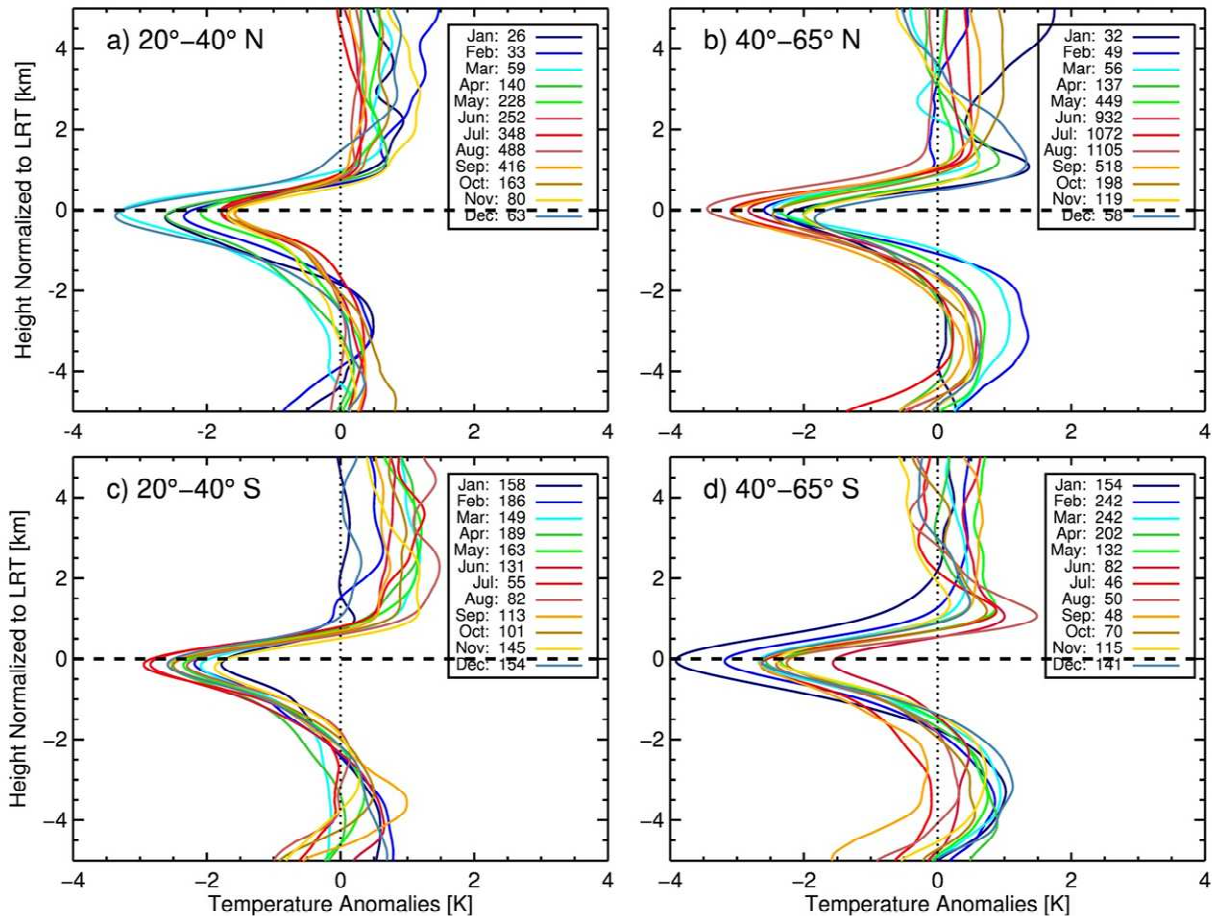


Figure 3.8. Monthly mean GPS RO temperature anomaly profiles (K) near non-DSI PFs over a) 20°-40°N, b) 40°-65°N, c) 20°-40°S, and d) 40°-65°S. The number of PFs within each category is also displayed after each label.

3.5.1.2 DSI PFs

Figure 3.9 displays the mean GPS RO temperature anomalies near DSI PFs within the extratropics (20°-65°), with clear differences in the anomaly vertical structure observed compared to non-DSI PFs. There is a well-defined pattern of increasing temperature anomaly magnitude for deeper RDs, as the strongest cooling in the upper troposphere more than doubles in magnitude for overshooting PFs compared to the shallowest PFs. For all PFs classified by

various RDs (Figure 3.9a), robust cooling is observed from 5 km below the LRT to roughly 0.5-1 km above the LRT, with the magnitude of cooling increasing with altitude and RD. Maximum cooling occurs just below the LRT, ranging from -2 K for the shallowest RD to over -5 K for the deepest RD. Above the LRT, temperature anomalies rapidly transition to strong warming. Maximum warming increases with stronger RD (from 2 to 4 K) and occurs at progressively higher altitudes. Major temperature anomaly differences are evident between land and ocean PFs (Figure 3.9b and c). Throughout the extratropics, DSI PFs occur more frequently over the oceans, with around four times as many PFs observed relative to over land due to the increase in baroclinicity over the oceans. This stronger baroclinicity is reflected in anomaly magnitudes that are much larger near the oceanic PFs. This is especially true for deeper PFs reaching near or above the LRT (e.g., $RD > 0.8$), where the maximum cool/warm anomalies can be 2-4 K stronger than PFs with a shallower RD. On the other hand, the weaker baroclinicity for land DSI PFs means less of a disparity between the mixing air masses, which results in smaller temperature anomalies and anomaly profiles that look more similar to non-DSI PFs. The temperature anomaly structure is similar for DSI PFs categorized by size (Figure 3.9d), with cooling in the upper troposphere and warming in the lower stratosphere both ranging from 1.5 to 3 K. Interestingly, larger tropopause-level anomalies are observed for PFs with smaller sizes. This is in direct contrast to non-DSI PFs, which display a distinct increase in anomaly magnitude as area increases. Differences in anomaly structure between land and oceanic PFs (Figure 3.9e and f) are less pronounced. In general, oceanic PFs still display larger anomaly variation between different sizes, but only on the order of 1-2 K compared to 2-4 K for different RDs.

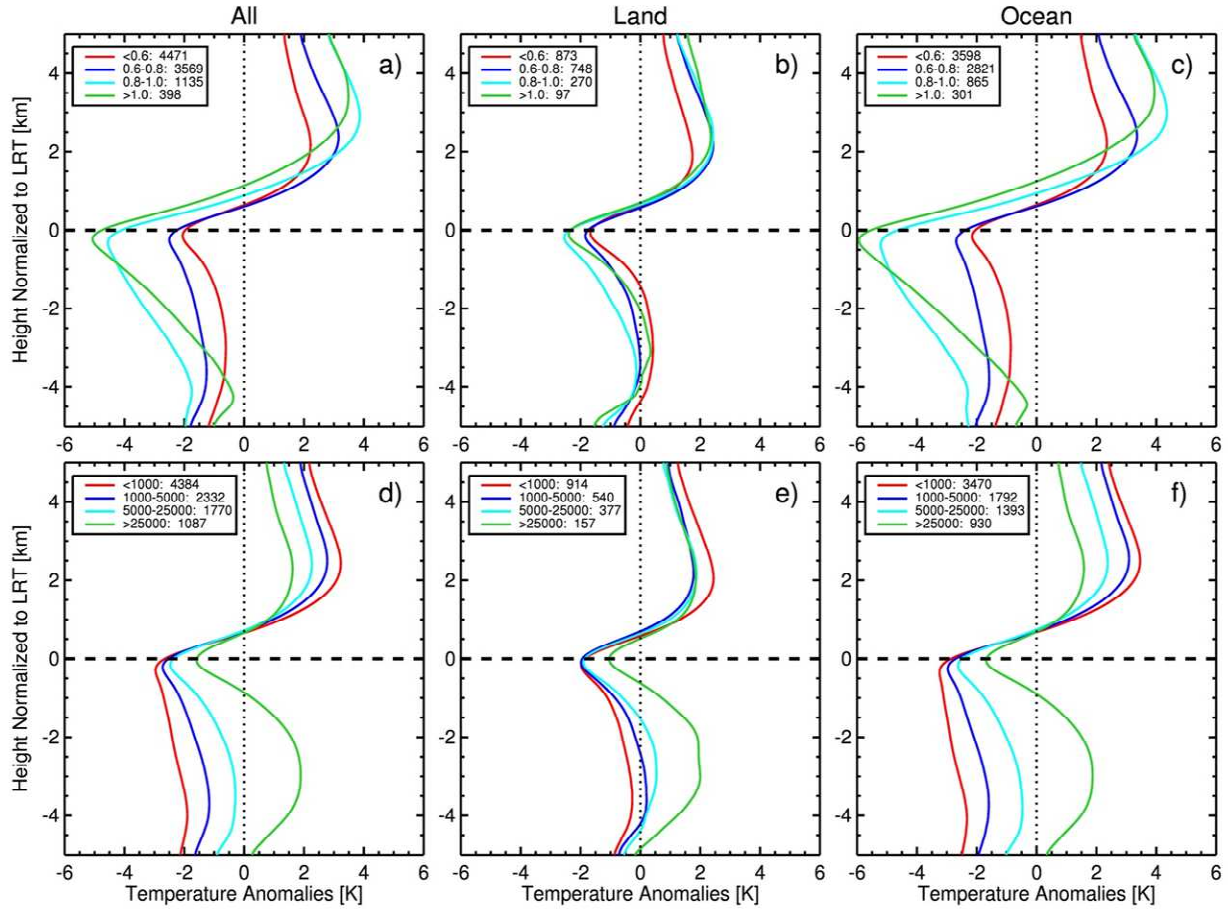


Figure 3.9. GPS RO temperature anomalies (K) near DSI PFs classified by relative depth (top) and area (bottom, in km^2) for (a,d) all PFs, (b,e) land PFs, and (c,f) oceanic PFs. The number of PFs within each category is also displayed after each label.

It is worth noting the UTLS temperature anomalies (and tropopause anomalies shown later) observed near the DSI PFs are strongly influenced by extratropical dynamics rather than the just PFs themselves (unlike non-DSI PFs). Extratropical cyclones obtain their energy from sharp horizontal temperature and moisture differences between tropical and polar air (e.g., highly baroclinic environments). We speculate that the differences in the magnitude of temperature anomaly variation as DSI PF area and RD increase may be related to the maturing and

dissipation process in these extratropical cyclones. During the early stages of extratropical cyclone development, surface frontogenesis is accompanied by strong differential temperature advection of cold and warm air. At this stage, the PFs are often driven by large thermodynamic instability, with a stronger intensity, reaching higher altitudes, and having relatively smaller sizes. As the cyclone matures, the system becomes occluded, thereby growing in size but weakening in strength. This ensures continued dynamic mixing among the two contrasting air masses, which is displayed as weaker cooling in the upper troposphere. After the cyclone has mixed away the temperature contrasts across the front, there is no longer any potential energy available to keep the cyclone going so it dissipates. On the other hand, the larger, more mature systems have ample time to spread latent heat release to the surrounding upper tropospheric environment (evidenced in the strong warming displayed only near the largest PFs). However, these speculations need further validation through observations and model simulations in the future. Additionally, tropopause folding associated with deep frontogenetic forcing can occur commonly near and upstream of PFs in baroclinic environments (Uccellini, 1986). A tropopause fold is an extrusion of stratospheric air within an upper-tropospheric baroclinic zone that slopes downward from the normal tropopause level to the middle or lower troposphere (Reed, 1955). The fold is associated with a substantial lowering of tropopause heights and has been identified to be a contributor to upper-level frontogenesis and the rapid development of surface storms (Bosart and Lin, 1984; Uccellini, 1986). In summary, the DSI PFs themselves are not the only cause of the temperature anomalies observed relative to the nearby dynamical processes. However, the observed temperature changes can provide insight into the depth and size of the PFs that most commonly occur in a highly baroclinic environment.

Additionally, note that there may be a PF-type ambiguity within larger DSI PFs. For example, many large-size DSI PFs form along elongated cold fronts in the wintertime with a large meridional and small zonal extent. If the pixels identified by the GPM KuPR are contiguous along the length of the front, then the front would be considered a single PF. However, there may be some deeper convective features near the equatorward-end of the PF which may be some distance away from the stratospheric intrusion. While steps are taken to minimize this limitation (such as filtering out PFs with a distance greater than 2° between the PF center and the location of PF maximum height, see Section 3.2.1), some stronger convective features with more non-DSI characteristics may remain within large DSI PFs.

Figure 3.10 displays the monthly mean temperature anomalies for DSI PFs within 40° - 65° in both hemispheres. For DSI PFs, even larger seasonal differences are observed in the pattern and magnitude of anomalies as the seasons change. In the Northern Hemisphere, wintertime PFs display cool anomalies throughout the entirety of the upper troposphere, with maximum cooling of -4 K occurring near the tropopause. Additionally, lower stratospheric warming is also at a maximum in the winter (~ 3 K). In contrast, summertime PFs display weak warming in the upper troposphere (~ 0.5 K) along with relatively weaker cooling (less than -2 K) near the tropopause and warming (~ 1 K) in the lower stratosphere. Anomaly magnitudes during the transition seasons generally remain in between summer and winter magnitudes. Similar results are also shown for the Southern Hemisphere PFs. Cool anomalies are observed throughout the entirety of the upper troposphere in all seasons but with stronger summertime cooling near the tropopause (-2 to -3 K). The larger-amplitude wintertime anomalies are likely due to stronger temperature contrasts fueling the development of intense midlatitude cyclones, which cause deeper tropopause folding and significant stratosphere-troposphere exchange. These

contrasts weaken significantly in the summer, leading to reduced dynamic UTLS mixing which results in anomaly profiles that look more similar to non-DSI PFs.

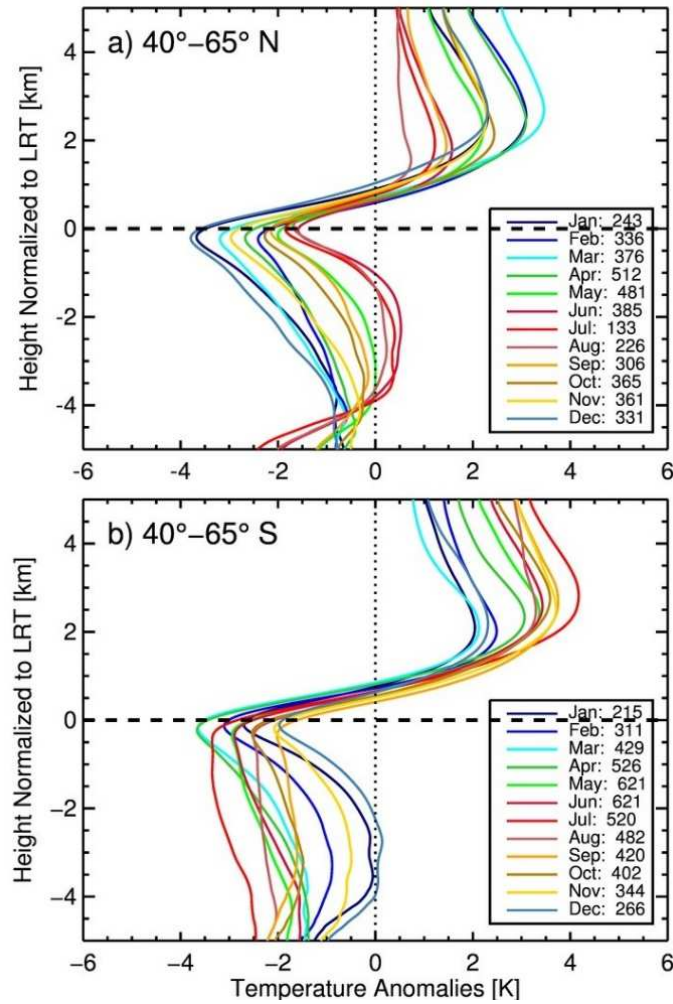


Figure 3.10. Monthly mean GPS RO temperature anomaly profiles (K) near DSI PFs over a) 40°-65°N and b) 40°-65°S. The number of PFs within each category is also displayed after each label.

3.5.2 PF Relationship to Tropopause Height/Temperature Anomalies

The previous section (3.5.1) focuses on the relationship between PFs and the broad UTLS temperature structure throughout the extratropical region, where temperature anomaly profiles

are generated by normalizing the anomalies to each individual PF's LRT height. Here we focus on the changes that occur specifically to the thermal tropopause near PFs. LRT height and temperature anomalies are generated by comparing the background tropopause with the tropopause that is observed after a PF has occurred. Two-dimensional histograms are constructed relating the RD and size of the PF to the magnitude of tropopause height and temperature anomalies observed. The PFs are binned using intervals of 0.1 for RD, and bin sizes increase logarithmically from 100 km² to ~120,000 km² for area. Contours of the number of PFs within each bin are also plotted (each bin must have at least 10 profiles).

Figure 3.11 displays the LRT height and temperature anomalies for non-DSI and DSI PFs within the extratropics (20°-65°). Moderate LRT height decreases are observed (0.1 to 0.4 km), on average, for relatively small-size PFs and for PFs with a high RD and moderate size. In contrast, considerable LRT height increases (0.2 to 0.6 km) are observed for PFs with a low RD, with larger height increases for large-size storms. The corresponding temperature anomalies (Figure 3.11c) show a similar pattern but with the opposite sign compared to the height anomalies. For example, warm LRT temperature anomalies (0.1 to 1.0 K) are observed for smaller PFs along with moderate-sized PFs with high RD, whereas cool LRT temperature anomalies (0.1 to 2 K) occur for PFs with a low RD and ones with a high RD and large size. On the other hand, DSI PFs are consistently associated with negative LRT height anomalies (Figure 3.11b) along with a corresponding large LRT temperature increase (Figure 3.11d). Much larger anomaly magnitudes are observed relative to non-DSI PFs. This is directly related to the sinking of stratospheric air near strong extratropical cyclones, which are mainly driven by baroclinic instability. We speculate that the properties of these PFs are related to the formation and development of these extratropical cyclones. Anomaly magnitude is larger for PFs with a

stronger RD, which likely occur in the earlier stages of cyclone development. The largest LRT height anomalies (-1.5 to -2.0 km) and temperature anomalies (6 to 8 K) are observed for storms with the highest RD, whereas the smallest LRT height anomalies (-0.25 to -0.5 km) and temperature anomalies (0.1 to 2 K) are seen for large-size PFs with a shallow RD, when cyclones are likely in the occlusion stage.

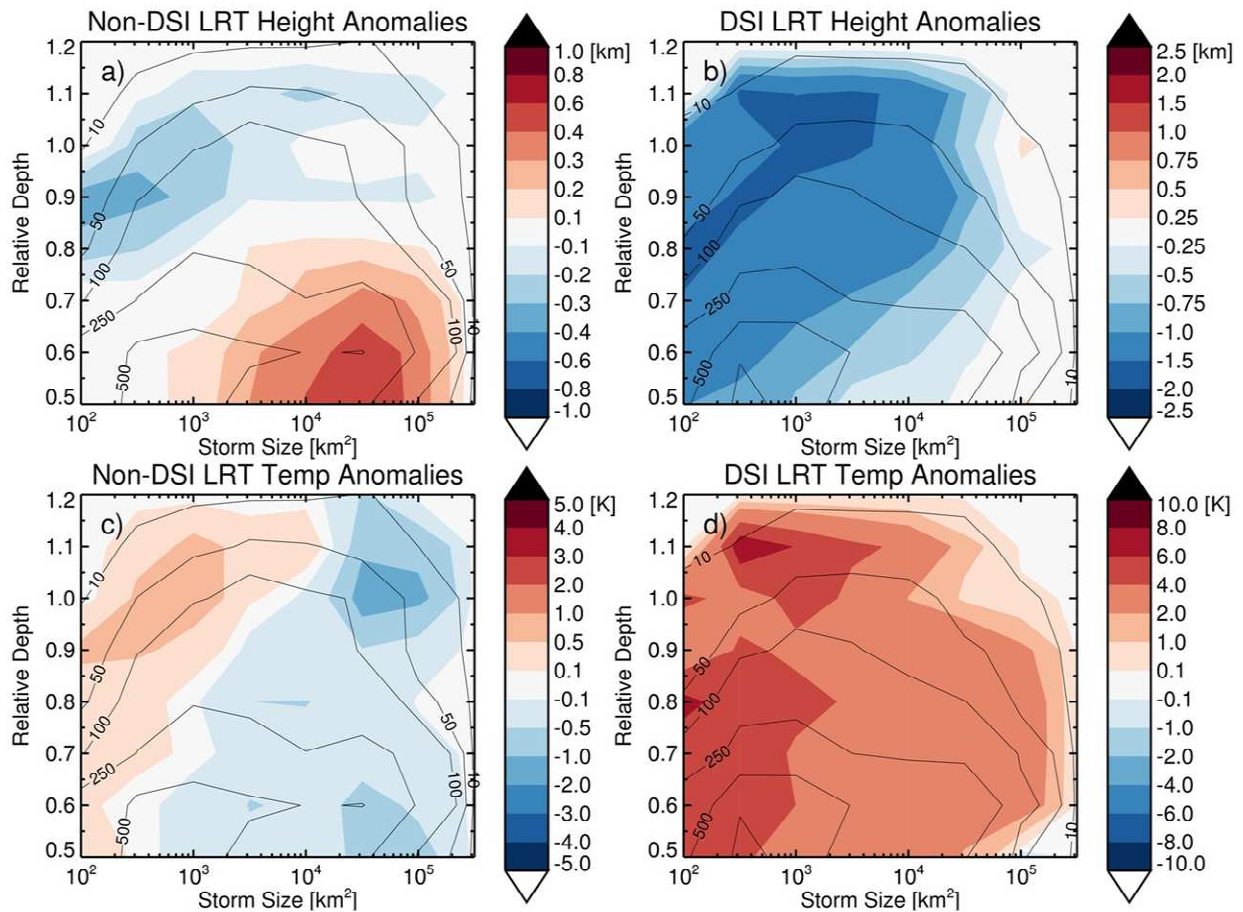


Figure 3.11. Two-dimensional histogram (contour) and joint-distribution of lapse rate tropopause height and temperature anomalies (shaded) with corresponding PF size and relative depth for non-DSI (a,c) and DSI (b,d) PFs.

Figure 3.12 displays the observed LRT temperature/height anomalies (solid contours) along with the temperature anomalies at the PF LRT relative to the background profile at the same altitude (the anomalies at the “zero line” from Figures 3.7 and 3.9; shaded contours), as well as individual cases representing typical RO profiles near each type of PF. Non-DSI PFs throughout the extratropics (Figure 3.12a) display a wide range of tropopause anomalies, with LRT temperature anomalies up to ± 12 K and height anomalies up to ± 2.5 km. However, most of these samples are clustered near the middle with only a slight trend toward the lower-right quadrant. Most PFs are typically found in the upper-left and lower-right quadrants, which indicates that the tropopause is most commonly raised/cooled or lowered/warmed (with only a small fraction of samples showing the LRT can be lowered/cooled or raised/warmed). Even though the PF tropopause displays considerable variation relative to the background tropopause, strong cooling (shaded contours) is almost always observed for the PF LRT *relative to the background temperature at the same altitude* (which was displayed in Figure 3.7). The strongest cooling (between -8 to -10 K) occurs when the PF LRT is pushed much higher (e.g., 2 km), but notable cooling is also observed (between -2 to -6 K) even when the PF LRT is at a lower altitude than normal. This can be explained by a commonly observed type of profile seen in the lower-right quadrant and is shown in Figure 3.12c, where a PF-located GPS profile (red) is compared to its background profile (black). In this instance, the PF LRT is almost 1 km lower and 3 K warmer than the background LRT. However, note that the PF LRT is roughly 2 K colder than the background temperature at this altitude. Near the top of the PF (blue dotted line), the lapse rate increases compared to the background and a relative minimum temperature is observed above the convective cloud. Above the cloud top, an inversion commonly occurs, and then the temperature progresses towards another relative minimum at a slightly higher altitude. This often

results in a double tropopause structure, as a new, lower LRT forms near the cloud top and the second (higher) LRT remains either near or is pushed up a few kilometers above the climatological LRT, similar to previous results shown by Biondi et al. (2012). While this type of profile was infrequently observed throughout the entire extratropics, it was most commonly seen in the subtropics. Additionally, this type of profile was observed for PFs with a weaker RD as well as a stronger RD (this example shown is 0.893). Additional research into the formation of these “lower” tropopauses near the convective top is recommended, especially for determining how long this type of UTLS environment persists after PF occurrence. Similar to non-DSI PFs, DSI PFs throughout the extratropics (Figure 3.12b) display a wide range of tropopause anomalies. The amplitude of maximum anomalies nearly doubles for DSI PFs, with LRT temperature anomalies up to 20 K and LRT height anomalies near -4 km. Most samples are within the lower-right quadrant, indicating the PF LRT typically becomes much lower and warmer due to baroclinic dynamics (such as tropopause folding and potential vorticity streamers). Nevertheless, similar to non-DSI PFs, strong cooling is again observed at the PF LRT relative to the background temperature at the same altitude. However, the strongest cooling now occurs when the PF LRT height *decreases* the most. A typical GPS temperature profile for a high-RD DSI PF is displayed in Figure 3.12d. The PF-located temperatures are much colder than the background environment throughout the troposphere. The cold UTLS air descends deeply into the troposphere along a tropopause fold, which is associated with typical baroclinic features such as strong cold fronts and extratropical cyclones (Reid and Vaughan, 2004). The PF LRT shows a much sharper temperature transition, with a height about 2 km lower (at ~7.5 km) and temperature ~3 K warmer than normal. The tropopause inversion layer, which is a region of enhanced static stability above the extratropical tropopause associated with a narrow-scale

temperature inversion (Randel and Wu, 2010), occurs between ~ 7.5 km to 10.5 km and becomes somewhat stronger. Temperatures remain above normal throughout the lower stratosphere near the PF as a result of the intrusion of comparatively warmer air pulled down from the stratospheric overworld (Holton et al., 1995). This type of profile is the most common profile observed near DSI PFs, although there are some instances when the PF LRT can be pushed higher and become colder.

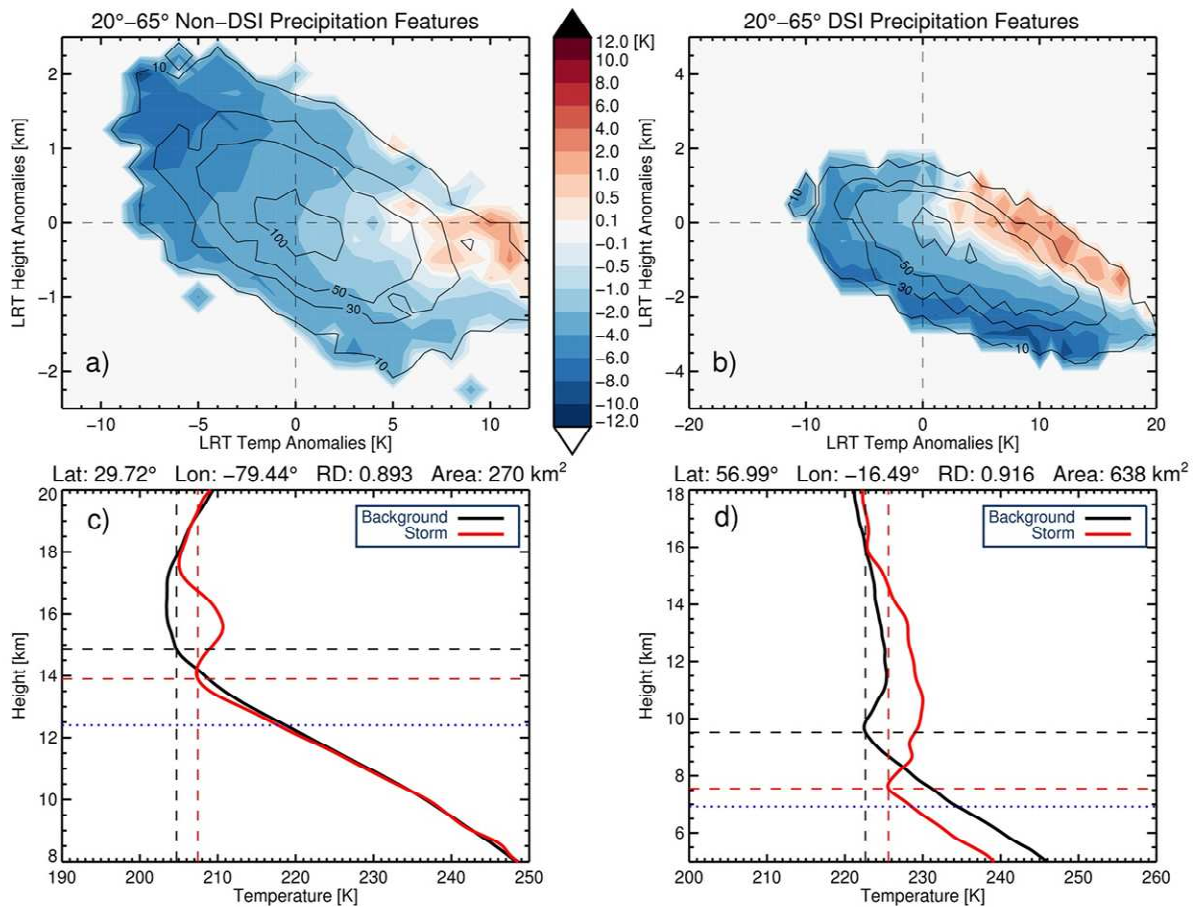


Figure 3.12. Two-dimensional histogram of the PF LRT temperature (K) and height (km) anomalies (solid contours) and the joint-distribution of the temperature anomalies (K) at the PF LRT from Figures 3.7 and 3.9 (shaded contours) for (a) non-DSI and (b) DSI PFs. Also shown are examples of common PF-collocated GPS temperature profiles (red) for (c) non-DSI (2015-07-05) and (d) DSI (2016-05-02) PFs along with their associated background profiles (black).

Dashed lines indicate the tropopause height and temperature for both profiles and dotted lines indicates maximum echo top height.

It is also interesting to observe the distribution of PFs as a function of their potential vorticity values at the 320 K isentrope and their LRT height/temperature anomalies derived from the collocated GPS profiles (Figure 3.13). Note that positive PVU values indicate PFs within the northern hemisphere and negative PVU values indicate PFs within the southern hemisphere. Non-DSI PFs have the majority of samples clustered to minor/moderate effects on the LRT, although height anomalies can reach ± 5 km and the corresponding temperature anomalies can reach ± 20 K. However, there is a distinct change in the LRT height and temperature anomalies observed around ± 2 -PVU. The overwhelming majority of DSI PFs display much lower LRT heights than normal along with, in general, a corresponding LRT temperature increase (although note that Northern Hemisphere temperature anomalies show more variability). Additionally, the anomaly magnitudes tend to become larger as PVU values also become larger. These clear differences in tropopause anomalies further confirm that using isentropic potential vorticity (specifically at 320 K) is a useful technique for separating extratropical precipitation features.

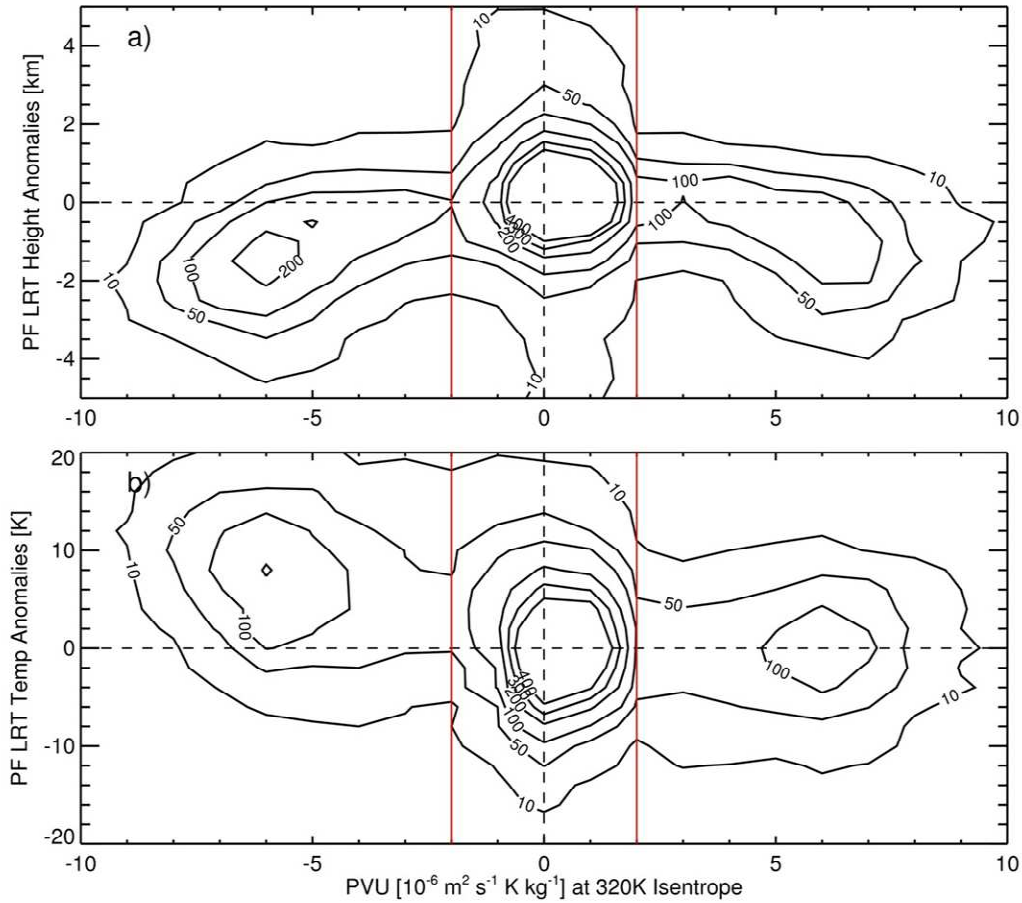


Figure 3.13. Sampling contours for PFs collocated with GPS temperature profiles comparing the potential vorticity values (PVU) at the 320 K isentrope with the lapse rate tropopause height (a, km) and temperature (b, K) anomalies that occurred near the PF. Solid red lines separate non-DSI and DSI PFs.

3.6. Conclusions

In this paper, the relationship between extratropical convection and the thermodynamic structure of the UTLS was studied by collocating precipitation features observed by the GPM dual-frequency precipitation radar with high vertical resolution GPS RO temperature soundings from 2014 to 2017. PFs were classified into two different synoptic conditions using potential

vorticity. UTLS temperature and tropopause height/temperature anomalies were calculated throughout the extratropics in both hemispheres (20°-65°). Anomalies were then studied for different PF sizes, depths, and surface types as well as classified by month of occurrence.

For non-DSI PFs (Figure 3.7), warm temperature anomalies ranging from 0.1 K to 1 K were observed from roughly 5 km to 1.5 km below the LRT due to latent heat release in-and-near the convective clouds. This transitioned to a layer of strong cooling ranging from -2 K to -3 K centered around the PF LRT height which occurs due to the injection of adiabatically-cooled air near the tops of the PFs. Beginning about 1 km above the PF LRT, minor-to-moderate warming ranging from 0.2 K to 1 K was observed. On the other hand, DSI PFs (Figure 3.9) displayed distinctly different results. Strong cooling ranging from -2 K to -5 K was generally observed (except for large-size PFs) throughout the mid/upper troposphere, with maximum values occurring slightly below the PF LRT. The anomalies transitioned to moderate/strong warming above the LRT, ranging from 2 K to 4 K. This temperature anomaly pattern occurs due to strong horizontal dynamic mixing among contrasting tropical and polar air masses and is associated with tropopause folding and a lowering of the tropopause. These DSI PFs likely contribute considerably to the large temperature standard deviation observed throughout the upper troposphere within the mid/high latitudes (Figure 3.1).

The relationships between PF depth/size and land/ocean contrast to anomaly magnitudes were also analyzed. For non-DSI PFs (Figure 3.7), the tropopause-relative depth (RD) displayed mixed results on anomaly magnitude. The strongest warming in the upper troposphere and cooling near the PF LRT generally occurred for PFs with the shallowest RD. In contrast, a consistent progression in anomaly magnitude was observed for upper tropospheric warming as well as cooling around the PF LRT as PF size increased. We speculate this may be related to the

life cycle of a PF, as intense overshooting convection typically occurs in the earlier stages of convective development and enough time may not have passed to spread the warming and cooling to the environment surrounding the PF. Under a different synoptic environment, DSI PFs (Figure 3.9) show the opposite results, as the strongest upper tropospheric cooling and lower stratospheric warming occurred near the deepest PFs, whereas the largest size PFs displayed the weakest magnitudes. We speculate that this is related to responses of temperature in the UTLS and properties of PFs under the different stages of extratropical cyclone development. The overall vertical structure of UTLS temperature anomalies was similar for land and oceanic PFs, but some key differences were evident. Anomaly magnitudes were generally stronger near oceanic PFs, especially for DSI PFs. This was expected, as baroclinicity is typically strongest near the coasts, especially over warm ocean currents in the wintertime. Additionally, much more variation in the temperature anomalies was evident for oceanic PFs of various sizes and RD.

In addition, seasonal differences in anomalies for each synoptic environment were also explored. For non-DSI PFs between 20°-40° N/S in both hemispheres (Figure 3.8), tropopause-level cooling was weakest from late spring through early fall and strongest during the wintertime. However, within the higher latitudes (40°-65° N/S), seasonal magnitude changes showed the opposite patterns, as the strongest tropopause-level cooling was seen during the summer whereas the weakest occurred during the winter. This is attributed to latitudinal seasonal variations of PF characteristics. For DSI PFs within 40°-65° N and S (Figure 3.10), wintertime PFs displayed cool anomalies throughout the entirety of the upper troposphere and the strongest near-tropopause cooling of any season. Additionally, lower stratospheric warming was also at a maximum in the winter. In contrast, summertime PFs displayed minor warming in the upper troposphere and weaker near-tropopause cooling. The larger-amplitude wintertime anomalies

likely occurred due to stronger temperature contrasts fueling the development of intense midlatitude cyclones, which cause deeper tropopause folding and likely more stratosphere-troposphere exchange.

Finally, the relationship between extratropical PFs and LRT height/temperature was quantified relative to PF area and RD. For non-DSI PFs, minor decreases in LRT height (-0.1 to -0.4 km) and increases in LRT temperature (0.1 to 1.0 K) were generally observed, on average, for PFs with a deeper RD and small-to-moderate size (Figure 3.11a and c), whereas PFs with a shallower RD and large area displayed large height increases (0.2 to 1 km) and temperature decreases (-0.1 to -2 K). Overall though, non-DSI PFs throughout the extratropics display a wide range of tropopause anomalies, with LRT temperature anomalies up to ± 12 K and height anomalies up to ± 2.5 km (Figure 3.12a). Two types of UTLS temperature profiles were commonly observed for non-DSI PFs: 1) the PFs either push the tropopause higher and it becomes colder (Figure 3.3a); or 2) a double tropopause structure develops, with a new, lower tropopause forming near the top of the convective cloud beneath the higher climatological LRT (Figure 3.12c). DSI PFs were associated with much larger tropopause anomalies (Figure 3.11b and d). On average, LRT heights are 0.25 km to 2 km lower and LRT temperatures are 2 to 8 K warmer than normal during significant deep stratospheric intrusion events, indicative of general subsidence and tropopause folding. Additionally, height decreases of almost -4 km and temperature increases near 20 K were observed (Figure 3.12b). There is one common profile type observed near DSI PFs, as the LRT displays a much stronger than normal temperature transition and a robust tropopause inversion layer is seen (Figure 3.12d).

It is worth noting that there are some limitations in this study. First, GPM only provides a snapshot of the PF at the time of observation so it cannot capture the stage of storm development

(although it can be inferred to some extent). This additional information would be useful for providing a more in-depth explanation of the differences in the temperature anomaly magnitudes under different PF size and depth. Second, UTLS temperature and tropopause anomalies would ideally be determined relative to the larger neighboring environment of each PF. Unfortunately, this is not possible with current GPS RO sounding density, so a composite study in this paper is unable to describe the full influence of convection on its environment. Third, the amount of GPS RO soundings available in the extratropics has steadily declined in recent years, as satellite missions such as COSMIC have reached the end of their life cycle. The recently launched COSMIC-2A mission will only provide soundings within the tropics and subtropics, so additional GPS RO satellites are needed to provide necessary coverage throughout the extratropics. Finally, note that both TerraSAR-X and GRACE are on a sun-synchronous orbit, which could lead to less uniform local-time sampling compared to COSMIC. However, despite these limitations, these results suggest intricate relationships between different types of precipitation systems and the UTLS temperature structure and tropopause throughout the extratropics, as the sign and magnitudes of anomalies observed vary considerably under the different synoptic environments and for the various PF characteristics. It is hopeful that this study will enhance our understanding of extratropical convection, stratosphere-troposphere exchange processes, and lead to the continued improvement of PF representation in weather and climate models. Additional studies on the role that PFs play in moisture transport in the extratropical UTLS would also be beneficial in understanding extratropical STE and will likely be a topic of future research.

Acknowledgements

Funding for this research was provided by NASA grants (NNX14AK17G and NNX15AQ17G). Chuntao Liu was supported by NASA-NNX16AD76G and NSF-1519271. Special thanks to the program managers Dr. Ramesh Kakar and Dr. Lucia Tsaoussi for the support of the project. GPS RO soundings were obtained freely from the University Corporation for Atmospheric Research (<http://cdaac-www.cosmic.ucar.edu/cdaac/products.html>). Thanks to the Precipitation Processing System (PPS) team at NASA Goddard Space Flight Center, Greenbelt, MD, for GPM data processing assistance. GPM precipitation feature database is available at <http://atmos.tamucc.edu/trmm/>.

CHAPTER IV: CHARACTERISTICS OF THE EXTRATROPICAL TROPOPAUSE: BIMODALITY AND ITS RELATIONSHIP TO THE OCCURRENCE OF DOUBLE TROPOPAUSES

4.1. Introduction

The tropopause is one of the most important locations of the atmosphere as it separates the turbulently-mixed troposphere and the more stable stratosphere (Anel et al., 2008) and these two layers of the atmosphere are chemically, dynamically, and thermally distinct (Holton et al., 1995). A fundamental characteristic of the tropopause is the change in static stability across the interface (Randel et al., 2007). The World Meteorological Organization definition of the tropopause is based on thermal criteria using the temperature lapse rate (lapse rate tropopause, or LRT), which provides a convenient way to define the tropopause (World Meteorological Organization (WMO), 1986). The tropopause can also be defined by more general stability criteria using the potential vorticity-based dynamical tropopause (Hoskins et al., 1985) or the ozone-based chemical tropopause (Pan et al., 2004). Characteristics of the tropopause and the surrounding region, the upper troposphere and lower stratosphere (UTLS), are important because the tropopause acts as a “two-way gate” for the exchange of mass, water vapor, and chemical species between the troposphere and stratosphere (Fueglistaler et al., 2009). Specifically, stratosphere-troposphere exchange (STE) of ozone and water vapor has attracted substantial interest, because these two trace gases make significant contributions to atmospheric radiative forcing and their distributions and controlling mechanisms are important elements of chemistry-climate interaction (Pan et al., 2009). The long-term variability and trends of the tropopause height have been recognized as a climate change indicator (Birner, 2006; Homeyer et al., 2010) because of its location in a region of minimum temperatures and its sensitivity to changes in the

concentration of radiatively active species in the UTLS (Gettelman et al., 2011; Peevey et al., 2014). For example, Santer et al. (2003) showed that tropopause height is closely associated with tropospheric warming and stratospheric cooling. Thus, continuous identification and monitoring of the tropopause has become an important topic in atmospheric and climate research and enhanced understanding of tropopause behavior can contribute knowledge to a variety of topics (Feng et al., 2011; Randel et al., 2007).

The boundary between the tropics and extratropics is often characterized by a split in the tropopause rather than a smooth transition, which results in discontinuities observed near the subtropical jet. Along this boundary, considerable variation in tropopause height has been observed in previous studies. For example, Seidel & Randel (2007) showed that tropopause heights can display a bimodal structure throughout the subtropics using radiosonde data. In these regions, the tropopause is sometimes at the height of the tropical tropopause and other times at a height typical of the extratropical tropopause which results in a clear separation of about 3–5 km between the two modes. Most importantly, the authors state that this feature is not simply a reflection of seasonal variability, as high and low tropopauses are observed in all seasons at a given station, although on summer (winter) days the tropopause does tend to be high (low). However, one of the main restrictions of the study is the limited spatial coverage of the radiosonde data, which results in observations at only a few locations over land. Additionally, seasonal variation of tropopause heights was not analyzed in the study. The location and strength of the subtropical jet is known to vary considerably with season, which could have an impact on when and where tropopause bimodality occurs. Additionally, along the subtropical jet, the occurrence of multiple tropopauses have been found in atmospheric temperature profiles using radiosondes (e.g., Anel et al., 2008; Seidel & Randel, 2006) and satellite data (e.g., Castanheira

& Gimeno, 2011; Peevey et al., 2012). Much research has been done over the past few decades to better characterize this thermal structure. For example, it has been shown that a large percentage of temperature profiles display a double tropopause during the midlatitude winter (40-80%) and this frequency decreases into the summer (Peevey et al., 2012; Schmidt et al., 2006). Early studies about the synoptic structure of double tropopause environments showed that they are related to upper-level jet stream frontal zones (Shapiro, 1980) while later studies have related them to ozone variability (Pan et al., 2004) and tropopause folding (Anel et al., 2008; Schmidt et al., 2006). Randel et al. (2007) showed that double tropopauses occur when the low latitude (tropical) tropopause extends to higher latitudes, overlying the lower tropopause. Additionally, they form most frequently above strong cyclonic circulation systems as this results in a lower stability in the lower stratosphere. However, while tropopause bimodality and frequent occurrences of double tropopauses both generally occur throughout the subtropics, no clear relationship between the two has been established in the literature up to this point.

The accurate, high vertical resolution temperature profiles provided by GPS Radio Occultation (RO) afford a unique opportunity to observe tropopause structure and variability with a substantially higher vertical resolution and better coverage than is available with other data (Anthes et al., 2008). Many recent studies have utilized GPS RO for this purpose, especially as the data record becomes longer which allows for more robust climatological studies. For example, Rieckh et al. (2014) studied tropopause characteristics using GPS RO data from 2001 to 2013. They showed that variability in the subtropical tropopause break leads to a large spread in the tropopause height and temperature distribution in the 20° to 30° latitudinal band during winter. Additionally, they noted that the median tropopause height is systematically higher than the mean at these latitudes since most of the tropopause heights were at higher altitudes (e.g.,

tropical) but some also show extratropical characteristics. Double tropopauses displayed weak latitudinal variations, with most second tropopause heights between 14 to 20 km in the extratropical winter hemisphere and between 18 to 20 km in the tropics. Son et al. (2011) also studied the fine-scale structure of the global tropopause using COSMIC GPS RO measurements. The authors found interesting intraseasonal variabilities in tropopause properties. For example, tropopause temperature and pressure show significant variability in the subtropics along the subtropical jet in both hemispheres, the storm track regions in the winter hemisphere, and the Tibetan plateau in JJA. However, their variabilities are minimum and zonally homogeneous in the deep tropics, suggesting that tropical deep convection plays only a minor role there. Zhang et al. (2014) also studied the global tropopause climatology using GPS RO data and found that the largest seasonal variations of tropopause heights occur in the subtropics, with variations of 2 to 4 km observed within 30°-40° in both hemispheres. These results show that GPS RO provides a novel tool for monitoring tropopause variability, quantifying the relevant physical mechanisms, and measuring potential long-term changes (Anthes et al., 2008).

The purpose of this study is to better understand the climatological characteristics of the extratropical tropopause by examining tropopause bimodality and establishing how it relates to double tropopause occurrence. The three main questions we answer in this manuscript are as follows: 1) Where and when does tropopause bimodality occur? Tropopause bimodality has been shown to occur in specific locations and suggested to occur year-round, but a long global record of high-resolution temperature observations could provide additional insights into exactly where and when this phenomenon occurs; 2) What are the characteristics of the tropopause in the locations where bimodality occurs? When the tropopause displays bimodal characteristics, the synoptic environments are a combination of tropical and extratropical. Answering this question

will provide insight into climatology of the subtropical jet stream and how often each region observes each type of synoptic pattern; and 3) How does the occurrence of double tropopauses relate to bimodality? Double tropopauses have been shown to occur frequently throughout the subtropics (e.g., Anel et al., 2008; Castanheira & Gimeno, 2011; Peevey et al., 2012; Randel et al., 2007; Schmidt et al., 2006) in a similar location that tropopause bimodality has been identified to occur in, so answering this question could provide valuable insight into formation mechanisms and characteristics. To answer these questions, we use GPS RO soundings to identify tropopause heights, as GPS RO offers a relatively long data record of global observations of UTLS temperatures and tropopause heights with a high vertical resolution. The structure of the paper is as follows: Section 2 provides background on the GPS RO data used in this study; Section 3 describes the methodology used, including tropopause definitions and how tropopause bimodality is characterized; Section 4 presents the key results of the study, including displaying bimodal tropopause locations and characteristics and how they relate to double tropopause formation; Lastly, a summary is provided in Section 5.

4.2. Data Description

GPS Radio Occultation has emerged as a powerful technique in monitoring the Earth's atmosphere by providing global observations of temperatures with a high vertical resolution in all-weather conditions (Anthes et al., 2008). The atmospheric refractivity N depends on conditions in the dry atmosphere, water vapor, and the ionosphere (Smith & Weintraub, 1953):

$$N = 77.6 \frac{P}{T} + 3.73 \times 10^5 \frac{e}{T^2} - 4.03 \times 10^7 \frac{N_e}{f^2} \quad (1)$$

where P is the atmospheric pressure (in hPa), T is the temperature (in K), e is the partial pressure of water vapor (in hPa), N_e is the electron density (in electrons m^{-3}), and f is the transmitted

frequency (in Hz) (Danzer et al., 2014). The ionospheric contribution is ignored since the ionospheric correction already happens on bending angle level (Vorob'ev & Krasnil'nikova, 1994). In this study, dry temperature is used because it can be treated as an independent satellite retrieval, whereas the real temperature retrieval relies on a priori moisture information from ECMWF low resolution analysis. Note, however, the dry temperature retrieval is nearly identical to the real temperature in the UTLS region as moisture is negligible (Kursinski et al., 1997). To ensure this is the case, we only use dry temperatures < 240 K. The dry temperature is derived from the refractivity (1) by neglecting atmospheric humidity (Foelsche et al., 2008) such that:

$$T_{dry} = 77.6 \left(\frac{P_{dry}}{N} \right) \quad (2)$$

where P_{dry} is the dry pressure (i.e., the pressure without water vapor) derived through hydrostatic integration.

GPS RO soundings are obtained from the joint US-Taiwan six-satellite FORMOSAT-3/COSMIC (FORMOSA Satellite Series No. 3/Constellation Observing System for Meteorology, Ionosphere, and Climate) mission (Anthes et al., 2008). The COSMIC constellation provided up to 2,500 soundings per day shortly after launch in 2006 with relatively homogeneous sampling coverage around the globe. However, the number of daily soundings has decreased to roughly 250-300 per day at the end of 2017. We obtained the reprocessed level-2 RO profiles from CDAAC (COSMIC Data Analysis and Archive Center) at the University Center for Atmospheric Research (UCAR). The profiles are quality controlled by excluding the ones with “bad” flags (such as if the observation bending angles exceed the climatology by a specific threshold). We use the “atmPrf” product, which provides refractivity and dry temperature (T_{dry}) from usually near the surface up to ~60 km. The vertical resolution of RO soundings varies from 0.2 km in the lower troposphere to 1.4 km in the upper stratosphere

(Anthes et al., 2008) with an average of 0.5 km in the UTLS. The retrieved profiles are reported as a function of geometric height above mean sea level and the location of each profile nearest to the surface is used.

4.3. Methodology

To obtain extratropical tropopause climatological characteristics, COSMIC GPS RO temperature profiles are analyzed from 2006 to 2017. The thermal tropopause height is determined by the WMO lapse rate tropopause (LRT) definition (World Meteorological Organization (WMO), 1986): (1) The first tropopause is defined as the lowest level at which the temperature lapse rate decreases to 2 K km^{-1} or less, provided that the average lapse rate between this level and all higher levels within 2 km does not exceed 2 K km^{-1} ; (2) If above the first tropopause the average lapse rate between any level and all higher levels within 1 km exceeds 3 K km^{-1} , then a second tropopause can be defined by the same criterion as (1). Additionally, our tropopause-detection algorithm does not begin searching for the tropopause height until the height of the profile is 5 km above mean sea level to alleviate issues with dry temperature profiles in the lower troposphere. Each GPS profile is interpolated into a 10 m uniform vertical grid using a quadratic interpolation scheme and then smoothed to 500 m, which is roughly the native resolution for RO profiles in the UTLS altitude range. The GPS profiles are binned into 2.5° latitude x 5° longitude grids and then the median background tropopause characteristics for each season are derived (December-January-February, March-April-May, June-July-August, September-October-November). The number of temperature profiles in each seasonal grid generally ranges from 250-350 profiles throughout the extratropics.

Tropopause bimodality is evaluated using Otsu's method (Otsu, 1979), an automatic image thresholding technique that creates a binary image based on setting a threshold value on the pixel intensity of the original image to separate the foreground pixels from background pixels (e.g., Bangare et al., 2015; Senthilkumaran & Vaithegi, 2016). This method searches for the threshold that maximizes the inter-class variance of a histogram, which is defined as the weighted sum of variances of the two classes:

$$\sigma^2 = \omega_0\omega_1(\mu_1 - \mu_0)^2 \quad (3)$$

where ω are class weights, μ are class means, and the subscripts represent the two groups within the histogram. The method involves iterating through all the possible threshold values between each histogram bin and calculating a measure of spread for the pixel levels on each side of the threshold (so that the pixels fall in either the foreground or the background). Otsu's method can also be applied to other cases of unsupervised classification besides image thresholding in which a histogram is available of some feature (such as tropopause heights) that is discriminative for classification (Otsu, 1979). Otsu's method demonstrates good performance if the histogram displays a relatively deep valley separating two peaks. However, the performance of this technique can be limited by small sampling, small mean difference between the two classes, and large amounts of noise (Lee et al., 1990). Histograms of tropopause height distribution are generated for each grid in every season. Otsu's method is then applied to determine whether the tropopause displays a bimodal distribution in that location. Figure 4.1 displays the LRT height histograms and inter-class variances for DJF and JJA for a grid over Florida (27.5°-30°N, 80°-85°W). In DJF (Figure 4.1a), tropopause heights display a well-defined bimodal distribution, with two clear peaks and a sharp valley in between. The sum of the relative frequencies of each group of LRT heights show similar values (both near 50%) although the peak is considerably

larger for the higher heights. Additionally, an extremely large variety of heights are possible during the wintertime as heights range from 8.5 up to 19 km, indicating a mixture of tropical and extratropical environments occurring. The corresponding maximum variance (Figure 1c) is ~ 4.5 and occurs at 15 km. In contrast, the histogram for JJA (Figure 1b) displays a near-normal distribution and the tropopause is consistently high (tropical). There is a small range of LRT heights displayed which results in a very low maximum variance (Figure 1d) of ~ 0.5 .

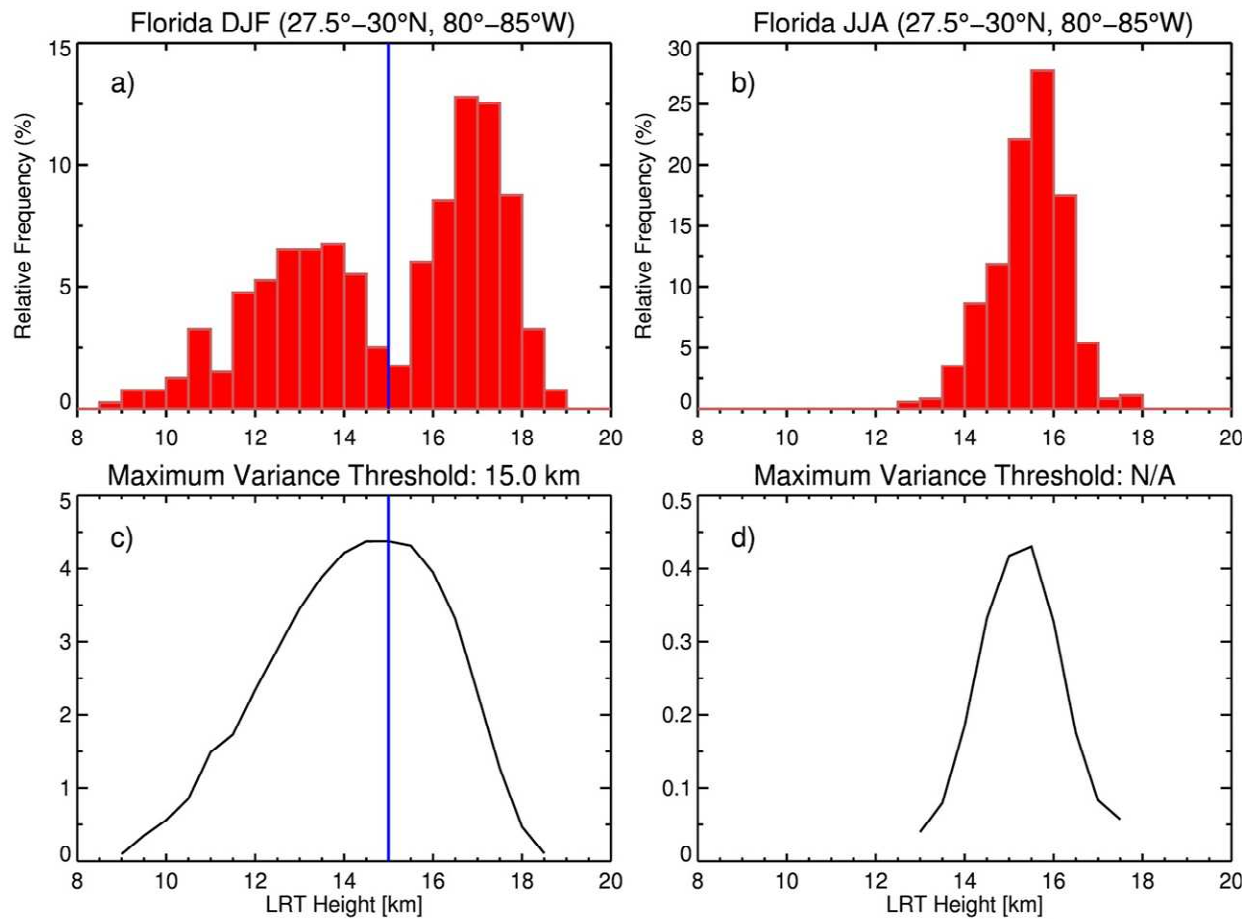


Figure 4.1. Tropopause height histograms and inter-class variances in DJF (a,c) and JJA (b,d) for a grid located over Florida (27.5°-30°N, 80°-85°W).

Additionally, careful analysis of a considerable number of tropopause height histograms around the globe throughout every season revealed that two constraints that must be implemented to ensure that the tropopause heights are properly classified as bimodal. This is necessary because the detection algorithm assumes that the input histogram always has a bimodal distribution and most locations around the globe do not experience tropopause bimodality. These criteria are 1) the sum of the relative frequency of occurrences for each class must be at least 10%, and 2) the maximum inter-class variance of the histogram must be at least 2.5. While these additional criteria may seem somewhat arbitrary, they ensure that the results only show locations that display a bimodal LRT height distribution and remove erroneous bimodal classifications, especially in many high latitude locations in which large tropopause height variation occurs. For example, over the high latitude North Atlantic Ocean in winter, large maximum variances (~ 2) are observed even though histograms show a near normal distribution because a wide range of tropopause heights can occur during the winter at these locations.

4.4. Results

4.4.1 Bimodal Tropopause Locations and Characteristics

This section examines the bimodality of the extratropical tropopause by determining where and when bimodality occurs and what the characteristics are of each mode. We first examine four locations analyzed by Seidel & Randel (2007; hereafter SR2007) that were classified as bimodal tropopause regions. These locations were studied using radiosonde data from 1979-2005 along with collocated NCEP/NCAR reanalysis data. The authors state that the bimodal tropopause feature is not simply a reflection of seasonal variability as high and low tropopauses are observed in all seasons at a given station, although on summer (winter) days the

tropopause does tend to be high (low) (Seidel & Randel, 2007). However, it must be noted that the analysis in the manuscript does not separate the data into different seasons. Figure 4.2 displays the seasonal probability density functions (PDFs) of tropopause heights for the four SR2007 locations. The tropopause data is binned using 1-km bins from 5 km to 20 km. We note that our locations are gridded (2.5° lat x 5° lon) due to GPS RO sampling characteristics. Right away, a distinct seasonality in tropopause heights is observed in each region. In Beit Dagan (Figure 4.2a), bimodality occurs in DJF and MAM with very similar PDFs, as there are two well-defined peaks with deep valleys in-between. However, bimodality is not evident in JJA and SON. Large peaks occur above 15 km (characteristic of the tropical tropopause) during these seasons with less-frequent occurrences of the lower tropopause heights. For Kashi (Figure 4.2b), seasonality is also observed but with opposite characteristics. Bimodality is now only observed in JJA and SON, with JJA displaying the larger peak for the higher (tropical) tropopause heights whereas the larger peak during SON is observed for the lower (extratropical) heights. In contrast, heights throughout DJF and MAM are almost exclusively of the extratropical variety. This difference between Beit Dagan and Kashi can be attributed to the differences in latitude, as Kashi is much farther north and experiences extratropical heights more frequently. At Perth (Figure 4.2c), bimodality is observed in three seasons (MAM, JJA, and SON). In JJA, the total occurrence frequency of each mode is very similar whereas MAM and SON are skewed towards the tropical heights. The results at Durban (Figure 4.2d) are comparable, as bimodality is also observed in MAM, JJA, and SON with similar modal characteristics displayed. This result indicates that there is considerable seasonal variability in tropopause bimodality which contrasts with the results and statement provided in SR2007. Each location experiences large differences

in the occurrence frequency of the tropical and extratropical mode, and these variations occur due to seasonal variations in the location and strength of the subtropical jet (Peevey et al., 2012).

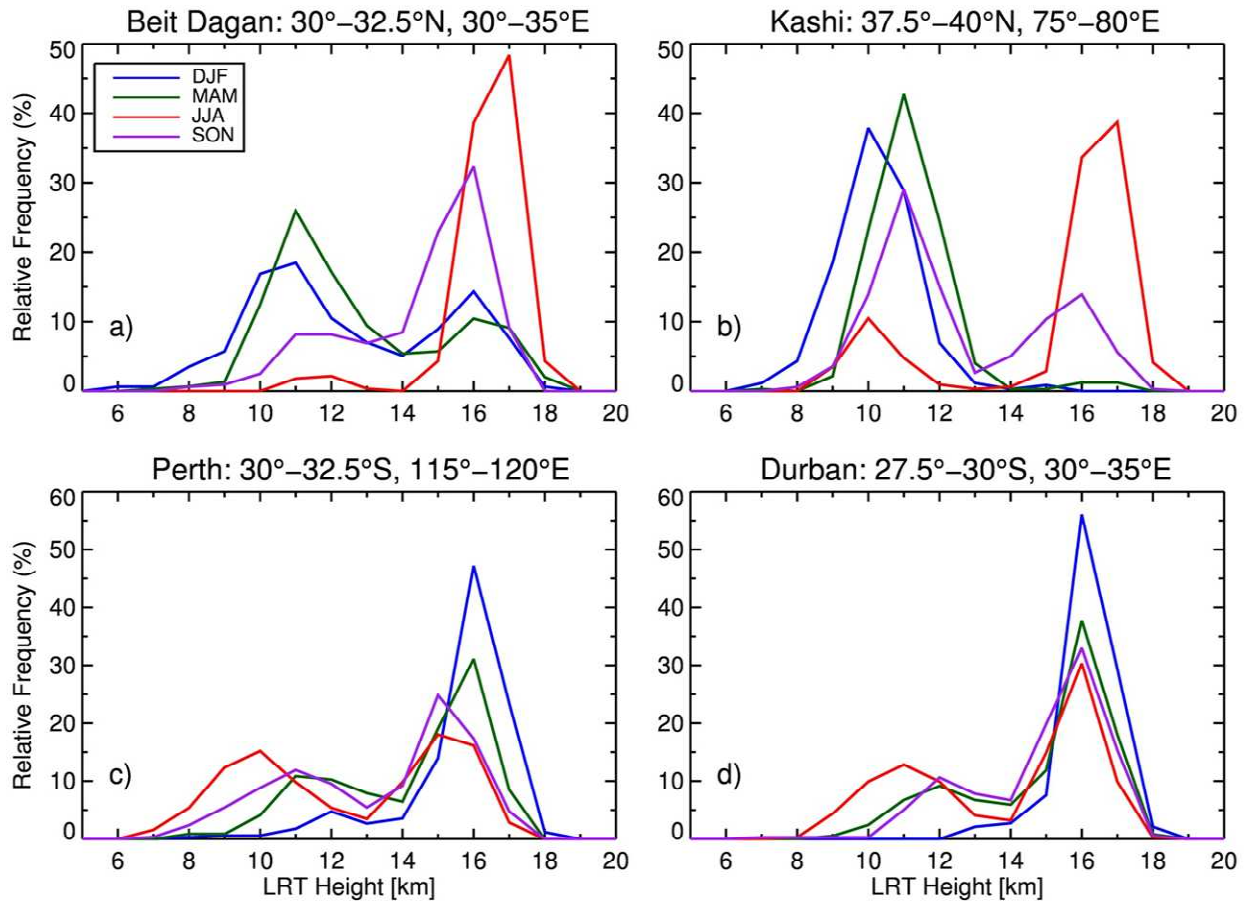


Figure 4.2. Probability distribution functions (PDFs) of tropopause heights (km) in DJF (blue), MAM (green), JJA (red), and SON (purple) for Beit Dagan (a), Kashi (b), Perth (c), and Durban (d).

The next set of figures expand upon bimodal tropopause features by showing when/where tropopause bimodality occurs globally and what the characteristics are. Figure 4.3 shows the seasonal locations of bimodal tropopauses along with the altitude that separates the two modes. In general, bimodality occurs more frequently during the winter due to a stronger subtropical jet

and temperature contrasts (Randel et al., 2007). In DJF (Figure 4.3a), bimodality occurs in the Northern Hemisphere continuously throughout, on average, a $\sim 10^\circ$ - 20° wide band between 20° - 40° with considerable zonal variations due to the location of the subtropical jet. Bimodality in the Southern Hemisphere generally displays a width of $\sim 10^\circ$ and demonstrates much less meridional movement, except off the western coast of South America. The threshold separating the two modes is generally highest in DJF, with many locations on the tropical side of the band experiencing height threshold values above 14.5 km. This occurs because the tropical tropopause heights are typically highest in DJF (~ 17 km) and lowest in JJA (~ 16 km) (Zhang et al., 2014). Substantial height threshold differences occur in Northern Hemisphere DJF, with ranges reaching 3 km or more between the northern and southern side of the band in the Northern Pacific. In MAM (Figure 4.3b), the Northern Hemisphere bimodal band begins to shrink in extent throughout the Western Hemisphere, with most of the occurrence relegated to the North American continent along with having high threshold values (≥ 14.5 km). However, occurrence remains similar to DJF throughout the Eastern Hemisphere or even increases in extent over the Asian continent. The Southern Hemisphere bimodal band characteristics are almost identical to DJF except for a slight shift equatorward ($\sim 5^\circ$) and a reduction in the tropical “tail” off the west coast of South America. In JJA (Figure 4.3c), the only remaining bimodal region throughout the Northern Hemisphere is over continental Europe and Asia. This region is much farther north (generally between 40° - 50°) and is associated with the Asian monsoon circulation. The Asian monsoon circulation includes a strong anticyclonic flow in the UTLS and double tropopauses frequently occur on the poleward flank of this anticyclonic circulation (the region of westerly zonal winds), where the tropical tropopause (near 16 km) extends poleward to almost 60° (Randel et al., 2007). As a result, threshold heights remain relatively high (mainly between 13.5-

14.49 km) even at these higher latitudes. In the Southern Hemisphere winter, zonal extent remains relatively similar to the other seasons, although the threshold height is generally lower. In general, bimodality occurs more frequently in the Northern Hemisphere winter, similar to double tropopause frequencies shown in Peevey et al. (2012). This could be due to hemispheric differences in land-ocean distribution (Schmidt et al., 2006), as the number of large mountain ranges in the Northern Hemisphere enhances the propagation of topographically forced planetary waves. In SON (Figure 4.3d), Northern Hemisphere bimodal extent begins to increase, especially throughout the West (such as over the northern United States). The location continues to remain at relatively higher latitudes (exclusively poleward of 30° and up to almost 50°) and height thresholds are dependent on latitude.

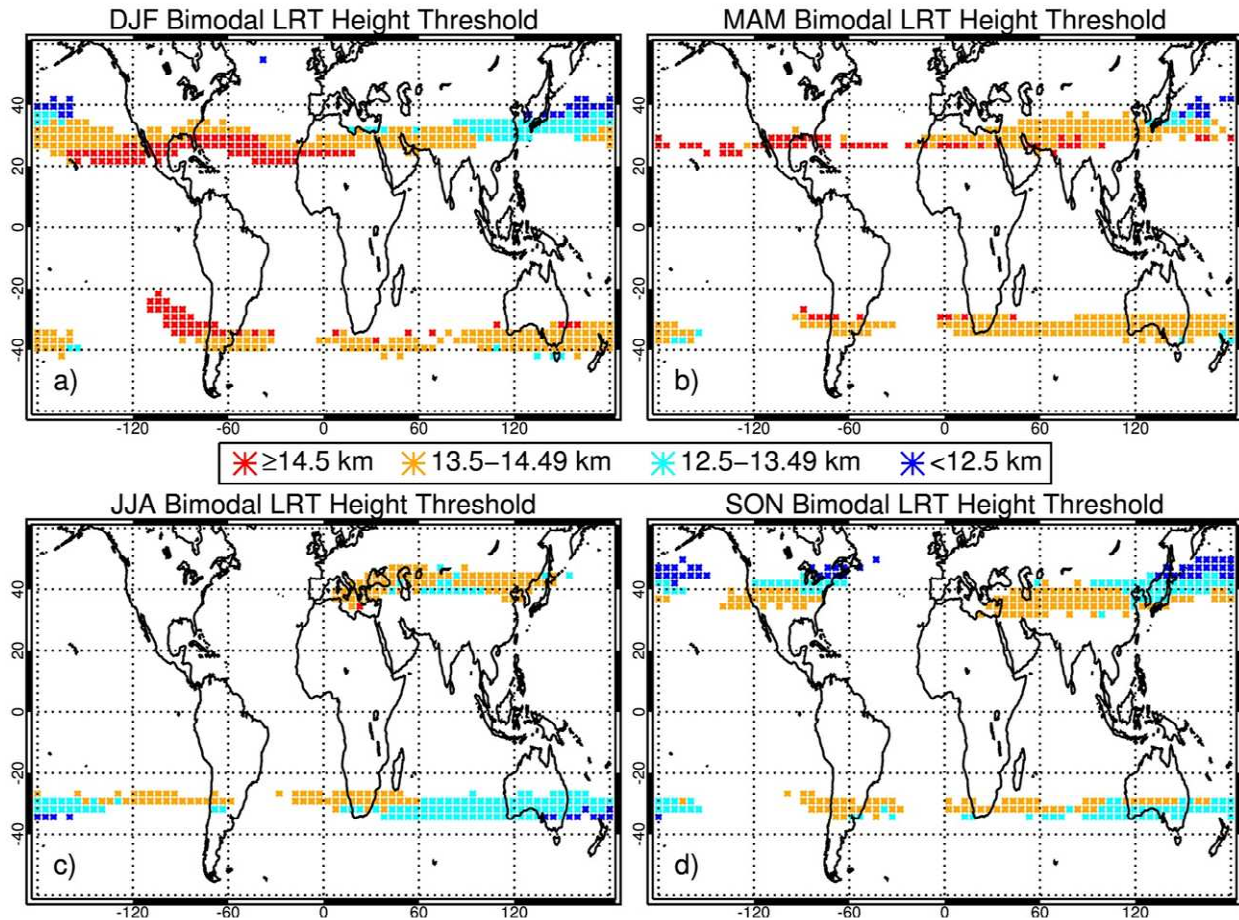


Figure 4.3. Seasonal distribution (a: DJF, b: MAM, c: JJA, d: SON) of bimodal tropopause height locations and threshold values for separating the two modes.

Next, we expand on the previous figure by showing the total relative frequency of occurrence for profiles with tropopause heights within the lower mode in Figure 4.4. As expected, the modal frequency of occurrence displays a distinct shift within each band of bimodal tropopause heights within all seasons, as the tropical side of the band typically has fewer profiles with tropopause heights within the lower mode (<40% occurrence) whereas the extratropical side has many more occurring within the lower mode (>60%). This shift occurs relatively quickly (over the course of 2.5°-5° latitude) due to the characteristic “tropopause

break” that occurs at this latitude, as the tropopause dips rapidly from the tropics to the extratropics. Double tropopauses also occur frequently around this region. These features are also associated with the characteristic break in the thermal tropopause near the subtropical jet where the tropical tropopause extends to higher latitudes, overlying the lower extratropical tropopause (Randel et al., 2007). Thus, the observed bimodality, especially along the tropical side of the bimodal region, may be directly related to these double tropopause environments and is investigated further in the next section.

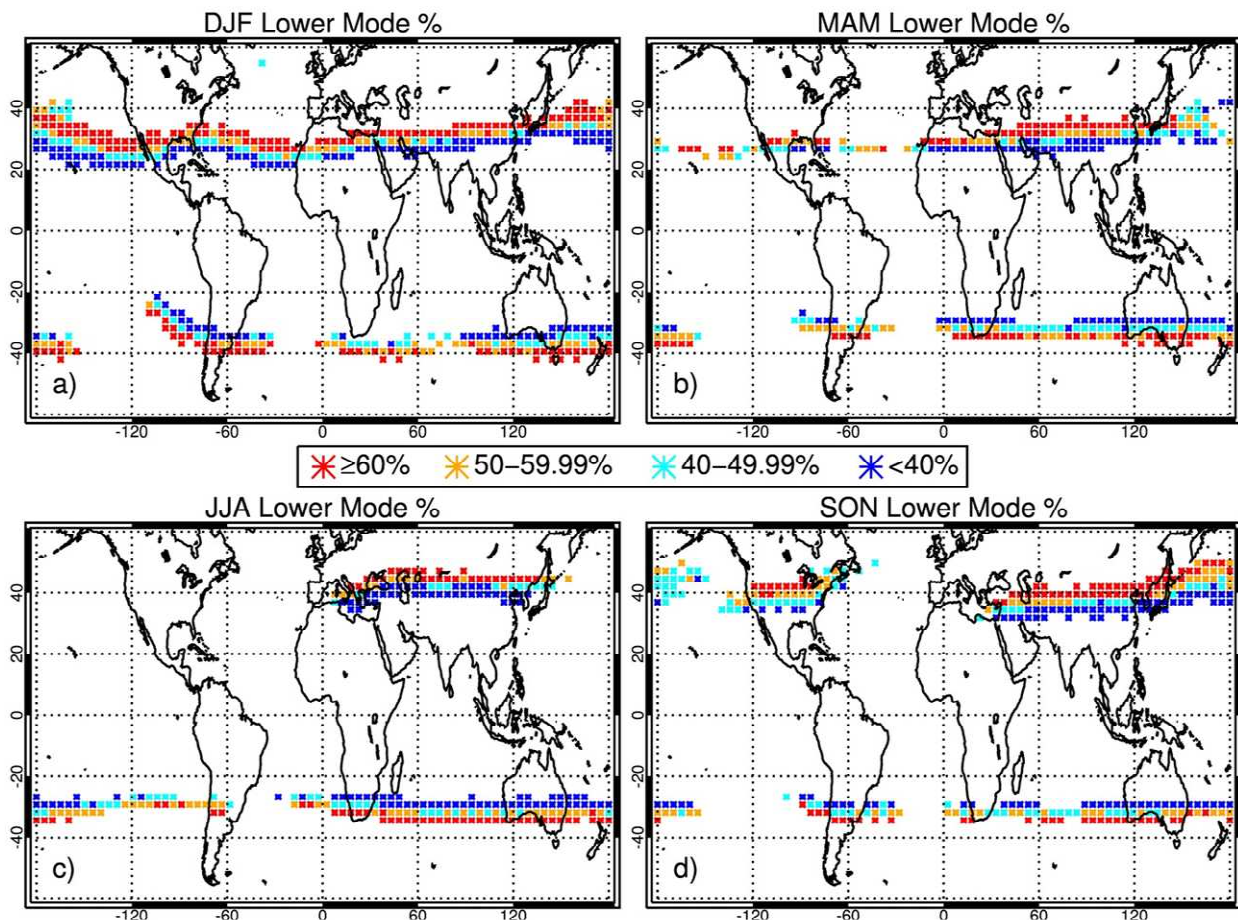


Figure 4.4. Seasonal distribution (a: DJF, b: MAM, c: JJA, d: SON) of bimodal tropopause height locations and total relative frequency of occurrence (%) of profiles with tropopause heights within the lower mode.

4.4.2 Relationship of Double Tropopause Environments to the Occurrence of Bimodality

This next section will investigate the relationship between double tropopauses and bimodality. First, it is useful to show what typical DT temperature profiles often look like in order to get a better idea of the type of synoptic environment present. Figure 4.5 shows individual profiles with DTs from the same SR2007 regions discussed in Figure 4.2 (Beit Dagan, Kashi, Perth, and Durban) during specific seasons whenever bimodality is occurring. There are two profile types shown for each location: the blue profile is when the first (lower) LRT height is below the bimodal tropopause height threshold and the red profile is when it is above the threshold. In Beit Dagan (Figure 4.5a) and Perth (Figure 4.5c), the profiles are obtained from the winter while the profiles for Durban (Figure 4.5d) are obtained from the fall. For all three locations, the two types of profiles look considerably different. The DT profiles with tropopause heights in the lower mode (LM) all have tropopause heights below 12 km. A strong inversion occurs just above the tropopause and this layer is known as the tropopause inversion layer, which is a region of enhanced static stability above the extratropical tropopause associated with a narrow-scale temperature inversion (Randel & Wu, 2010). This layer can be as shallow as 1 km (such as near Durban) or as thick as 4 km (such as near Beit Dagan). Then, above this layer, the temperatures begin to decrease again (albeit at a different lapse rate compared to below the first tropopause) until reaching a second tropopause near the typical tropical tropopause height (e.g., 17 km near Durban). In contrast, the DT profiles with tropopause heights in the upper mode (UM) display a much warmer upper troposphere (up to 5 K). However, temperatures quickly become colder above the LM profile's first tropopause, and the UM profile's tropopause is generally 5-10 K colder. This indicates two different types of synoptic environments present

(tropical vs. extratropical). Additionally, profiles are shown for Kashi (Figure 4.5b) but are taken from the summer. These two profiles look very similar, but the main difference is the strength of the inversion around 10-11 km. The inversion is strong and well-defined in the LM profile but is not strong enough in the UM profile to be classified as a tropopause using the WMO definition. These differences are likely due to the previously discussed Asian monsoon circulation. The strength of the anticyclonic circulation and associated westerly winds influences the type of profile observed, as a stronger circulation will produce a stronger inversion (and vice versa).

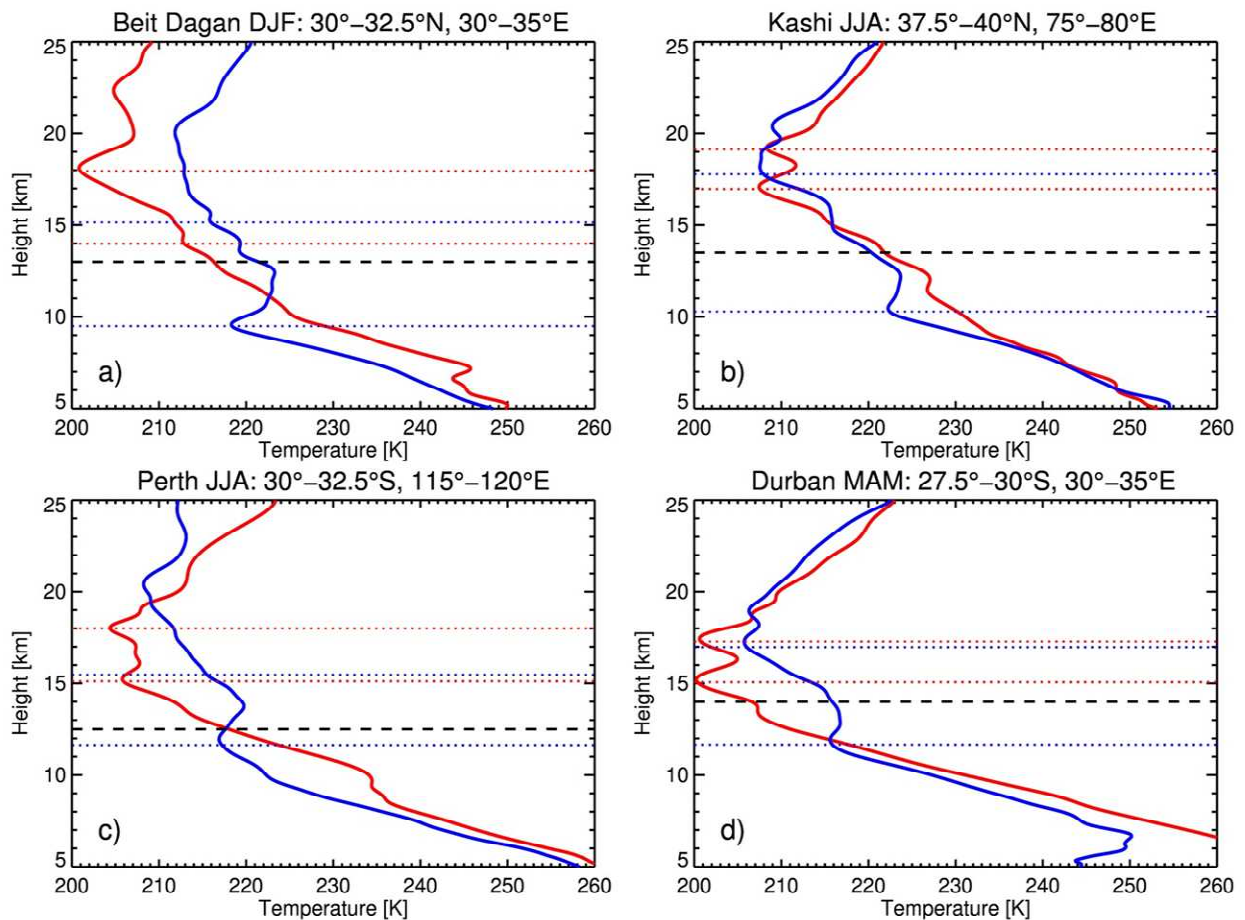


Figure 4.5. Typical individual double tropopause profiles when the first (lower) LRT height is below (blue) and above (red) the bimodal tropopause height threshold in each respective region for Beit Dagan (a), Kashi (b), Perth (c), and Durban (d). The blue and red dotted lines are the

locations of the first and second tropopause heights, while the black dashed line is the bimodal height threshold.

It is important to show where and how frequent double tropopauses happen to obtain a better idea of how their occurrence relates to bimodal tropopause height distributions. Figure 4.6 displays the seasonal double tropopause frequency of occurrences along with the locations that display a bimodal distribution of LRT heights. Double tropopause frequencies are generally highest in the winter in each hemisphere, as NH DJF (Figure 4.6a) shows a large area of frequencies >50% (with some values between 60-70%) along the poleward edge of the bimodal region and SH JJA (Figure 4.6c) also displays a few areas with >50% frequency of occurrences. These values tend to decrease slowly through the seasons, with NH minimum frequencies occurring in SON and SH minimum frequencies occurring in MAM (generally <35%). Additionally, frequencies decrease rapidly towards the tropical side of where bimodality occurs as many locations observe frequencies <20%. Overall, the DT frequencies shown here agree relatively well with previous research on DT frequency, although our values are slightly lower than Schmidt et al. (2006), which saw maximum frequencies over 80% in some locations, and slightly higher than Peevey et al. (2012), which generally saw frequencies up to 50%. Both studies relate the high frequency of DTs in the subtropics to the zonal mean wind speeds at 200 hPa, as the maximum zonal wind at this altitude serves as a rough indicator for the mean location of the jet streams (Peevey et al., 2012; Schmidt et al., 2006). The location of the bimodal region is generally close to the locations that experience a high frequency of DTs. However, the regions do not display a perfect overlap, as the highest DT frequencies often continue poleward beyond where bimodality was identified for up to 5°-10°.

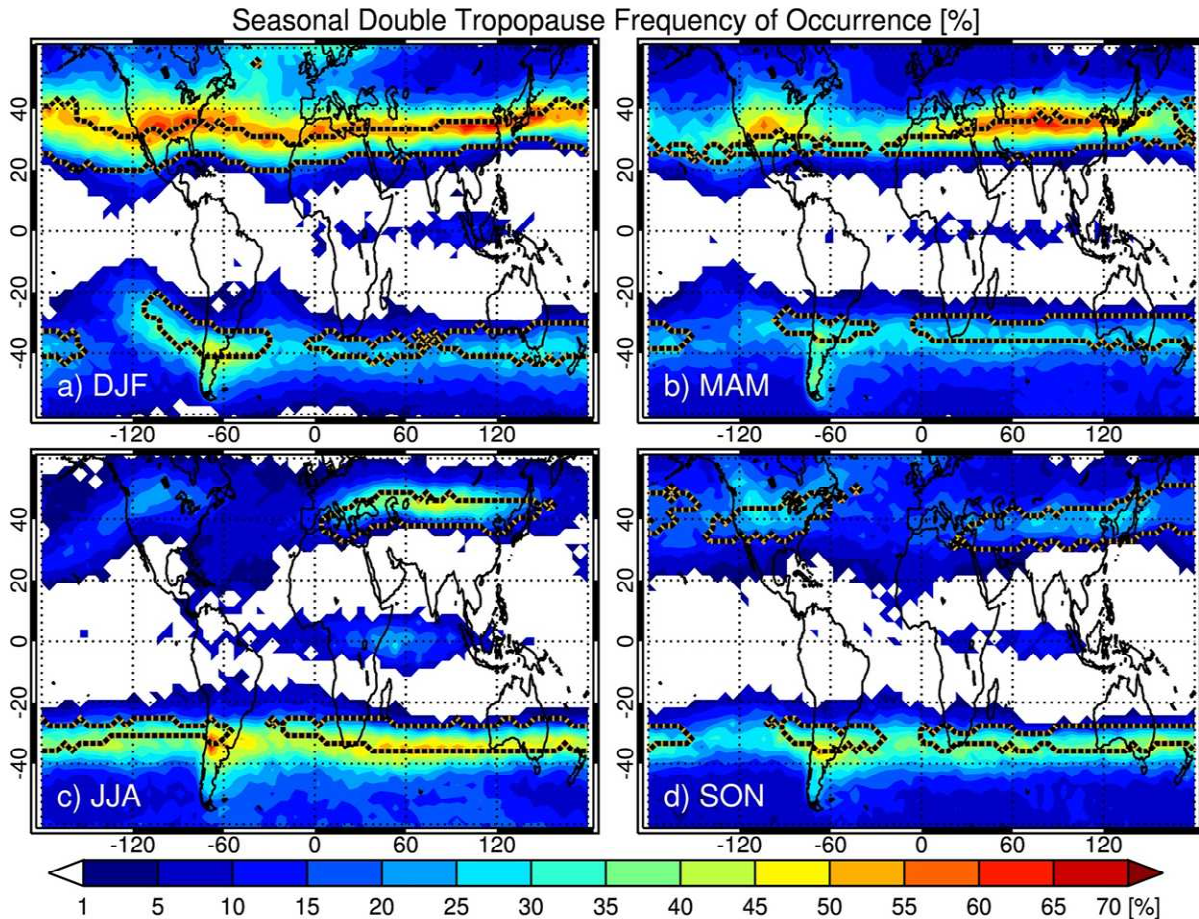


Figure 4.6. Seasonal distribution (a: DJF, b: MAM, c: JJA, d: SON) of the total frequency of occurrence (%) of temperature profiles with double tropopauses observed. The region that displays LRT height bimodality is outlined by the black and gold contours.

It is also useful to establish the type of environments most frequently associated with the formation of DTs and how the lower tropopause forms in these profiles. Thus, Figure 4.7 shows the percentage of double tropopause profiles that have their lower (first) tropopause height within that grid's lower mode. Similar to Figure 4.6, there is a distinct meridional shift in the percentage of profiles that have their first tropopause (LRT1) within the lower mode. For example, in DJF (Figure 4.7a), DT profiles from almost the entire poleward side of the NH

bimodal band have a lower, or extratropical, tropopause height, as most grids display values of >80% (and some percentages are as high as 95%). In contrast, many grids on the tropical side of the bimodal band observe percentages of <50%. This indicates that often the lower tropopause at these latitudes is not necessarily of an extratropical origin. Additionally, there is a strong zonal dependence in the Northern Hemisphere, as latitudes such as 30° show considerable variation (such as percentages in Southeastern Asia <50% compared to the Eastern Pacific percentages of >80%). This same general pattern is evident across the rest of the seasons in the Northern Hemisphere. Less variation is evident in the Southern Hemisphere as most grids observe frequencies of >65%, except in JJA (winter) and SON (spring). This result shows that not all double tropopause environments are the same. While most DTs do in fact produce LRT1 heights of extratropical origin (in the lower mode), often over half of DT profiles have higher tropopause heights within the upper mode. Even though most of these bimodal locations on the tropical side of the bimodal band have lower DT frequency of occurrences (generally <35%), these types of profiles would play a significant role in tropopause bimodality in these locations.

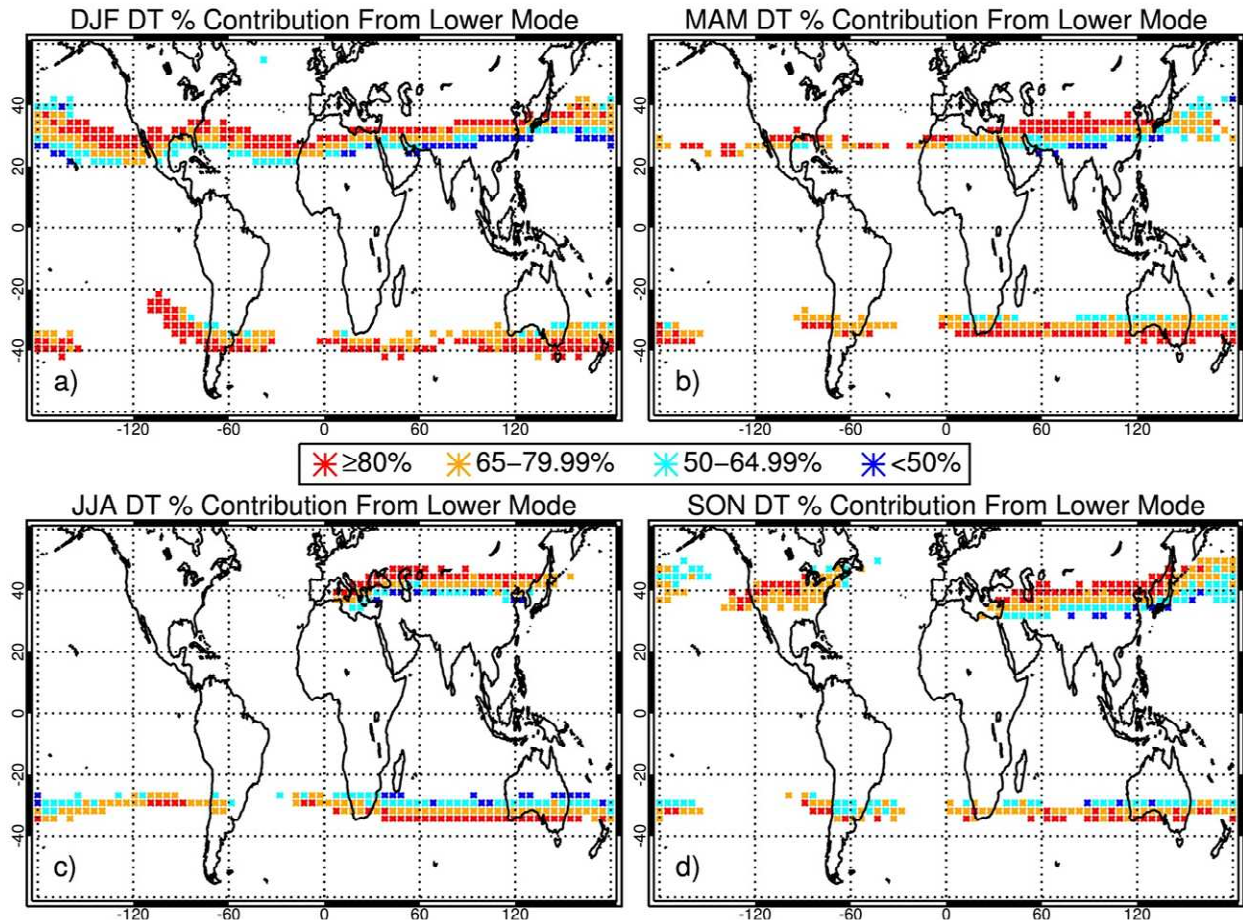


Figure 4.7. Seasonal distribution (a: DJF, b: MAM, c: JJA, d: SON) of bimodal tropopause height locations and the percentage of double tropopause profiles that have their first (lower) tropopause height within the lower mode.

The previous figure indicates that not all temperature profiles with double tropopauses are identical. Even though most DT profiles do have their LRT1 within the lower mode (e.g., of extratropical origin), there are still some with their LRT1 within the upper mode. Characterizing the different structures of these two types of DT profiles is important in analyzing their synoptic environments and how DTs contribute to bimodal tropopause height distributions. Figure 4.8 shows the gridded seasonal mean temperature profiles for double tropopause profiles with

tropopause heights within the lower mode (solid lines) and the upper mode (dashed lines). Two Northern Hemisphere and two Southern Hemisphere grids were chosen based on bimodality occurring throughout most or all of the year in order to allow for more seasonal comparisons. Bimodality does not occur year-round in any Northern Hemisphere grids (so locations with only 3 bimodal seasons sans JJA were chosen) whereas it does occur year-round in a few Southern Hemisphere grids. Right away, two different types of double tropopause synoptic environments are apparent for each location. In Figure 4.8a, profiles with lower mode DT profiles look very similar throughout all seasons, with LRT1 heights generally between 11-12 km and second tropopause (LRT2) heights near 17-18 km. In contrast, upper mode mean DT profiles in this region look more like single-tropopause tropical profiles as the finer scale features are smoothed out in the mean profiles, but little variation is evident again between the seasons. The lower mode profiles are generally 5-10 K colder throughout the upper troposphere but generally become ~5 K warmer above the lower mode profile's LRT1. More seasonal variation is evident in Figure 4.8b, as both the lower mode and upper mode mean profiles display large differences in temperature at all altitudes along with tropopause height location. Both Southern Hemisphere locations (Figures 4.8c and 4.8d) display profile characteristics that look relatively similar. For example, the LM and UM mean profile temperature magnitude, LRT1 heights, and profile shape are almost the same in each season. In summary, these profiles provide additional evidence that there are considerable differences between double tropopause profiles depending on what altitude the LRT1 is occurring at, and these differences provide insight as to which large-scale environment is influencing the location at each time (tropical vs. extratropical).

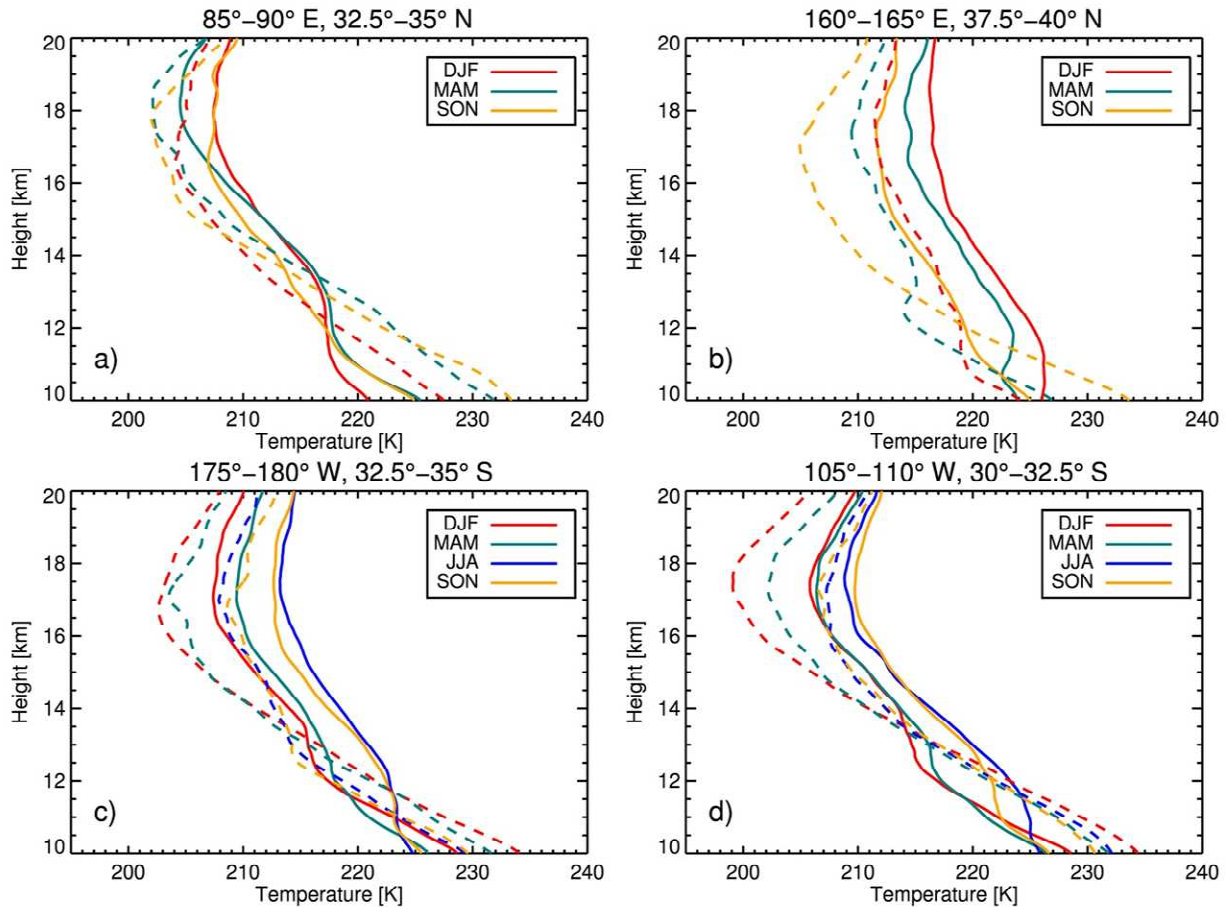


Figure 4.8. Seasonal mean temperature profiles within four grids for double tropopause profiles with tropopause heights within the lower mode (solid lines) and the upper mode (dashed lines) for DJF (red), MAM (teal), JJA (blue), and SON (orange).

In the last two figures, profiles are classified by whether they have one or two tropopause heights in order to establish how tropopause bimodality changes for each type of profile and help determine which type of profile impacts the occurrence of bimodality in different locations. Bimodality is shown for double tropopause profiles in Figure 4.9 along with the altitude for separating the two modes. In general, the bimodal band is slightly reduced in extent relative to the results shown for all profiles (e.g., Figure 4.3), although in some locations its occurrence is

eliminated almost completely (such as over North America in SON). The locations of occurrence are generally more towards the tropical side of the previously identified bimodal region, as large portions of bimodality between 30°-40° now do not occur. The height threshold separating the two modes is generally lower for double tropopause grids in locations that overlap with all profiles, as the threshold is typically one category lower (e.g., up to 1 km lower). This indicates that double tropopause profiles often result in lower bimodal thresholds since their LRT1 heights are typically lower than the LRT1 height of single-tropopause profiles, even when both profiles are extratropical (lower) in nature.

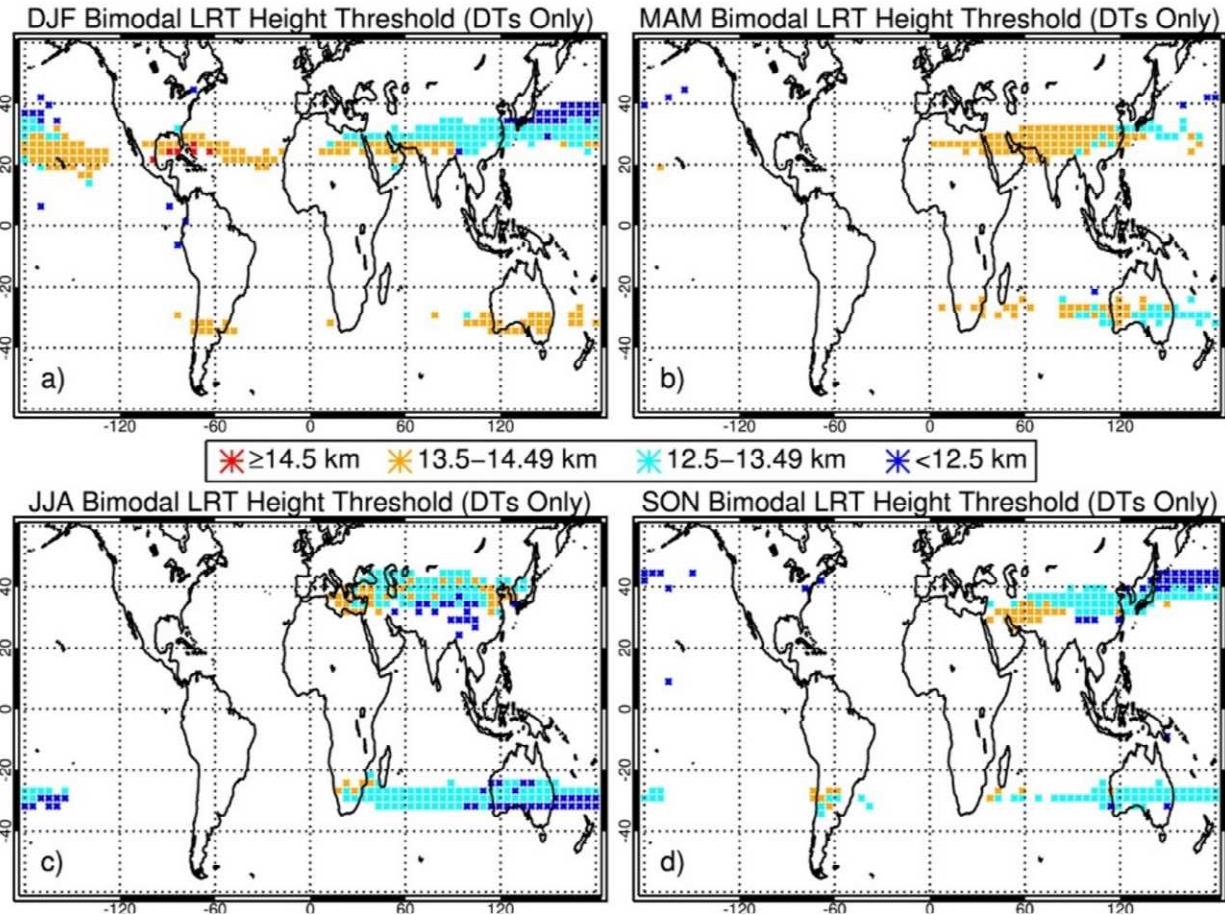


Figure 4.9. Seasonal distribution (a: DJF, b: MAM, c: JJA, d: SON) of bimodal tropopause height locations for profiles that have double tropopauses identified and threshold values for separating the two modes.

Finally, we look at where bimodality occurs when only considering profiles that have been identified as having a single tropopause and display the altitude for separating the two modes in Figure 4.10. The bimodal band becomes much smaller in extent when studying single tropopause profiles, as its maximum width is generally only 2.5° - 7.5° and shows many additional gaps. The location is shifted toward the poleward edge of the previously identified bimodal region throughout all seasons. For example, in DJF (Figure 4.10a), the NH band is confined between 30° - 40° whereas before, many locations also observed bimodality between 20° - 30° . This shift towards the poleward edge continues for all seasons and both hemispheres, and in some locations the single tropopause bimodal band shifts poleward even slightly beyond the bimodal band displayed for all profiles. At the same time, the height threshold is generally higher for single tropopause-only grids in locations that overlap with all profiles, as the threshold is often one category higher (e.g., up to 1 km). This result, along with the other results previously shown, suggests that two main factors contribute to the occurrence of seasonal tropopause bimodality. On the tropical side of the bimodal band, bimodality is mainly due to the occurrences of double tropopauses. At these latitudes, profiles with only one tropopause identified are almost always more tropical in nature, as LRT heights are higher and occur in the upper mode (hence no bimodality shown in Figure 4.10). However, when double tropopause profiles occur at these latitudes (which is typically <30% of the time), their LRT1 heights are often occurring within the lower mode (between ~40-65% of the time), which results in bimodality. On the other hand, on

the polar side of the bimodal band, the main reason bimodality occurs is due to single tropopause profiles that are more tropical in nature. At these latitudes, double tropopauses occur very frequently (often >50% of the time) and when they do occur, their LRT1 height is almost always within the lower mode (>80% of the time and even up to 95%). Thus, if only double tropopause profiles are considered, most of these locations would not be classified as bimodal. However, single tropopause profiles have a mixture of lower (extratropical) and upper (tropical) mode tropopause heights occurring; hence, the bimodality seen at these latitudes in Figure 4.10.

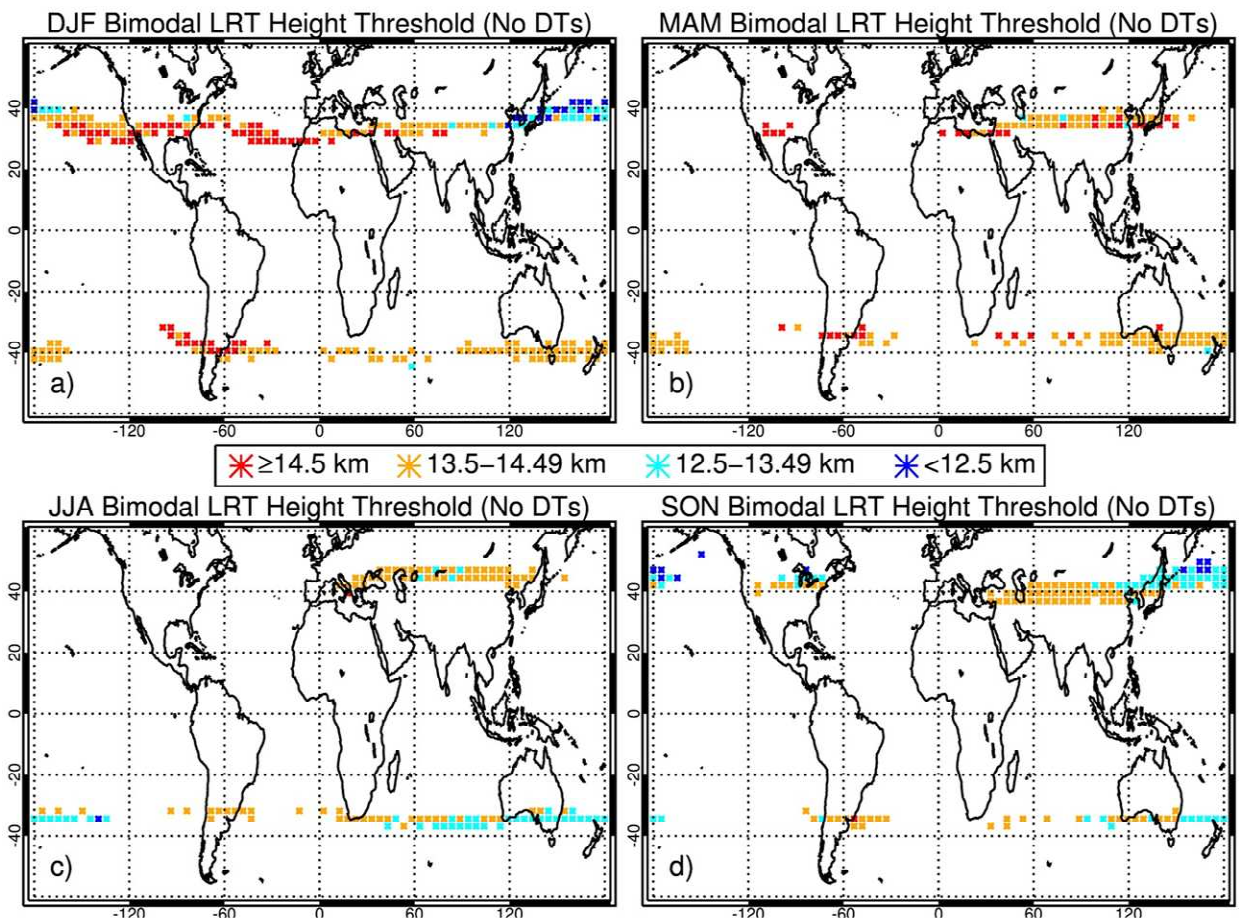


Figure 4.10. Seasonal distribution (a: DJF, b: MAM, c: JJA, d: SON) of bimodal tropopause height locations for profiles that only have a single tropopause identified and threshold values for separating the two modes.

4.5. Summary

In this paper, climatological characteristics of the extratropical tropopause were examined in order to determine where and when does tropopause bimodality occurs, what the tropopause characteristics were in these bimodal regions, and how the occurrence of double tropopauses relates to bimodality. First, four locations were chosen from the SR2007 paper (Beit Dagan, Kashi, Perth, Durban) to determine when bimodality occurred (Figure 4.2). A distinct seasonality in tropopause heights was observed in each region, which contrasts with the statement provided in SR2007 that bimodality occurs year-round in these locations. Additionally, each location experiences large differences in the occurrence frequency of the tropical and extratropical mode.

Seasonal bimodal characteristics and a global distribution of when/where bimodality occurs were shown. Bimodality occurs more frequently during the winter due to the stronger subtropical jet and temperature contrasts. Bimodality occurs in the Northern Hemisphere winter in a $\sim 10^\circ$ - 20° wide band between 20° - 40° with considerable zonal variations due to the location of the subtropical jet. This band shrinks throughout spring and into summer as temperature contrasts weaken. However, bimodality persists in the summer over northern Asia due to a strengthening of the Asian monsoon circulation. Bimodality in the Southern Hemisphere generally displays a width of $\sim 10^\circ$ in all seasons and demonstrates much less meridional movement. In general, bimodal threshold heights (Figure 4.3) remain relatively high (>13.5 km) on the tropical side of the band and decrease quickly on the polar side of the band (<12.5 km) except in the Northern Hemisphere summer. The total relative frequency of occurrence for profiles with tropopause heights within the lower mode was also shown (Figure 4.4). There is a

distinct shift in frequencies within all seasons, as the tropical side of the band typically has fewer profiles with tropopause heights within the lower mode (<40% occurrence) whereas the extratropical side has many more occurring within the lower mode (>60%). This occurs relatively quickly (within 2.5°-5° latitude) due to the characteristic “tropopause break” that occurs at these latitudes.

The relationship between double tropopauses and bimodality was also investigated. Seasonal double tropopause characteristics within the bimodal tropopause height regions were shown, such as the frequency of occurrence (Figure 4.6). The location of the bimodal region is generally close to the locations that experience a high frequency of DTs. DT frequencies are highest in the winter. For example, NH DJF sees a large area of frequencies >50% along the poleward edge of the bimodal region and SH JJA also displays a few areas with >50% frequencies. These values tend to decrease steadily through the seasons. Additionally, frequency of occurrence decreases rapidly towards the tropical side of the bimodal band, with many locations seeing frequencies between 20% to 30%. Previous studies (e.g., Peevey et al., 2012; Schmidt et al., 2006) have shown a strong relationship between the high frequency of DTs in the subtropics to the zonal mean wind speeds at 200 hPa, as the maximum zonal wind at this altitude serves as a rough indicator for the mean location of the jet streams. The percentage of double tropopause profiles that have their LRT1 within that grid’s lower mode was also shown (Figure 4.7). There is a distinct meridional shift in this percentage, as DT profiles from the poleward side of the bimodal band have a lower (extratropical) tropopause height (values of >80% with some up to 95%) whereas in contrast, many grids on the tropical side of the bimodal band observe percentages of <50%. This indicates that not all double tropopause environments are the same. While most DTs do have extratropical LRT1 heights (e.g., within the lower mode), certain

regions observe DT profiles with higher LRT1 heights more frequently (more tropical in nature). To examine this more closely, gridded seasonal mean temperature profiles for DT profiles with LRT1 heights within the LM and the UM were shown (Figure 4.8) in regions that experience bimodality through most or all of the year. Considerable differences are observed at each location between mean double tropopause profiles depending on what altitude the LRT1 is occurring at, and these differences provide more evidence as to which large-scale environment is influencing the location at each time (tropical vs. extratropical) and why bimodality is occurring. Finally, bimodal locations were shown for profiles that have been identified as having double tropopauses (Figure 4.9) or only having a single tropopause (Figure 4.10) along with their threshold altitudes. For double tropopause profiles, bimodality is slightly reduced in extent and shifts towards the equatorward edge of the previously identified bimodal region. The bimodal height threshold is generally lower for double tropopause-only grids that overlap with all profiles. On the other hand, the bimodal band becomes much smaller in extent (2.5° - 7.5°) for single tropopause profiles and shows many additional gaps. Its location is shifted toward the poleward edge of the previously identified bimodal region throughout all seasons and in both hemispheres. The bimodal height threshold is also generally higher for single tropopause-only grids in locations that overlap with all profiles.

The results shown here suggest that two main factors contribute to the occurrence of seasonal tropopause bimodality. On the tropical side of the bimodal band, bimodality is mainly due to the occurrence of double tropopauses. At these latitudes, profiles with only one tropopause identified are almost always tropical in nature with LRT1 heights in the upper mode. However, when double tropopause profiles occur at these latitudes, their LRT1 heights are often occurring within the lower mode, which results in bimodality. On the other hand, on the polar

side of the band, the main reason bimodality occurs is due to single tropopause profiles that are more tropical in nature. At these latitudes, double tropopauses occur very frequently and their LRT1 height is almost always within the lower mode. Thus, if only double tropopause profiles are considered, most of these locations would not be classified as bimodal. However, single tropopause profiles have a mixture of extratropical and tropical LRT1 heights which results in the observed bimodality. Further research on this topic is planned farther down the line as more GPS RO data becomes available. A longer-term trend analysis of how tropopause bimodality is changing could be useful in providing a better understanding of tropopause behavior and interactions between the tropics and extratropics.

Acknowledgements

Funding for this research was provided by NASA grants (NNX14AK17G and NNX15AQ17G). Special thanks to the program managers Dr. Ramesh Kakar and Dr. Lucia Tsaoussi for the support of the project. GPS RO soundings were obtained freely from the University Corporation for Atmospheric Research (<http://cdaac-www.cosmic.ucar.edu/cdaac/products.html>).

CHAPTER V: CONCLUSION

The role convection plays in the heat budget of the UTLS has become a major research topic over the past few decades because of the importance of convection in influencing climate processes by regulating stratospheric water vapor through direct injection, by enhancing thin cirrus cloud presence, and by modulating the ozone budget. However, the impact of convection on the UTLS temperature structure has seen varying results between previous studies due to considerable limitations in both convection and temperature observations. The launch of the TRMM satellites has allowed an unprecedented mapping of deep convective characteristics across the tropics and subtropics, and the more-recent launch of GPM has expanded these capabilities into the extratropics. Additionally, GPS RO temperature soundings have begun to fill gaps in temperature data by offering global observations of UTLS temperatures with a high vertical resolution in all-weather conditions. Through the combined use of these datasets, this study has provided new insight into upper tropospheric and lower stratospheric temperature structure variations over both tropical and extratropical precipitation systems.

In the tropics, deep convection was analyzed in two different regions and produced a layer of warm anomalies in the upper troposphere (0.2 to 0.8 K) due to convective latent heat release. The anomalies transitioned to a layer of cooling near the tropopause (-0.4 to -1.5 K) which occur because as gravity waves spread the warming due to convective heating through the free troposphere, hydrostatic pressure gradients will extend above the heating, causing divergence, ascent, and adiabatic cooling aloft. In the lower stratosphere, a mixture of warming occurred in the PWP and cooling in the TACO region. The amplitude of diurnal temperature variation increased by 0.2-0.3 K at both 11 km and 17 km altitude in both regions after deep convection occurs, which confirmed the important role deep convection plays in enhancing the

UTLS diurnal temperature variation in the tropics. Land-ocean contrast played a significant role in determining anomaly magnitude. For example, over land, a layer of cool anomalies was observed within 14-22 km that range from -0.3 to -1.5 K, whereas over the oceans, the layer of cool anomalies generally is only within 14-17 km and a layer of warm anomalies developed above the tropopause within 17-20 km, ranging from 0.2 to 0.5 K. Finally, there is a clear impact of convection depth on the vertical temperature anomaly structure, as a robust pattern of increasing temperature anomalies was observed as convective depth increases. Additionally, it was shown that a combination of the minimum IR CTT and 20 dBZ echo top height is needed to obtain the full picture of convective effects to the UTLS temperature environment. However, deep convection with higher 40 dBZ heights do not lead to a larger magnitude of cool anomalies near the tropopause. This implies that presumably stronger deep convection with higher 40 dBZ heights do not necessarily reach overall higher altitudes or result in a more significant impact to UTLS temperatures compared to less intense convection.

In the extratropics, PFs were compared to two different synoptic background profiles using potential vorticity on the 320 K isentropic surface and then classified into non-DSI and DSI categories to quantify UTLS temperature and tropopause height anomalies under these two different types of environments. Extratropical non-DSI PFs displayed a similar UTLS temperature structure to tropical deep convection, as warm anomalies ranging from 0.1 to 1 K were observed in the upper troposphere, which transitioned to a layer of cool anomalies centered around the LRT ranging from -2 to -3 K, and then back to warm anomalies ranging from 0.2 to 1 K in the lower stratosphere. On the other hand, DSI PFs displayed much different results, as strong cooling ranging from -2 K to -5 K was observed throughout the mid/upper troposphere, with maximum values occurring slightly below the PF LRT. The anomalies transitioned to

moderate/strong warming above the LRT, ranging from 2 K to 4 K. This temperature anomaly pattern occurs due to strong horizontal dynamic mixing among contrasting tropical and polar air masses and is associated with tropopause folding and a lowering of the tropopause. These DSI PFs likely contribute considerably to the large temperature standard deviation observed throughout the upper troposphere within the mid/high latitudes. The impact of PF depth and size to anomaly magnitude was analyzed. For non-DSI PFs, the largest anomaly magnitudes generally occurred for PFs with the weakest RD. In contrast, UTLS anomaly magnitudes consistently increased from the smallest to the largest PFs. These differences are related to the life cycle of a PF, as intense overshooting convection typically occurs in the earlier stages of convective development and enough time may not have passed to spread the warming and cooling to the environment surrounding the PF. DSI PFs showed the opposite results, as the largest UTLS anomaly magnitudes occurred near the most intense overshooting PFs, whereas the largest area PFs displayed the weakest magnitudes. We hypothesize that this is related to responses of temperature in the UTLS and properties of PFs under the different stages of extratropical cyclone development. The overall vertical structure of UTLS temperature anomalies is similar for land and oceanic PFs, but in general, anomaly variations and magnitudes are larger near oceanic PFs. Seasonal UTLS temperature anomalies were also explored in different latitude bands in both hemispheres. For non-DSI PFs, the strongest tropopause-level cooling was observed in different seasons from 20°-40° to 40°-65°, which is attributed to latitudinal seasonal variations of PF characteristics. For DSI PFs, the strongest upper tropospheric cooling and lower stratospheric warming occurred in the wintertime due to stronger temperature contrasts fueling the development of intense midlatitude cyclones, which cause deeper tropopause folding and likely more stratosphere-troposphere exchange. Finally, PF

impact to tropopause height was also quantified relative to both area and RD. For non-DSI PFs, minor decreases in LRT height (-0.1 to -0.4 km) were generally observed for PFs with a large RD and small-to-moderate size, whereas PFs with a small RD and large area displayed large height increases (0.2 to 1 km). This resulted in two commonly observed types of UTLS temperature profiles, as the PFs either push the tropopause higher and it becomes colder, or a double tropopause structure develops with a new, lower tropopause forming near the top of the convective cloud beneath the higher climatological LRT. DSI PFs were associated with much larger tropopause anomalies as height decreases ranged from 0.25 km to 2 km during significant deep stratospheric intrusion events, indicative of general subsidence and tropopause folding. One common type of profile was observed, as the LRT displayed a much stronger than normal temperature transition and a robust tropopause inversion layer was seen.

Finally, climatological characteristics of the extratropical tropopause were examined in order to determine where and when does tropopause bimodality occurs, what the tropopause characteristics were in these bimodal regions, and how the occurrence of double tropopauses relates to bimodality. First, four locations were chosen from Seidel & Randel (2007) to determine when bimodality occurred. A distinct seasonality in tropopause heights was observed in each region, which contrasts with their statement that bimodality occurs year-round in these locations. Overall, tropopause bimodality occurred in the Northern Hemisphere winter in a $\sim 10^\circ$ - 20° wide band between 20° - 40° latitude with considerable zonal variation due to the location of the subtropical jet. This band shrinks throughout spring and into summer as the jet weakens. However, bimodality persisted in the summer over northern Asia due to strengthening of the Asian monsoon circulation. Bimodality in the Southern Hemisphere generally displayed a width of $\sim 10^\circ$ in all seasons and demonstrated much less meridional movement. The height threshold

separating the two modes was much higher on the tropical side of the band (>13.5 km) and decreased quickly towards the polar side of the band (<12.5 km), except in the Northern Hemisphere summer. Additionally, the total relative frequency of occurrence for profiles with tropopause heights within the lower mode showed a distinct shift in frequencies within all seasons, as the tropical side of the band typically has fewer profiles with tropopause heights within the lower mode ($<40\%$ occurrence) whereas the extratropical side has many more occurring within the lower mode ($>60\%$). This occurred relatively quickly (within 2.5° - 5° latitude) due to the characteristic “tropopause break” that occurs at these latitudes. The relationship between double tropopauses and bimodality was also investigated. The location of the bimodal region is generally close to the locations that experience a high frequency of DTs. Frequencies were highest in the winter as, for example, NH DJF observed a large area of frequencies $>50\%$ along the poleward edge of the bimodal region and these values decreased steadily through the seasons. There was a distinct meridional shift in the percentage of double tropopause profiles that have their LRT1 within that grid’s lower mode, as DT profiles from the poleward side of the bimodal band have a lower (extratropical) tropopause height (values of $>80\%$ with some up to 95%) whereas in contrast, many grids on the tropical side of the bimodal band observe percentages of $<50\%$. This indicates that not all double tropopause environments are the same. When analyzing bimodal locations for profiles that have been identified as only having a single tropopause, the bimodal band became much smaller in extent (2.5° - 7.5°), showed many additional gaps, and its location was shifted toward the poleward edge of the previously identified bimodal region throughout all seasons and in both hemispheres. The results shown here suggest that two main factors contribute to the occurrence of seasonal tropopause bimodality. On the tropical side of the bimodal band, bimodality is mainly due to the occurrences

of double tropopauses, whereas on the polar side, bimodality is mainly due to single tropopause profiles that are more tropical in nature.

The results shown in this dissertation display the unique characteristics of the UTLS and the noteworthy impact that both tropical and extratropical precipitation systems have on its thermodynamic structure. Additionally, these results suggest there are intricate relationships between different types of precipitation systems and their properties to the types of temperature anomalies that they produce. It is likely that this study will enhance the community's understanding of both tropical and extratropical convection, stratosphere-troposphere exchange processes, and lead to the continued improvement of PF representation in both weather and climate models. Future research topics will attempt to address some of the key limitations of this study. For example, TRMM/GPM only provide snapshots of the convection at the time of observation. Thus, the stage of development of the convection is unknown (although can be inferred to some extent). This has left gaps in our ability to fully explain some of the types of anomalies observed in this study. The newly developed Integrated Multi-satellitE Retrievals for GPM (IMERG) dataset has shown very promising ability to track and identify storm stage of development. The precipitation information obtained from IMERG can be collocated with thermodynamic profiles from the recently launched COSMIC-2 constellation throughout the tropics and subtropics, as many more collocations will now be possible due to the increase in tropical sampling associated with COSMIC-2. Then, the time that the temperature profile occurred relative to the stage of the storm can be recorded, which will allow for the ability to determine differences in temperature anomaly magnitude for the early/mature/dissipation stages throughout both the convective latent heating region of the mid/upper troposphere and adiabatic cooling region near the tropopause.

REFERENCES

- Alexander, P., A. de la Torre, P. Llamedo, and R. Hierro (2014), Precision estimation in temperature and refractivity profiles retrieved by GPS radio occultations, *J. Geophys. Res. Atmos.*, *10*, 8624–8638, doi:10.1002/2013JD021016.
- Anel, J. A., Antuna, J. C., Torre, L. D. La, Castanheira, M., & Gimeno, L. (2008). Climatological features of global multiple tropopause events. *Journal of Geophysical Research*, *113*, 1–14. <http://doi.org/10.1029/2007JD009697>
- Anthes, R. A., Ector, D., Hunt, D. C., Kuo, Y.-H., Rocken, C., Schreiner, W. S., ... Yen, N. L. (2008). The COSMIC/FORMOSAT-3 Mission: Early Results. *Bulletin of the American Meteorological Society*, *89*(3), 313–333. <http://doi.org/10.1175/BAMS-89-3-313>
- Appenzeller, C., Davies, H. C., & Norton, W. A. (1996). Fragmentation of stratospheric intrusions. *Journal of Geophysical Research: Atmospheres*, *101*(D1), 1435–1456. <http://doi.org/10.1029/95JD02674>
- Bangare, S. L., Dubal, A., Bangare, P. S., & Patil, S. T. (2015). Reviewing Otsu's Method For Image Thresholding. *International Journal of Applied Engineering Research*, *10*(9), 21777–21783.
- Baray, J.-L., Daniel, V., Ancellet, G., & Legras, B. (2000). Planetary-scale tropopause folds in the southern subtropics. *Geophysical Research Letters*, *27*(3), 353–356.
- Beyerle, G., Grunwaldt, L., Heise, S., Köhler, W., König, R., Michalak, G., ... Giesinger, B. (2011). First results from the GPS atmosphere sounding experiment TOR aboard the TerraSAR-X satellite. *Atmospheric Chemistry and Physics*, *11*(13), 6687–6699. <http://doi.org/10.5194/acp-11-6687-2011>
- Beyerle, G., Schmidt, T., Michalak, G., Heise, S., Wickert, J., & Reigber, C. (2005). GPS radio

- occultation with GRACE: Atmospheric profiling utilizing the zero difference technique. *Geophysical Research Letters*, 32(13), 1–5. <http://doi.org/10.1029/2005GL023109>
- Biondi, R., Randel, W. J., Ho, S.-P., Neubert, T., & Syndergaard, S. (2012). Thermal structure of intense convective clouds derived from GPS radio occultations. *Atmospheric Chemistry and Physics*, 12, 5309–5318. <http://doi.org/10.5194/acp-12-5309-2012>
- Birner, T. (2006). Fine-scale structure of the extratropical tropopause region. *Journal of Geophysical Research*, 111(February), 1–14. <http://doi.org/10.1029/2005JD006301>
- Bosart, L. F., & Lin, S. C. (1984). A Diagnostic Analysis of the Presidents' Day Storm of February 1979. *Monthly Weather Review*, 112, 2148–2177.
- Castanheira, J. M., & Gimeno, L. (2011). Association of double tropopause events with baroclinic waves. *Journal of Geophysical Research*, 116, 1–9. <http://doi.org/10.1029/2011JD016163>
- Chae, J. H., Wu, D. L., Read, W. G., & Sherwood, S. C. (2011). The role of tropical deep convective clouds on temperature, water vapor, and dehydration in the tropical tropopause layer (TTL). *Atmospheric Chemistry and Physics*, 11, 3811–3821. <http://doi.org/10.5194/acp-11-3811-2011>
- Chen, P. (1995). Isentropic cross-tropopause mass exchange in the extratropics. *Journal of Geophysical Research*, 100(D8), 16661. <http://doi.org/10.1029/95JD01264>
- Costantino, L., P. Heinrich, N. Mzé, and A. Hauchecorne (2015), Convective gravity wave propagation and breaking in the stratosphere: Comparison between WRF model simulations and lidar data, *Ann. Geophys.*, 33(9), 1155–1171, doi:10.5194/angeo-33-1155-2015.
- Danielsen, E. F. (1968). Stratospheric-Tropospheric Exchange Based on Radioactivity, Ozone and Potential Vorticity. *Journal of the Atmospheric Sciences*, 25, 502–518.

- Danzer, J., U. Foelsche, B. Scherllin-Pirscher, and M. Schwärz (2014), Influence of changes in humidity on dry temperature in GPS RO climatologies, *Atmos. Meas. Tech.*, 7(9), 2883–2896, doi:10.5194/amt-7-2883-2014.
- Dee, D. P., Uppala, S. M., Simmons, A. J., Berrisford, P., Poli, P., Kobayashi, S., ... Geer, A. J. (2011). The ERA-Interim reanalysis : configuration and performance of the data assimilation system. *Quarterly Journal of the Royal Meteorological Society*, (April), 553–597. <http://doi.org/10.1002/qj.828>
- Feng, S., Fu, Y., & Xiao, Q. (2011). Is the tropopause higher over the Tibetan Plateau? Observational evidence from Constellation Observing System for Meteorology, Ionosphere, and Climate (COSMIC) data. *Journal of Geophysical Research*, 116, 1–12. <http://doi.org/10.1029/2011JD016140>
- Foelsche, U., Borsche, M., Steiner, A. K., Gobiet, A., Pirscher, B., Kirchengast, G., ... Schmidt, T. (2008). Observing upper troposphere-lower stratosphere climate with radio occultation data from the CHAMP satellite. *Climate Dynamics*, 31(1), 49–65. <http://doi.org/10.1007/s00382-007-0337-7>
- Fritts, D. C. D. C. D. C., and M. J. Alexander (2003), Gravity Wave Dynamics and Effects in the Middle Atmosphere, *Rev. Geophys.*, 41(1), 1–64, doi:10.1029/2001RG000106.
- Fueglistaler, S., Dessler, A. E., Dunkerton, T. J., Folkins, I., Fu, Q., & Ote, P. W. (2009). Tropical tropopause layer, *Rev. Reviews of Geophysics*, (2009), 1–31. <http://doi.org/10.1029/2008RG000267>.1.INTRODUCTION
- Gettelman, A., & Birner, T. (2007). Insights into Tropical Tropopause Layer processes using global models. *Journal of Geophysical Research*, 112(December), 1–15. <http://doi.org/10.1029/2007JD008945>

- Gettelman, A., Pan, L. L., Randel, W. J., Hoor, P., Birner, T., & Hegglin, M. I. (2011). The Extratropical Upper Troposphere and Lower Stratosphere. *Reviews of Geophysics*, 49(3), 1–31. <http://doi.org/10.1029/2011RG000355>.1.INTRODUCTION
- Gray, S. L. (2003). A case study of stratosphere to troposphere transport: The role of convective transport and the sensitivity to model resolution. *Journal of Geophysical Research*, 108(D18), 4590. <http://doi.org/10.1029/2002JD003317>
- Grosvenor, D. P., Choulaton, T. W., Coe, H., & Held, G. (2007). A study of the effect of overshooting deep convection on the water content of the TTL and lower stratosphere from Cloud Resolving Model simulations. *Atmospheric Chemistry and Physics*, 7, 4977–5002. <http://doi.org/10.5194/acpd-7-7277-2007>
- Hamada, A., & Takayabu, Y. N. (2016). Improvements in Detection of Light Precipitation with the Global Precipitation Measurement Dual-Frequency Precipitation Radar (GPM DPR). *Journal of Atmospheric and Oceanic Technology*, 33(2012), 653–667. <http://doi.org/10.1175/JTECH-D-15-0097.1>
- Hassim, M. E. E., & Lane, T. P. (2010). A model study on the influence of overshooting convection on TTL water vapour. *Atmospheric Chemistry and Physics*, 10(20), 9833–9849. <http://doi.org/10.5194/acp-10-9833-2010>
- Haynes, P., Scinocca, J., & Greenslade, M. (2001). Formation and maintenance of the extratropical tropopause by baroclinic eddies. *Geophysical Research Letters*, 28(22), 4179–4182.
- Held, I. M. (1982). On the Height of the Tropopause and the Static Stability of the Troposphere. *Journal of the Atmospheric Sciences*, 39, 412–417.
- Hindley, N. P., Wright, C. J., Smith, N. D., & Mitchell, N. J. (2015). The southern stratospheric

gravity wave hot spot: Individual waves and their momentum fluxes measured by COSMIC GPS-RO. *Atmospheric Chemistry and Physics*, 15(14), 7797–7818.

<http://doi.org/10.5194/acp-15-7797-2015>

Holloway, C., & Neelin, J. D. (2007). The Convective Cold Top and Quasi Equilibrium *.

Journal of the Atmospheric Sciences, 64, 1467–1488. <http://doi.org/10.1175/JAS3907.1>

Holton, J. R., Haynes, P. H., McIntyre, M. E., Douglass, A. R., Rood, R. B., & Pfister, L. (1995).

Stratosphere-Troposphere Exchange. *Reviews of Geophysics*, (95), 403–439.

Homeyer, C. R., Bowman, K. P., & Pan, L. L. (2010). Extratropical tropopause transition layer

characteristics from high \square resolution sounding data. *Journal of Geophysical Research*,

115, 1–12. <http://doi.org/10.1029/2009JD013664>

Homeyer, C. R., Pan, L. L., Dorsi, S. W., Avallone, L. M., Weinheimer, A. J., O'Brien, A. S., ...

Campos, T. L. (2014). Convective transport of water vapor into the lower stratosphere

observed during double tropopause events. *Journal of Geophysical Research: Atmospheres*,

2014JD021485. <http://doi.org/10.1002/2014JD021485>

Hoskins, B. J., McIntyre, M. E., & Robertson, A. W. (1985). On the use and significance of

isentropic potential vorticity maps. *Quarterly Journal of the Royal Meteorological Society*,

111(6), 877–946. <http://doi.org/10.1002/qj.49711147002>

Hou, A. Y., Kakar, R. K., Neeck, S., Azarbarzin, A. A., Kummerow, C. D., Kojima, M., ...

Iguchi, T. (2014). The Global Precipitation Measurement Mission. *Bulletin of the American*

Meteorological Society, 95(5), 701–722. <http://doi.org/10.1175/BAMS-D-13-00164.1>

Houze, R. A. (1989). Observed structure of mesoscale convective systems and implications for

large-scale heating. *Quarterly Journal of the Royal Meteorological Society*, 115(487), 425–

461.

- Johnston, B. R., Xie, F., & Liu, C. (2018). The Effects of Deep Convection on Regional Temperature Structure in the Tropical Upper Troposphere and Lower Stratosphere. *Journal of Geophysical Research: Atmospheres*, *123*(3), 1585–1603.
<http://doi.org/10.1002/2017JD027120>
- Khaykin, S. M., Pommereau, J.-P., & Hauchecorne, a. (2013). Impact of land convection on temperature diurnal variation in the tropical lower stratosphere inferred from COSMIC GPS radio occultations. *Atmospheric Chemistry and Physics*, *13*(13), 6391–6402.
<http://doi.org/10.5194/acp-13-6391-2013>
- Kim, H., & Dessler, A. E. (2004). Observations of convective cooling in the tropical tropopause layer in AIRS data. *Atmospheric Chemistry and Physics Discussions*, *4*(6), 7615–7629.
<http://doi.org/10.5194/acpd-4-7615-2004>
- Kim, J., Randel, W. J., & Birner, T. (2018). Convectively Driven Tropopause-Level Cooling and Its Influences on Stratospheric Moisture. *Journal of Geophysical Research: Atmospheres*, *123*(1), 590–606. <http://doi.org/10.1002/2017JD027080>
- Kummerow, C., Barnes, W., Kozu, T., Shiue, J., & Simpson, J. (1998). The Tropical Rainfall Measuring Mission (TRMM) Sensor Package. *Journal of Atmospheric and Oceanic Technology*, *15*, 809–818.
- Kunz, A., Konopka, P., Müller, R., & Pan, L. L. (2011). Dynamical tropopause based on isentropic potential vorticity gradients. *Journal of Geophysical Research Atmospheres*, *116*(1), 1–13. <http://doi.org/10.1029/2010JD014343>
- Kursinski, E. R., Hajj, G. A., Schofield, J. T., Linfield, R. P., & Hardy, K. R. (1997). Observing Earth's atmosphere with radio occultation measurements using the Global Positioning System. *Journal of Geophysical Research*, *102*(D19), 23.429--23.465.

<http://doi.org/10.1029/97JD01569>

- Labitzke, K., & Kunze, M. (2009). Variability in the stratosphere: The sun and the QBO. In *Climate and Weather of the Sun-Earth System (CAWSES)* (pp. 257–278).
- Lamarque, J.-F., Langford, a. O., & Proffitt, M. H. (1996). Cross-tropopause mixing of ozone through gravity wave breaking: Observation and modeling. *Journal of Geophysical Research: Atmospheres*, *101*(D17), 22969–22976. <http://doi.org/10.1029/96JD02442>
- Lee, S. U., Chung, S. Y., & Park, R. H. (1990). A Comparative Performance Study of Several Global Thresholding Techniques for Segmentation. *Computer Vision, Graphics, and Image Processing*, *52*, 171–190.
- Liu, C., and E. J. Zipser (2009), “Warm rain” in the tropics: Seasonal and regional distributions based on 9 yr of TRMM data, *J. Clim.*, *22*(3), 767–779, doi:10.1175/2008JCLI2641.1.
- Liu, C., E. J. Zipser, and S. W. Nesbitt (2007), Global distribution of tropical deep convection: Different perspectives from TRMM infrared and radar data, *J. Clim.*, *20*(3), 489–503, doi:10.1175/JCLI4023.1.
- Liu, C., & Zipser, E. J. (2015). The global distribution of largest, deepest, and most intense precipitation systems. *Geophysical Research Letters*, *42*(9), 3591–3595. <http://doi.org/10.1002/2015GL063776>
- Liu, C., Zipser, E. J., Cecil, D. J., Nesbitt, S. W., & Sherwood, S. (2008). A cloud and precipitation feature database from nine years of TRMM observations. *Journal of Applied Meteorology and Climatology*, *47*(10), 2712–2728. <http://doi.org/10.1175/2008JAMC1890.1>
- Liu, N., & Liu, C. (2016). Global distribution of deep convection reaching tropopause in 1 year GPM observations. *Journal of Geophysical Research: Atmospheres*, *121*, 3824–3842.

<http://doi.org/10.1002/2015JD023364>.Received

- Liu, Z., D. Ostrenga, W. Teng, and S. Kempler (2012), Tropical Rainfall Measuring Mission (TRMM) Research and Applications, *Bull. Am. Meteorol. Soc.*, (September), 1317–1326.
- Machado, L. A. T., Rossow, W. B., Guedes, R. L., & Walker, A. W. (1998). Life Cycle Variations of Mesoscale Convective Systems over the Americas. *Monthly Weather Review*, *126*, 1630–1654.
- McIntyre, M. E., & Norton, W. A. (2000). Potential Vorticity Inversion on a Hemisphere. *Journal of the Atmospheric Sciences*, *57*(9), 1214–1235. [http://doi.org/10.1175/1520-0469\(2000\)057<1214:PVIOAH>2.0.CO;2](http://doi.org/10.1175/1520-0469(2000)057<1214:PVIOAH>2.0.CO;2)
- McLandress, C. (1997), Seasonal variability of the diurnal tide: Results from the Canadian middle atmosphere general circulation model, *J. Geophys. Res. Atmos.*, *102*(D25), 29747–29764, doi:10.1029/97JD02645.
- Otsu, N. (1979). A Threshold Selection Method from Gray-Level Histograms. *IEEE Transactions on Systems, Man, and Cybernetics*, *SMC-9*(1), 62–66.
- Pan, L. L., Randel, W. J., Gary, B. L., Mahoney, M. J., & Hints, E. J. (2004). Definitions and sharpness of the extratropical tropopause: A trace gas perspective. *Journal of Geophysical Research D: Atmospheres*, *109*(23), 1–11. <http://doi.org/10.1029/2004JD004982>
- Pan, L. L., Randel, W. J., Gille, J. C., Hall, W. D., Nardi, B., Massie, S., ... Tarasick, D. (2009). Tropospheric intrusions associated with the secondary tropopause. *Journal of Geophysical Research*, *114*, 1–12. <http://doi.org/10.1029/2008JD011374>
- Paulik, L. C., & Birner, T. (2012). Quantifying the deep convective temperature signal within the tropical tropopause layer (TTL). *Atmospheric Chemistry and Physics*, *12*, 12183–12195. <http://doi.org/10.5194/acp-12-12183-2012>

- Peevey, T. R., Gille, J. C., Homeyer, C. R., & Manney, G. L. (2014). The double tropopause and its dynamical relationship to the tropopause inversion layer in storm track regions. *Journal of Geophysical Research*, *119*(17), 10,194-10,212. <http://doi.org/10.1002/2014JD021808>
- Peevey, T. R., Gille, J. C., Randall, C. E., & Kunz, A. (2012). Investigation of double tropopause spatial and temporal global variability utilizing High Resolution Dynamics Limb Sounder temperature observations. *Journal of Geophysical Research*, *117*, 1–14. <http://doi.org/10.1029/2011JD016443>
- Pirscher, B., U. Foelsche, M. Borsche, G. Kirchengast, and Y. H. Kuo (2010), Analysis of migrating diurnal tides detected in FORMOSAT-3 / COSMIC temperature data, *J. Geophys. Res.*, *115*, 1–16, doi:10.1029/2009JD013008.
- Poli, P., Healy, S. B., & Dee, D. P. (2010). Assimilation of Global Positioning System radio occultation data in the ECMWF ERA-Interim reanalysis. *Quarterly Journal of the Royal Meteorological Society*, *136*(653), 1972–1990. <http://doi.org/10.1002/qj.722>
- Potter, B. E., and J. R. Holton (1995), The Role of Monsoon Convection in the Dehydration of the Lower Tropical Stratosphere, *J. Atmos. Sci.*, *52*(8), 1034–1050.
- Poulida, O., Dickerson, R. R., & Heymsfield, A. (1996). Stratosphere-troposphere exchange in a midlatitude mesoscale convective complex 1.Observations. *Journal of Geophysical Research*, *101*(95), 6823–6836.
- Price, J. D., & Vaughan, G. (1993). The potential for stratosphere-troposphere exchange in cut-off low systems. *Quarterly Journal of the Royal Meteorological Society*, *119*, 343–365.
- Randel, W. J., Seidel, D. J., & Pan, L. L. (2007). Observational characteristics of double tropopauses. *Journal of Geophysical Research*, *112*, 1–13. <http://doi.org/10.1029/2006JD007904>

- Randel, W. J., Wu, F., & Rios, W. (2003). Thermal variability of the tropical tropopause region derived from GPS / MET observations. *Journal of Geophysical Research*, *108*, 1–12.
<http://doi.org/10.1029/2002JD002595>
- Randel, W. J., & Wu, F. (2010). The Polar Summer Tropopause Inversion Layer. *Journal of the Atmospheric Sciences*, *67*, 2572–2581. <http://doi.org/10.1175/2010JAS3430.1>
- Reed, R. J. (1955). A Study of a Characteristic Type of Upper-Level Frontogenesis. *Journal of Meteorology*, *12*, 226–237.
- Reid, H. J., & Vaughan, G. (2004). Convective mixing in a tropopause fold. *Quarterly Journal of the Royal Meteorological Society*, *130*(599 PART B), 1195–1212.
<http://doi.org/10.1256/qj.03.21>
- Rieckh, T., Scherllin-Pirscher, B., Ladstädter, F., & Foelsche, U. (2014). Characteristics of tropopause parameters as observed with GPS radio occultation. *Atmospheric Measurement Techniques*, *7*(11), 3947–3958. <http://doi.org/10.5194/amt-7-3947-2014>
- Santer, B. D., Sausen, R., Wigley, T. M. L., Boyle, J. S., Achutarao, K., Doutriaux, C., ... Taylor, K. E. (2003). Behavior of tropopause height and atmospheric temperature in models, reanalyses, and observations: Decadal changes. *Journal of Geophysical Research*, *108*, 1–22. <http://doi.org/10.1029/2002JD002258>
- Santhi, Y. D., Ratnam, M. V., Dhaka, S. K., & Rao, S. V. (2014). Global morphology of convection indices observed using COSMIC GPS RO satellite measurements. *Atmospheric Research*, *137*, 205–215. <http://doi.org/10.1016/j.atmosres.2013.10.002>
- Scherllin-Pirscher, B., G. Kirchengast, A. K. Steiner, Y. Kuo, and U. Foelsche (2011), Quantifying uncertainty in climatological fields from GPS radio occultation : an empirical-analytical error model, *Atmos. Meas. Tech. Discuss.*, *4*, 2749–2788, doi:10.5194/amtd-4-

2749-2011.

- Schmidt, T., Beyerle, G., Heise, S., Wickert, J., & Rothacher, M. (2006). A climatology of multiple tropopauses derived from GPS radio occultations with CHAMP and SAC-C. *Geophysical Research Letters*, *33*, 1–4. <http://doi.org/10.1029/2005GL024600>
- Schreiner, W., C. Rocken, S. Sokolovskiy, S. Syndergaard, and D. Hunt (2007), Estimates of the precision of GPS radio occultations from the COSMIC / FORMOSAT-3 mission, *Geophys. Res. Lett.*, *34*, 1–5, doi:10.1029/2006GL027557.
- Schumacher, C., Houze, R. A., & Kraucunas, I. (2004). The Tropical Dynamical Response to Latent Heating Estimates Derived from the TRMM Precipitation Radar. *Journal of the Atmospheric Sciences*, *61*, 1341–1358.
- Seidel, D. J., & Randel, W. J. (2006). Variability and trends in the global tropopause estimated from radiosonde data. *Journal of Geophysical Research*, *111*, 1–17. <http://doi.org/10.1029/2006JD007363>
- Seidel, D. J., & Randel, W. J. (2007). Recent widening of the tropical belt: Evidence from tropopause observations. *Journal of Geophysical Research*, *112*, D20113. <http://doi.org/10.1029/2007JD008861>
- Senthilkumaran, N., & Vaithegi, S. (2016). Image Segmentation by Using Thresholding Techniques for Medical Images. *Computer Science and Engineering: An International Journal*, *6*(1), 1–13. <http://doi.org/10.5121/cseij.2016.6101>
- Seto, S., Iguchi, T., & Oki, T. (2013). The Basic Performance of a Precipitation Retrieval Algorithm for the Global Precipitation Measurement Mission's Single/Dual-Frequency Radar Measurements. *IEEE Transactions on Geoscience and Remote Sensing*, *51*(12), 1–13.
- Shapiro, M. A. (1980). Turbulent Mixing within Tropopause Folds as a Mechanism for the

- Exchange of Chemical Constituents between the Stratosphere and Troposphere. *Journal of the Atmospheric Sciences*, 37, 994–1004.
- Sherwood, S., Horinouchi, T., & Zeleznik, H. (2003). Convective Impact on Temperatures Observed near the Tropical Tropopause. *Journal of the Atmospheric Sciences*, 60, 1847–1857.
- Škerlak, B., Sprenger, M., Pfahl, S., Tyrlis, E., & Wernli, H. (2015). Tropopause folds in ERA-interim: Global climatology and relation to extreme weather events. *Journal of Geophysical Research: Atmospheres*, 120(10), 4860–4877. <http://doi.org/10.1002/2014JD022787>
- Smith, E. K., & Weintraub, S. (1953). The Constants in the Equation for Atmospheric Refractive Index at Radio Frequencies. *Proceedings of the IRE*, 41(8), 1035–1037. <http://doi.org/10.1109/JRPROC.1953.274297>
- Son, S. W., Tandon, N. F., & Polvani, L. M. (2011). The fine-scale structure of the global tropopause derived from COSMIC GPS radio occultation measurements. *Journal of Geophysical Research*, 116, 1–17. <http://doi.org/10.1029/2011JD016030>
- Sprenger, M., Wernli, H., & Bourqui, M. (2007). Identification and ERA-15 Climatology of Potential Vorticity Streamers and Cutoffs near the Extratropical Tropopause. *Journal of the Atmospheric Sciences*, 64(5), 1569–1586. <http://doi.org/10.1175/JAS3912.1>
- Thompson, D. W. J., Bony, S., & Li, Y. (2017). Thermodynamic constraint on the depth of the global tropospheric circulation. *PNAS*, 114(31), 8181–8186. <http://doi.org/10.1073/pnas.1620493114>
- Uccellini, L. W. (1986). The Possible Influence of Upstream Upper-Level Baroclinic Processes on the Development of the QE II Storm. *Monthly Weather Review*, 114, 1019–1027.
- Vaughan, G., Price, J. D., & Howells, A. (1994). Transport into the troposphere in a tropopause

- fold. *Quarterly Journal of the Royal Meteorological Society*, 120(518), 1085–1103.
<http://doi.org/10.1002/qj.49712051814>
- Vorob'ev, V. V., & Krasnil'nikova, T. G. (1994). Estimation of the Accuracy of the Atmospheric Refractive Index Recovery from Doppler Shift Measurements at Frequencies Used in the NAVSTAR System. *Physics of the Atmosphere and Ocean*, 29(5), 602–609.
- Wernli, H., & Sprenger, M. (2007). Identification and ERA-15 Climatology of Potential Vorticity Streamers and Cutoffs near the Extratropical Tropopause. *Journal of the Atmospheric Sciences*, 64(5), 1569–1586. <http://doi.org/10.1175/JAS3912.1>
- World Meteorological Organization (1986). Atmospheric ozone 1985. *WMO 16, Geneva*.
- Xian, T., & Fu, Y. (2015). Characteristics of tropopause-penetrating convection determined by TRMM and COSMIC GPS radio occultation measurements. *Journal of Geophysical Research Atmospheres*, 120(14), 7006–7024. <http://doi.org/10.1002/2014JD022633>
- Xie, F., D. L. Wu, C. O. Ao, and a. J. Mannucci (2010), Atmospheric diurnal variations observed with GPS radio occultation soundings, *Atmos. Chem. Phys.*, 10(14), 6889–6899, doi:10.5194/acp-10-6889-2010.
- Zeng, Z., W. Randel, S. Sokolovskiy, C. Deser, Y. H. Kuo, M. Hagan, J. Du, and W. Ward (2008), Detection of migrating diurnal tide in the tropical upper troposphere and lower stratosphere using the Challenging Minisatellite Payload radio occultation data, *J. Geophys. Res. Atmos.*, 113(3), 1–12, doi:10.1029/2007JD008725.
- Zhang, X., Gao, P., & Xu, X. (2014). Variations of the Tropopause Over Different Latitude Bands Observed Using COSMIC Radio Occultation Bending Angles. *IEEE Transactions on Geoscience and Remote Sensing*, 52(5), 2339–2349.